

Aus dem Institut für Transfusionsmedizin und Immunologie  
der Medizinischen Fakultät Mannheim  
(Direktor: Prof. Dr. med. Harald Klüter)

# Flow Morphometry of Red Blood Cell Storage Quality Based on Neural Networks

Inauguraldissertation  
zur Erlangung des akademischen Grades Doctor scientiarum humanarum  
(Dr.sc.hum.)  
der  
Medizinischen Fakultät Mannheim  
der Ruprecht-Karls-Universität  
zu  
Heidelberg

vorgelegt von  
Clemens Böcker

aus  
Minden  
2022

Dean: Prof. Dr. med. Sergij Goerd  
Advisor: Prof. Dr. rer. Nat. Karen Bieback

für Caro

# TABLE OF CONTENTS

ABREVIATIONS .....	1
1 INTRODUCTION .....	5
1.1 Red Blood Cells .....	5
1.2 Red Blood Cell Storage and Storage Lesion .....	7
1.3 RBC Morphology.....	10
1.4 Morphological Analysis of RBCs.....	14
1.4.1 Microfluidic Analysis Systems.....	14
1.4.2 Flow Morphometry System .....	15
1.5 Application of Neural Networks .....	17
1.6 Flow Morphometry applied to Air Rescue RCCs.....	20
1.7 Aim of the Study.....	22
2 MATERIALS AND METHODS.....	24
2.1 Materials .....	24
2.1.1 Devices, Components and Reagents .....	24
2.2 Flow Morphometry Setup .....	25
2.2.1 Fluidic System and Fluid Dynamics .....	25
2.2.2 Microscopic System.....	28
2.2.3 Software Platforms .....	29
2.2.4 Image Processing .....	29
2.2.5 Convolutional Neural Network (CNN) .....	32
2.2.6 Organization of the Data and CNN Training .....	34
2.2.7 Alternative CNN Architecture.....	37
2.3 RBC Sample Preparation and Morphology Classes .....	38
2.4 Statistics .....	40
2.5 Flow Morphometry applied to Air Rescue RCCs.....	41
2.5.1 Storage and Transport Logistics .....	41
2.5.2 Rotation System and Sampling.....	43
2.5.3 Biochemical and Morphological Quality Control.....	45
2.5.4 Statistics for Air Rescue RCCs .....	46
3 RESULTS.....	47
3.1 Improvements of the Flow Morphometry Setup .....	47
3.2 Convolutional Neural Network Based Image Processing.....	49
3.2.1 CNN Architecture and Development of RBC Morphology Class Composition .....	49

3.2.2	CNN Training Progress of GoogLeNet .....	53
3.2.3	High Resolution CNN Classification of Erythrocytes .....	56
3.2.4	CNN Classes Match Reference Data from Decision Tree-Based Classification .....	58
3.3	New Insights in Flow Morphometry of RBCs through High Resolution CNN Classification .....	61
3.3.1	Shear Induced Stomatocyte Morphology in Flow Channels .....	61
3.3.2	RBC Morphology Progression during Storage Lesion and its Application for Storage Lesion Monitoring .....	62
3.3.3	Illustration of Lesion Index as Indicator of Storage Lesion in Individual RCCs	64
3.3.4	The Lesion Index as Indicator for the Hemolysis Level .....	68
3.4	Non-inferior RCC Quality after Repeated Air Rescue Mission Transport for Prehospital Transfusion .....	71
3.4.1	A Rotation System Allows Regulatory-compliant Storage and Transport Logistics of RCCs for Repeated Air Rescue Missions .....	71
3.4.2	Biochemical Parameters of RBC Quality Show Non-Inferiority of RCCs after Repeated Air Rescue Missions .....	73
3.4.3	Flow Morphometric Analysis Confirms Non-Inferiority of RCCs after Repeated Air Rescue Missions .....	75
3.4.4	RBC Quality Parameters were not Affected by Flight Time Duration .....	79
4	DISCUSSION .....	82
4.1	Improved Classification Resolution of RBC Morphologies by CNNs .....	82
4.2	Shear Induced Morphologies by Morphometric Measurements in Flow Chambers .....	85
4.3	Prediction of Hemolysis Level Based on the Lesion Index .....	87
4.4	The Lesion Index as an Additional Storage Lesion Marker .....	89
4.5	The Standardization of Flow Morphometry for the Measurement of Storage Lesion .....	90
4.6	Non-Inferiority of RCC Quality after Repeated Air Rescue Missions under Specific Regulations of a Rotation System .....	91
4.7	Outlook .....	94
5	SUMMARY .....	96
6	REFERENCES .....	99
7	SUPPLEMENTARY INFORMATION .....	111
8	CURRICULUM VITAE .....	113
9	ACKNOWLEDGMENTS .....	115

Partial results of the presented work have been published in:

Boecker, C., Sitzmann, N., Halblaub Miranda, J. L., Suhr, H., Wiedemann, P., Bieback, K., Rudolph, M., & Klüter, H. (2022). Noninferior Red Cell Concentrate Quality after Repeated Air Rescue Mission Transport for Prehospital Transfusion. *Transfusion Medicine and Hemotherapy*, 49(3), 172-179. <https://doi.org/10.1159/000520650>

## ABREVIATIONS

<b>°C</b>	Degree Celsius
<b><i>f</i></b>	Activation Function
<b>2,3-DPG</b>	2,3-diphosphoglycerate
<b>A</b>	Ampere
<b>ATP</b>	Adenosine Triphosphate
<b>B</b>	Width
<b>BÄK</b>	Bundesärztekammer
<b>CCD</b>	Charged-Coupled Device
<b>CI95%</b>	95% Confidence Interval
<b>cm</b>	Centimeter
<b>CM</b>	Confusion Matrix
<b>CNN</b>	Convolutional Neural Network
<b>CO<sub>2</sub></b>	Carbon Dioxide
<b>CPD</b>	Citrate Phosphate Dextrose
<b>D</b>	Discocyte
<b>D<sub>h</sub></b>	Dynamic Diameter
<b>DS</b>	Deformed Stomatocyte
<b>DT</b>	Decision Tree
<b>E</b>	Echinocyte
<b>E1</b>	Echinocyte1
<b>E2</b>	Echinocyte2
<b>E3</b>	Echinocyte3
<b>F</b>	Flow Rate
<b>FDA</b>	Food and Drug Administration
<b>fHb</b>	Free Hemoglobin
<b>fL</b>	Femtoliter
<b>FN</b>	False Negative
<b>FP</b>	False Positive

<b>g</b>	Gram
<b>h</b>	Position of Focal Plane in Channel Height
<b>H</b>	Channel Height
<b>Hb</b>	Hemoglobin
<b>Hkt</b>	Hematocrit
<b>Hz</b>	Hertz
<b>I<sub>B</sub></b>	Binary Image
<b>I<sub>BG</sub></b>	Background Image
<b>I<sub>COM</sub></b>	Brightness-Compensated Image
<b>I<sub>DIV</sub></b>	Division Image
<b>IFC</b>	Imaging Flow Cytometry
<b>I<sub>HP</sub></b>	High-Pass Filtered Image
<b>I<sub>IN</sub></b>	Input Image
<b>I<sub>LP</sub></b>	Low-Pass Filtered Image
<b>I<sub>M</sub></b>	Binary Image after Morphological Operations
<b>I<sub>SC</sub></b>	Scaled Image
<b>ISM</b>	In Situ Microscopy
<b>I<sub>TH</sub></b>	Binary Image after High Threshold
<b>I<sub>TL</sub></b>	Binary Image after Low Threshold
<b>kPa</b>	Kilopascal
<b>L</b>	Liter
<b>M</b>	Cell Micrograph
<b>m</b>	Meter
<b>MCV</b>	Mean Corpuscular Volume
<b>MI</b>	Morphological Index
<b>min</b>	Minute
<b>mL</b>	Milliliter
<b>mm</b>	Millimeter
<b>mmol</b>	Millimolar
<b>mOsm</b>	Milliosmole
<b>n</b>	Number of Samples

<b>NA</b>	Numerical aperture
<b>NaCl</b>	Sodium Chloride
<b>NAD(P)H</b>	Nicotinamide Adenine Dinucleotide (Phosphate) Reducing Equivalent
<b>nm</b>	Nanometer
<b>NN</b>	Neural Network
<b>O<sub>2</sub></b>	Oxygen
<b>p</b>	Probability
<b>Pa</b>	Pascal
<b>PAGGSM</b>	Phosphate Adenine Glucose Guanosine Saline Mannitol
<b>pO<sub>2</sub></b>	Partial Pressure of Oxygen
<b>R<sup>2</sup></b>	Correlation Coefficient
<b>RBC</b>	Red Blood Cell
<b>RCC</b>	Red Blood Cell Concentrate
<b>Re</b>	Reynolds Number
<b>ROS</b>	Reactive Oxygen Species
<b>rpm</b>	Revolutions per Minute
<b>rps</b>	Revolutions per Second
<b>s</b>	Second
<b>S</b>	Spherocyte of Decision Tree
<b>SAG-M</b>	Saline Adenine Glucose-Mannitol
<b>SDE</b>	Stomatocyte-Discocyte-Echinocyte Sequence
<b>SE</b>	Spheroechinocyte
<b>SP</b>	Spherocyte
<b>ST</b>	Stomatocyte
<b>T</b>	Trilobe
<b>TP</b>	True Positive
<b>TRALI</b>	Transfusion-Related Acute Lung Injury
$\bar{v}$	Mean Flow Velocity
<b>w<sub>i</sub></b>	Weight

<b>xor</b>	Exclusive OR
$\dot{\gamma}$	Shear Rate
$\eta$	Dynamic Viscosity
$\mu\text{L}$	Microliter
$\mu\text{m}$	Micrometer
$\mu\text{s}$	Microsecond
$\rho$	Medium Density
$\tau$	Shear Stress

# 1 INTRODUCTION

## 1.1 Red Blood Cells

The main function of blood is to provide oxygen ( $O_2$ ) and nutrients for living cells (tissues and organs) and to remove waste products such as carbon dioxide ( $CO_2$ ) and urea (Pittman, 2011). Circulating blood performs these functions by maintaining the chemical environment within the tissues at an appropriate composition to guarantee their functionality (Pittman, 2011). Human blood consists of two major components: on the one hand, plasma (~55%) and, on the other hand, the cells-types leukocytes, thrombocytes and erythrocytes (otherwise called red blood cells and abbreviated in what follows as RBCs, ~45%) (Pittman, 2011). Plasma contains mainly water (~92% by volume) but also important substances such as proteins (albumin, blood-clotting factors and antibodies), nutrients (amino acids, sugars and fatty acids) and small amounts of other components such as electrolytes and hormones (Dean, 2005). RBCs fulfil the task of the oxygen transfer within the body by carrying the protein hemoglobin (Hb). Hemoglobin is a tetrameric protein that consists of two chains ( $\alpha$ - and  $\beta$ - chains), each of which is able to bind an oxygen molecule (oxyhemoglobin) (Perutz et al., 1960). The oxygen uptake at high partial pressure of  $O_2$  ( $pO_2$ ) in the lungs and the oxygen release at low  $pO_2$  when it circulates in small blood vessels is quantitatively described by the oxyhemoglobin dissociation curves (Tinmouth & Chin-Yee, 2001).

These various functions of blood are essential for human survival. A reduction of RBCs through small blood losses and the general renewal of blood can be compensated by the human body through erythropoiesis, meaning the natural production of RBCs (Hoffbrand, 2002; Turgeon, 2011). Erythropoiesis is regulated by the hormone erythropoietin. In the case of reduced  $O_2$  levels, which is detected by the kidneys, erythropoietin is secreted in the blood stream. Erythropoietin stimulates the proliferation and differentiation of red cell precursors, resulting in the enhanced production of RBCs.

Hemorrhage (severe bleeding) after trauma is one of the most common causes of death (Kleber et al., 2013; Oyeniyi et al., 2017; Pfeifer et al., 2009). In this circumstance erythropoiesis cannot cope with such large blood losses and the body is too slow to restore adequate oxygenation of the tissue. Therefore, the transfusions of blood

components, and especially RBCs, in the event of hemorrhagic shock is an integral part of therapy in the hospital (AWMF, 2012; Holcomb et al., 2015). Prehospital transfusion provides an immediate intervention in emergency cases. Air ambulance based prehospital transfusion, which is well suited to this purpose, has recently been implemented in the civilian sector in a few European and non-European countries (Karl et al., 2016; Lockey et al., 2013; Thies et al., 2020). Blood transfusion not only ensures proper tissue oxygenation but is also required to maintain volume and rheological properties in the blood. Yet, RBC transfusions also constitute standard therapy in symptomatic anemia in order to increase blood hemoglobin concentration and the hematocrit.

Globally approximately 85 million red blood cell concentrates (RCCs) are transfused annually, with the demand on the increase (Carson et al., 2012). To provide RBCs for transfusion, RCCs are made from whole blood donations. The blood is then separated into the plasma fraction, the buffy coat fraction (which is used for pooled thrombocyte concentrates) and finally the RBC fraction. These are stored in a bag with a specific stabilizer solution in order to ensure a consistent quality over the entire RCC shelf-life. To remove residual leukocytes, the RCCs need to be filtered by adhesion filtration. The resulting product is a RCC which is ready for transfusion. This can be stored for up to 42 days.

Besides acute and significant blood cell loss, the decision to undertake RBC transfusion is often based on the hemoglobin concentration ( $< 8\text{g/dL}$ ) (Vuille-Lessard et al., 2010). However, various clinical guidelines (Napolitano et al., 2009; Practical guideline for blood component therapy, 1996; Rogers et al., 2009) recommend that the patient's clinical condition and symptoms should be considered alongside the hemoglobin concentration when transfusing, rather than using only a single parameter (that is, usually the hemoglobin concentration). In this way, treatment outcomes can be improved and the risk of unnecessary RBC transfusions with possible post transfusion complications can be avoided (Carson et al., 2016).

Even though RBC transfusions can be life-saving procedures, stored RCCs from different donors used for transfusion are not qualitatively equal products (Garcia-Roa et al., 2017). This is a matter of concern in the transfusion practice for several reasons. Despite improved preservation methods of RBCs, an increased risk of mortality in critically ill and trauma patients (Hebert et al., 1999; Marik & Corwin, 2008), as well as

other negative side effects (such as pneumonia and acute lung injury) (Silliman & McLaughlin, 2006; Vamvakas & Carven, 1999), have been reported after RBC transfusion. In this connection, an increasing number of studies has focused on the possibly harmful influence of the storage duration of RCCs (Aubron et al., 2013; Hess et al., 2009; Lelubre et al., 2009; Tinmouth et al., 2006; Zimrin & Hess, 2009). These studies have raised concerns that “older” RBCs, which have been accumulated during prolonged storage of RCCs (Roussel et al., 2017), may lead to harm when transfused in critically ill patients. Therefore, it is better to avoid these functional changes of aged RBCs in stored RCCs to improve the quality before transfusion (Hess, 2006).

## 1.2 Red Blood Cell Storage and Storage Lesion

In general, the half-life of RBCs in the circulatory system is approximately  $120 \pm 4$  days (Palis, 2008). The donated RBCs represent a mixture of different aged RBCs. During storage, the already aged RBCs complete their aging process and lyse before the moment of transfusion (D'Alessandro et al., 2010). Furthermore, the *ex vivo* storage poses a challenge to the RBCs. Unlike *in vivo* circulating RBCs, stored RBCs are exposed to the cell debris which accumulate in the stored RBC suspension. This cell debris may contain reactive constituents, such as aggregated, oxidized or denatured proteins and lipids, which produce far from physiologically normal conditions (Hess et al., 2009; Sparrow, 2010). The conditions in RCCs thus cause a greater and prolonged stress than is usually experienced by RBCs in the human body during their regular lifetime (D'Alessandro et al., 2010). By adding storage solutions, such as phosphate adenine glucose guanosine saline mannitol (PAGGSM) or saline adenine glucose mannitol (SAG-M), red blood cell concentrates can be stored under hypothermically conditions for up to 6 weeks (Cancelas et al., 2015; D'Alessandro et al., 2010).

Blood banks have experienced technical progress in preservation and storage of blood products in recent years, which improve the quality of RCCs and prolong their shelf-life. This has mainly been achieved by the removal of leucocytes (leucoreduction) before storage, which reduces RBC damage caused by cytotoxic mediators released from lysed leucocytes (Heaton et al., 1994; Yazer et al., 2004). In addition, the use of additive storage solutions has led to longer preservation of the cells' metabolic functions during storage, so that the RBC *in vivo* recovery fraction is increased and

complications for patients after transfusion occur less frequently (Arduini et al., 2007; Hess, 2006; Kurup et al., 2003). The RBC *in vivo* recovery fraction is the proportion of blood cells that are not directly filtered by the immune system of the transfusion recipient and that can contribute to the adequate oxygenation of the tissue. Currently, the extracted whole blood is first treated with an anticoagulant (citrate phosphate dextrose (CPD)). After leucocyte depletion, the additive storage solution is added. The present state-of-the-art additive storage solution is PAGGSM (Zehnder et al., 2008). Isotonic PAGGSM reduces hemolysis levels and osmotic fragility after 42 days of storage compared to the hypertonic SAG-M storage solution (Zehnder et al., 2008). During the last few years, clinical institutes have switched more frequently from SAG-M to PAGGSM.

The biochemical and morphological alterations of RBCs during storage are referred to as storage lesion (D'Alessandro et al., 2010; Karon et al., 2009; Sparrow, 2010). Storage lesion only occurs in *ex vivo* storage and modifies the RBC properties and the corresponding supernatant of the RCCs (see Table 1).

**Table 1. Major changes in RBCs and storage medium over storage time.**

Changes occurring to RBCs	Changes occurring in supernatant
<b>Metabolic:</b> <ul style="list-style-type: none"> <li>• Acidosis ↑</li> <li>• 2,3-DPG ↓</li> <li>• ATP (slowed metabolism) ↓</li> <li>• Glutathione, NADH, NADPH ↓</li> </ul>	<ul style="list-style-type: none"> <li>• pH ↓</li> <li>• potassium ↑</li> <li>• Free Hemoglobin (Hemolysis) ↑</li> <li>• Heme and iron (potential redox injuries) ↑</li> <li>• Proinflammatory cytokines ↑</li> <li>• Damaged, oxidized proteins and lipids (biologically active) ↑</li> <li>• Lactate ↑</li> </ul>
<b>Oxidative stress:</b> <ul style="list-style-type: none"> <li>• Protein oxidation (e.g., Band III) ↑</li> <li>• Lipid peroxidation ↑</li> <li>• Lysolipids (cause TRALI) ↑</li> </ul>	
<b>Shape and membrane changes:</b> <ul style="list-style-type: none"> <li>• Morphology shift (Discocytes → Echinocytes → Spherical forms)</li> <li>• Loss of cell membrane (microvesiculation) ↑ <ul style="list-style-type: none"> <li>○ Cell shrinkage</li> <li>○ Deformability ↓</li> </ul> </li> <li>• CD47 expression ↑</li> <li>• phosphatidylserine exposure ↑</li> </ul>	

The most prominent biochemical changes are the following:

- a reduced pH with a decrease in concentration of 2,3-diphosphoglycerate (2,3-DPG),
- a slowed glycolytic activity with a decrease in adenosine 5`-triphosphate (ATP) and nicotinamide adenine dinucleotide (phosphate) reducing equivalents (NADH), and
- a transient loss of ion pumps (Na<sup>+</sup>-K<sup>+</sup>-ATPase activity) with an increase in extracellular potassium (D'Alessandro et al., 2010; Hamasaki & Yamamoto, 2000; Hess, 2010; Karon et al., 2009).

Many changes, such as the reduction of methemoglobin (Korgun et al., 2001), generate reactive oxygen species (ROS) and thereby increase oxidative stress .

Oxidative stress results in oxidative damage, which has been identified as a significant factor in the storage lesion of RBCs (D'Amici et al., 2007; Kriebardis et al., 2008). Among other things, oxidative damage leads to the following outcomes:

- alterations in the structure of the protein band 3 (Bosman et al., 2008),
- spectrin oxidation (Card, 1988; Wagner et al., 1987),
- lipid peroxidation (Tinmouth & Chin-Yee, 2001),
- microvesiculation (Card, 1988) and
- membrane loss (Sparrow, 2010).

These changes all result in alterations to the RBC morphology and in an accelerated aging process, which ultimately ends in RBC apoptosis (Bosman et al., 2008; D'Alessandro et al., 2010; Hess, 2010; Karon et al., 2009). Along with morphological changes, alterations in the mechanical properties of the cells can be observed, which affect the osmotic fragility, the deformability and rheology of the cells (Cardo et al., 2008; Mohandas & Chasis, 1993).

### 1.3 RBC Morphology

Healthy red blood cells (average diameter: 6.2 - 8.2  $\mu\text{m}$  and thickness: 2 - 2.5  $\mu\text{m}$ ) which possess the form of biconcave disc shapes are called discocytes (D) (Tombak, 2019). Discocytes have a typical volume of about 90 fL and a high membrane area to volume ratio.

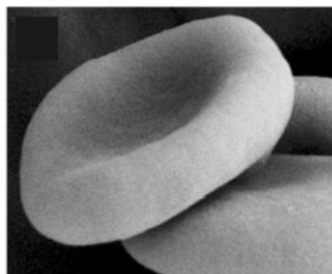


**Figure 1. Scanning electron microscope image of healthy red blood cell (discocyte)** (adapted from (Mesarec et al., 2019)).

Discocytes need only ~50% of the membrane to contain their volume (Hess, 2010; Mohandas & Chasis, 1993). The extra membrane area is crucial for the RBCs' ability to deform and squeeze through the microvasculature or narrow capillaries (Guo et al., 2014; Mohandas & Chasis, 1993). In these narrow capillaries, RBCs are briefly exposed to increased shear stress, causing healthy RBCs to transform temporarily into stomatocyte morphologies if they are exposed to sudden stress (Lanotte et al., 2016). Depending on the shear intensity, the healthy RBCs transform into stomatocytes (ST, cup-shape), deformed stomatocytes (DS, more profound cup-shape) or trilobes (T, triconcave shape) (Lanotte et al., 2016; Mauer et al., 2018; Reichel et al., 2019).

The membrane loss during storage leads to a slow change in the shape of RBCs. They evolve from smooth biconcave discs through intermediate morphological stages, such as subtly bumpy discs (echinocytes1, E1 and echinocytes2, E2) and grossly bumpy spheres (echinocytes3, E3 and spherocytes, SE) to smooth spheres (spherocytes, SP) (see Figure 2 and (Bessis, 1972)). During the echinocytosis degradation pathway, the membrane loss is associated with the expansion of the outer leaflet of the membrane in comparison to the inner leaflet (Melzak et al., 2021). However, there is also a minor proportion of RBCs (about 1%) that acquires a stomatocyte morphology as a temporary stage during storage degradation (Piety et al., 2015). This rare degradation pathway is associated with the expansion of the inner leaflet of the membrane as compared to the outer leaflet (Bessis, 1972; Melzak et al., 2021).

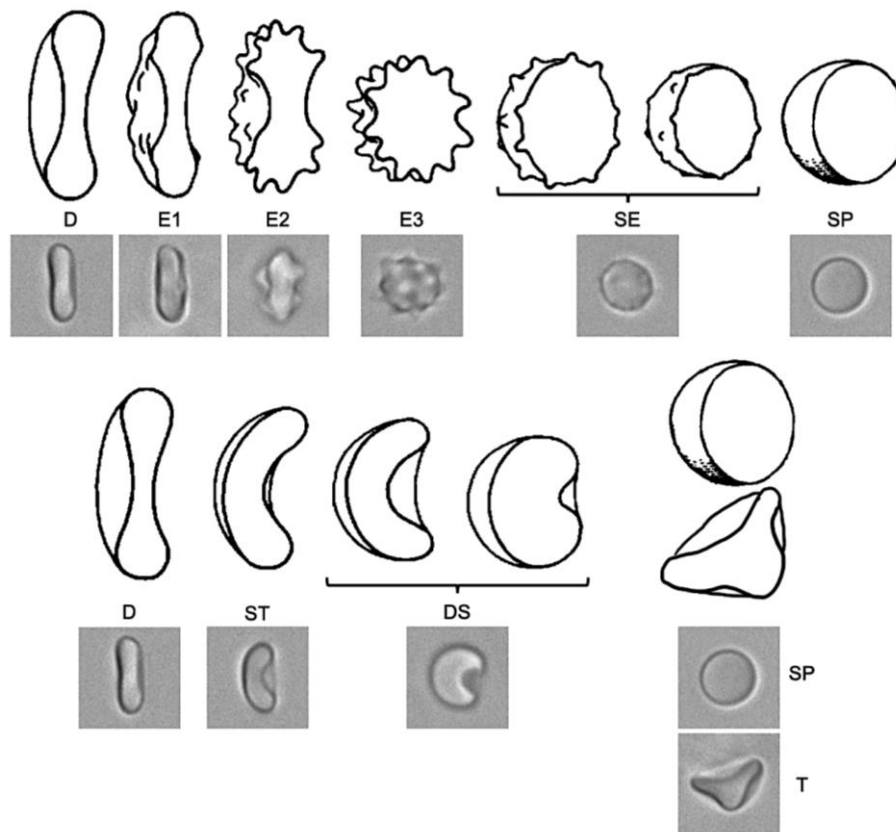


**Figure 2. RBC degradation pathways and shear morphologies as sketches and corresponding RBC micrographs generated by flow morphometry.** The main morphological degradation process of RBCs according to Bessis (Bessis, 1972) is shown in the top line. The degradation process starts with discocytes (D) and develops further through echinocytes1 (E1), echinocytes2 (E2), echinocytes3 (E3), and spherocytes (SP). For this study, the subclasses of spherocytes I and II are grouped as spherocytes. In the bottom line two pathways are shown, which denote the different shear dependent morphologies and the rare degradation pathway via stomatocytes. The shear dependent morphologies start with stomatocytes (ST) and deform further into deformed stomatocytes (DS) and trilobes (T) with increasing shear. The rare degradation pathway via stomatocytes incorporates ST and DS as well, but in the last stage they morph into spherocytes (SP).

The storage-associated shape change can be reversed to a certain degree through a process called rejuvenation (Lockwood et al., 2003), which is mainly characterized by an increase of ATP concentration and the restoration of a normal pH for the RBCs (Hogman et al., 1985). However, at the level of spherocytes, the membrane loss in the form of micro vesicles is too far gone and therefore irreversible (Hess, 2010). Shape changes towards spherical morphologies are associated with rheological changes through decreased deformability and increased viscosity, leading to a disturbed capillary flow and oxygen delivery (Cardo et al., 2008). These negative properties are only present in spherical morphologies. Spherical RBCs are removed by phagocytic cells (macrophages) shortly after they enter the circulatory system through transfusion (Deplaine et al., 2011; Roussel et al., 2021). The infusion and subsequent destruction of larger numbers of these cells can accelerate iron overload

(especially in chronically transfused patients) and thus promote inflammation and infection in the recipient (Bosman et al., 2008; Hod et al., 2011; Hod & Spitalnik, 2011). Therefore, RCCs which have a relatively large concentration of cells with spherical morphologies are considered to have a low quality (Almizraq et al., 2013). Several reports showed a correlation between RBC morphology and storage lesion (Dhabangi et al., 2015; Fergusson et al., 2012; Heddle et al., 2016; Lacroix et al., 2015; Steiner et al., 2015) as well as between RBC morphology and RBC quality (Doan et al., 2020; Hess, 2010; Hess, 2016; Roussel et al., 2017; Roussel et al., 2021).

Currently, the quality of stored RCCs is mainly assessed by quantifying hemolysis. Hemolysis represents the ratio of free hemoglobin (fHb) to the total hemoglobin (Hb) contained in an RCC, scaled by the hematocrit (Hkt) factor. Free hemoglobin in the suspending solution emerges from the rupture of cells or the shedding of RBCs micro vesicles (Hess, 2010). The hemolysis rate depends on the storage duration, the storage solution and the individual donors (Hess et al., 2009). An increase in hemolysis can also reflect a mishandling of RCCs (freezing or heating) or bacterial contamination (Hess, 2010). This wide range of influencing factors means that hemolysis measurement is a good indicator for tracking the deterioration of stored RBCs. Currently, the recommendations of the Council of Europe (European Directorate for the Quality of Medicines & HealthCare, 2020) and the German regulatory guideline (Bundesärztekammer, 2017) set a threshold of 0.8% hemolysis rate in RCCs, above which they need to be discarded. The corresponding threshold in the USA, as recommended by the Food and Drug Administration (FDA), is set to a hemolysis rate of 1% (FDA, 1986). However, hemolysis measurement is a time-consuming and labor-intensive procedure. Furthermore, it is not standardized; different methods to measure the hemoglobin level are used (Han et al., 2010). Due to its complexity, hemolysis is often only checked visually based on the intensity of the red color before transfusion (Janatpour et al., 2004).

Furthermore, despite its widespread acceptance, the hemolysis parameter does not sufficiently reflect some important molecular changes that RBCs experience during storage (D'Alessandro et al., 2010; Glynn et al., 2016). In particular, the post-transfusion recovery of RBCs is not accurately detected by the measurement of hemolysis (Roussel et al., 2017; Roussel et al., 2021). This led to growing concern regarding the safety and efficacy of stored red blood cell concentrates which are checked only by hemolysis measurement (D'Alessandro et al., 2010; Glynn et al.,

2016). According to Glynn et al., the hemolysis variable was developed before the clinical outcome studies were performed on RBCs of different storage age and it does not reflect either the nature of the storage lesion elements and quality of RBCs or the efficacy of RBC transfusions in different patient populations (Glynn et al., 2016).

#### 1.4 Morphological Analysis of RBCs

Additional information about the safety and efficacy of stored RBCs can be obtained by morphological analysis, a method that has the potential to ensure an easy and practical diagnosis (Blasi et al., 2012; D'Alessandro et al., 2010; Doan et al., 2020). The gold standard for morphological analysis of RBCs is a visual observation of a blood smear under a light microscope. Prior to characterization, a blood smear assay requires smearing, fixing and staining of the erythrocytes on a microscope slide (Acker et al., 2014). The characterization is performed by visual examination of between 200 and 1500 cells (Berezina et al., 2004; Blasi et al., 2012; Piety et al., 2015). The cells are sorted into different classes and multiplied by a designated fractional weight, resulting in a percentage score that evaluates the sample (Tchir et al., 2013). However, the typical blood smear assay is labor-intensive, limited by its small sample sizes and prone to manual bias (Doan et al., 2020; Sierra et al., 2017).

##### 1.4.1 Microfluidic Analysis Systems

As an alternative to blood smears, microfluidic systems that analyze suspended RBCs in flow can provide fully automated morphological diagnosis based on image analysis with a larger statistic of cells (Piety et al., 2015; Pinto et al., 2019; Sierra et al., 2017). The distinctive feature of these techniques is their ability to generate large amounts of image-data in a short time. This enables comprehensive data analysis and robust signals. Research groups have used different microfluidic systems, such as custom-made flow chambers for single-cell layer flow (Piety et al., 2015), commercially available larger flow chambers for multi-cell layer flow (100  $\mu\text{m}$  height) (Sierra et al., 2017) and imaging flow cytometry (IFC) for single-cell flow (Pinto et al., 2019).

However, classification systems for RBCs in laminar flow (which are typical for this type of microfluidic systems) must take into account that certain rheological effects may influence the classification results (details follow in section 2.2.1). For example, cells with the same morphology can be imaged in different shapes depending on their random orientation. Moreover, when the shear stress in the flow reaches values in the order of 1 Pa, this can result in certain artefacts. First, regular and flexible discocytes will orient themselves according to the velocity gradient in the laminar flow and adopt a rolling motion (Dupire et al., 2012; Sierra et al., 2017). Second, the shear stress of this magnitude can also induce healthy discocytes to reversibly change shape into artefactual stomatocyte morphologies (Abkarian et al., 2008; Lanotte et al., 2016; Mauer et al., 2018; Otto et al., 2015; Reichel et al., 2019). In a microscopic life video, Lanotte et al. demonstrated how cells with shear induced stomatocyte morphology revert to discocytes within a very short time (1.2 s) after the shear had stopped (Lanotte et al., 2016). The stomatocyte morphology proportions generated in this process far exceed those of the rare stomatocyte degradation pathway mentioned above. This is also true for IFCs, as the cells are exposed to similar laminar flows that arise in other microfluidic systems. These laminar flows are generated in the injection nozzle microseconds before hydrodynamic focusing in the flow chamber (this a particularly shear gentle type of cell flow which is specific to flow cytometry).

These various effects can occur even under “moderate” flow conditions, since in laminar flow channels the shear stress increases linearly, starting from zero in the center of the flow and reaching maxima at the wall surfaces. In this way, the shear stress covers a certain range of values, which depends on the flow rate. Interestingly, this effect has not been explicitly discussed in studies of RBC degradation based on microfluidic systems.

#### 1.4.2 Flow Morphometry System

Two decades ago, the first *in situ* microscope (ISM) was introduced for real-time monitoring of microorganisms in agitated bioreactors (Suhr et al., 1995). The advantage of non-invasive *in situ* microscopy is that it allows imaging of cells directly in a flowing suspension. This technique enables both virtual sampling of cells on a large scale and simultaneous online analysis using image processing. In this way, a

significant automation advantage is achieved which eliminates the need for sample collection and allows for large-scale data acquisition that can undergo rapid statistical analysis. The principle of ISM also does not require cell labeling, which greatly simplifies the technique, allowing non-invasive examination of suspended cells in flowing suspension. The ISM circumvents the negative effect of motion blur at the moment of imaging moving cells by controlling the exposure time of the camera sensor and the illumination duration. By generating short pulses of light, images of moving cells are captured without blurring.

(Sierra, 2017) developed the flow morphometry system which is used in this study through the combination of the *in situ* microscope and a commercially available flow chamber (see Figure 3). According to this method, the ISM system was placed below the flow chamber realizing an inverted microscope. The system is described in more detail in 2.2.

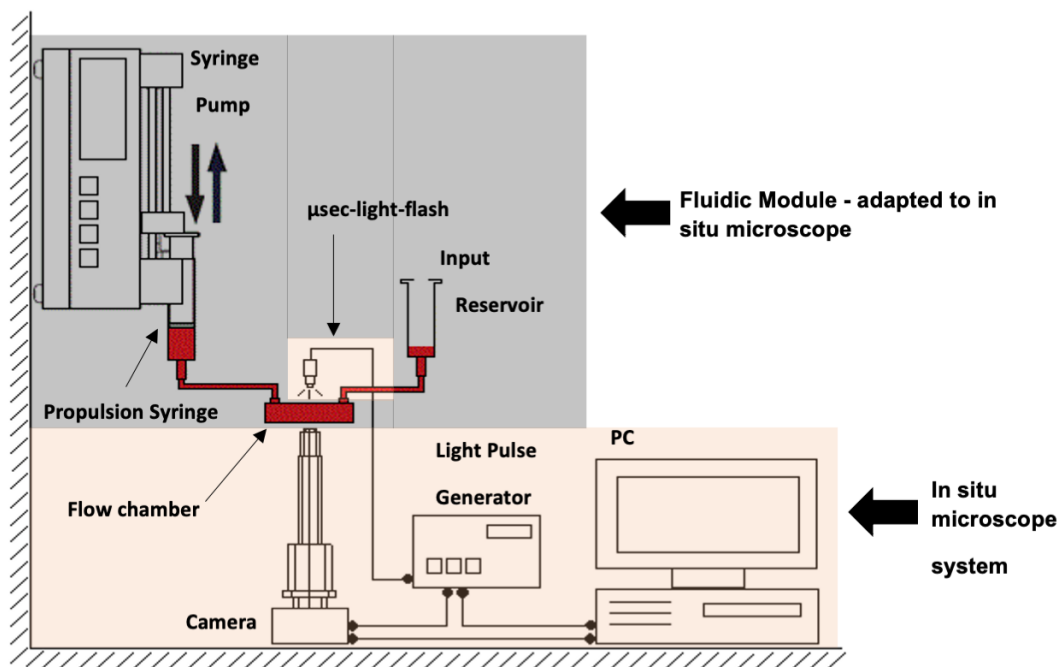


**Figure 3. Adaption of *in situ* microscope with fluidic module.** Erythrocyte suspension flows through a flow chamber and is imaged by the inverted *in situ* microscope from below. The microscope captures images from the depth of field within the suspension flow, which is illuminated by microsecond light flashes from above the flow chamber (adapted from (Sierra, 2017)).

In his work (Sierra, 2017), Sierra uses a decision tree-based image processing algorithm to classify RBC morphologies into three distinct sets (Discocytes, echinocytes and spherocytes) (see Figure 4). The classification of different RBC

morphologies in a decision tree algorithm is based on only a few morphological characteristics, otherwise the algorithm becomes too complex to handle. Sierra uses four morphological features (border roughness, non-circularity, texture inhomogeneity and equivalent diameter) to perform the classification of the RBC morphologies. Through this flow morphometry system (Sierra et al., 2017) a suitable candidate for a morphological storage lesion marker could be identified in a first approach. However, due to the low classification resolution (three morphology-classes), possible influences of the measurement system on the cells by shear-induced morphology changes could not be detected.

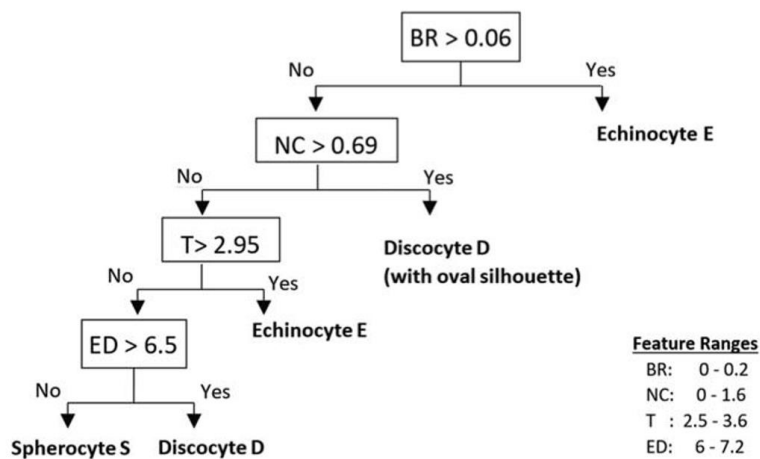


**Figure 4. Binary decision tree for classification of RBCs.** At the first ramification superficial bumps and spikes (echinocytes) are detected through the border roughness (BR). Smooth oval contours (discocytes) and round spherocytes with small bumps are recognized by the non-circularity (NC) and the texture inhomogeneity (T), respectively. In the last ramification, smooth spherocytes are distinguished from non-oriented discocytes by the equivalent diameter (ED) (adapted from (Sierra et al., 2017)).

## 1.5 Application of Neural Networks

To study degradation- and shear-induced morphologies simultaneously, a sufficiently accurate classification of RBC morphologies is required. In the previous microfluidic systems mentioned above, the RBC-classification has been performed using decision tree algorithms that are limited in terms of differentiable morphological resolution (Pinto et al., 2019; Sierra et al., 2017) and/or its sensitivity and specificity (Piety et al., 2015). A more refined discrimination of morphology classes can be obtained by using convolutional neural networks (CNNs).

Neural networks (NNs) are based on mathematical models of the function of neurons in the brain and enable a special kind of machine learning. This kind of machine learning finds patterns in analyzed data, such as images, without a conventional hand-written deterministic image analysis algorithm (Koza, 1996). Not only numerical datasets but also image-, audio- and text-data can be used (Bishop & Nasrabadi, 2006).

The building blocks of NNs are artificial neurons, which simulate the function of brain neurons. An artificial neuron is a mathematical function that can process multiple inputs. Each input has a weight whose value indicates how important that input is to the output (Ash, 1989) (see Figure 5). The weights represent the actual memory of an NN for specific classification tasks, as they are adapted during the training process. For example, an input can be a pixel value of an image. The neuron multiplies each input by its weight and adds them together (Schmidhuber, 2015). The sum is used as a variable in an activation function, which in the simplest case is a threshold. If the weighted sum is greater than this threshold, the output is either 1 or 0 (most activation function have continuous outputs). As a result of this, the weights decide which neuron connections are to be used for the different input images during a classification task.

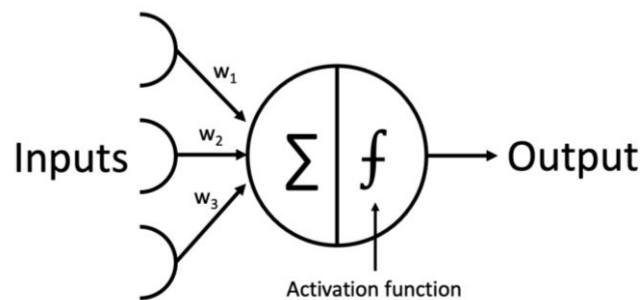


**Figure 5. Artificial neuron as building block of NNs.**  $w_i$  denotes the weights and  $f$  denotes the activation function.

Many neurons which stand in parallel and which are not connected to each other form a layer (Oja, 1989). When one layer is connected to another, the outputs of the first layer become the inputs of the next layer, and when each output is connected to every neuron in the next layer, these layers are called fully connected layers (Bishop & Nasrabadi, 2006). Several layers connected in series form a neural network. The simplest NNs (see Figure 6) consist of two to four layers, and they are called shallow

neural networks. The input layer is the layer into which the input values are fed. The layers in between are called hidden layers and perform the actual classification. The output layer has the same number of neurons since the network has different classes into which the input values are to be sorted. The NN in Figure 6, for example, has two classification classes because of the two neurons in the output layer. Every layer has a unique functionality, performs feature extractions or finds patterns.

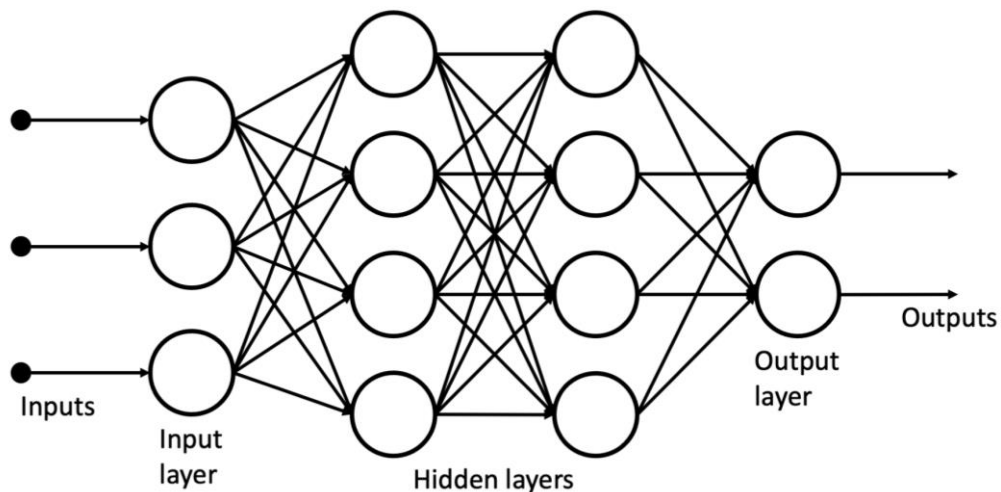


**Figure 6: Diagram of shallow neural network.** The simplest form of a NN.

Convolutional neural networks (CNNs) are a special type of NNs which are optimized for image data analysis and which can recognize and classify specific objects in digital images (LeCun, 1989; LeCun, 1998). In a CNN, the number of weights (the actual memory for specific classification tasks) is dramatically decreased compared to a fully connected network. This lower effort with respect to weights is only possible because of the convolutional structure of the layers. A convolutional layer maps the input to an output map by sliding a kernel over the input values and computing the convolution (via element-wise multiplication, or the so-called Hadamard product) of the input with the kernel (see Figure 7). The results are calculated and then passed through an activation function. In a convolutional layer more than one kernel can be used simultaneously. In this way, each kernel represents an own artificial neuron with its own activation function.

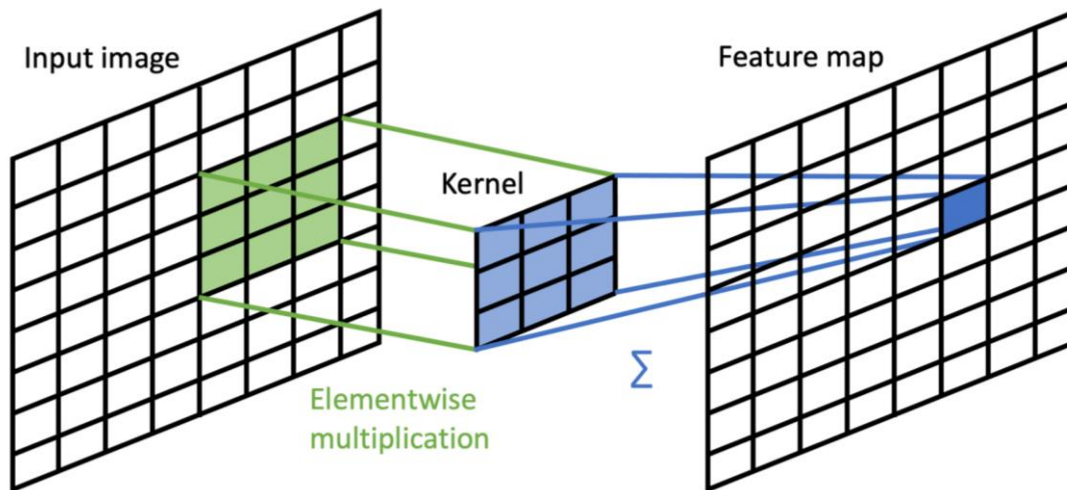


**Figure 7. Convolutional layer diagram.** Convolutional stage with an input image, the kernel and an output map. In this diagram the convolutional layer has a kernel size of 3x3 convolution.

Kernels can be seen as filters for images, each of which has a specific pattern optimized, for example, to detect horizontal or vertical edges. In this way, the CNN only has to remember the values of the kernel that represent the weights of the convolutional layer.

## 1.6 Flow Morphometry applied to Air Rescue RCCs

To validate our flow morphometry system, we applied it in a pilot study in which RCCs were transported via helicopter as emergency prehospital transfusion.

The integration of clinical transfusion therapy already in the prehospital care of severely injured patients was first implemented in the military (Shackelford et al., 2017) and more recently in the civilian sector in a few European and non-European countries (Karl et al., 2016; Lockey et al., 2013; Thies et al., 2020). The benefits of prehospital transfusion have been documented at length, particularly when patients need to be transported long distances (Brown, Cohen, et al., 2015; Brown, Sperry, et al., 2015; Griggs et al., 2018; Rehn et al., 2019). Short patient transport distances are currently being investigated in some countries (Brown, Sperry, et al., 2015; Lockey et al., 2013; Lyon et al., 2017).

Several aspects need to be considered in prehospital transfusion: severity of trauma, urgency of immediate transfusion, high risk of hemorrhagic shock and the limited

availability of blood products (AWMF, 2012). The use of air ambulance seems particularly useful, as it allows for long ranges to be covered and short transport times. In order to perform air ambulance transport for prehospital transfusions in Germany, the requirements of the Hemotherapy Guidelines, the Transfusion Act, and the Cross-Sectional Guidelines for Therapy with Blood Components and Plasma Derivatives of the German Medical Association (BÄK) must be followed (Bundesärztekammer, 2017, 2020). The details of the specifications for the transportation and storage of RCCs are crucial.

Currently, there is limited information available regarding the transport logistics of RCCs in an air ambulance, particularly with respect to repeated transport, total flight time, re-entry into regular blood bank storage and coping with the limited availability of blood products. In current German pilot projects, a concept has been established in which RCCs are transported for up to three days and then transferred back into regular blood bank storage and use (Brade et al., 2020; Selleng, 2020). Dr. Sitzmann, a colleague of mine, developed a rotation system with one day of transport, one day of quarantine storage, and one day of storage throughout the entire RCC shelf life, due to regulatory requirements. A resource-saving concept is key for the application of air ambulance based prehospital transfusions in emergency cases, as helicopters typically carry rhesus D-negative RCCs of blood group 0, which can be given to any recipient. However, due to their versatility, RCCs with blood group 0 are the most valuable (in the sense of being the most important and rare) RCCs and should therefore not expire.

Previous studies already indicated that helicopter transport (e.g., large temperature fluctuations, air pressure changes and vibration) did not affect RCC quality as compared to control groups (Brade et al., 2020; Otani et al., 2012). However, a detailed analysis of RCC quality after repeated transport throughout the shelf life of blood components with varying flight times is currently lacking.

## 1.7 Aim of the Study

My work is divided into three parts: i) I introduce the CNNs in the image processing of the flow morphometry system as a further development of decision tree-based algorithms, ii) I develop a robust marker for storage lesion based on morphological analysis with CNNs, and iii) I apply this new developed storage lesion marker in the case of repeated air rescue mission transport for prehospital transfusion.

- i) We use CNN-based image processing in order to strongly improve the resolution of the morphological classification of RBCs in our flow morphometry system, compared to our formerly used decision tree-based classification. This should enable the determination of degradation-induced morphologies at a high resolution simultaneously with shear-induced morphologies in RCCs. With the improved classification resolution provided by the CNNs, we believe that we will be able to acquire a deeper understanding of RBC shape changes during storage of RCCs. To validate the CNN-based classification, we will compare it to manual reference classification as well as to the formerly used decision tree-based classification.
- ii) We aim to develop a robust marker for storage lesion based on morphological analysis with flow morphometry. This storage lesion marker should generate additional information about the post-transfusion survival of RBCs. For this aim, it is essential to establish a CNN that ensures an improved classification resolution with high sensitivity and specificity for all classes during storage of RBCs. Based on this new data, the definition of a morphological parameter for the monitoring of storage lesion can be optimized. This morphological parameter should correlate with hemolysis levels to confirm compliance with regulatory guidelines for quality control of RCCs. Furthermore, it is necessary to investigate to what extent the shear in our microfluidic system affects this potential storage lesion marker and which standardizations on the system can generate a more robust measurement.
- iii) We will use the newly developed morphological storage lesion marker, together with other biochemical parameters, to conduct the largest progressive study to date of RCC quality after repeated air rescue mission

transport for prehospital transfusion. For this study, a regulatory compliant rotation system had to be developed, which was then assessed by analyzing biochemical parameters and RBC morphology.

## 2 MATERIALS AND METHODS

### 2.1 Materials

#### 2.1.1 Devices, Components and Reagents

**Table 2: List of devices, components and reagents used in this study.**

<b>Devices, Components and Reagents</b>	<b>Reference</b>	<b>Manufacturer</b>
Syringe Pump	Legato 270	KD Scientific Inc, Holliston, MA, USA
In Situ Microscope – Light Pulse Generator		Hochschule Mannheim, Mannheim, Germany
In Situ Microscope – Camera	A102f	Basler, Ahrensburg, Germany
In Situ Microscope – Water Immersion Objective	40x – NA 0.75	Lomo, St. Petersburg, Russia
Dovetail Carrier 75 mm Width	55-340	Edmund Optics, Barrington, USA
Flow Chamber	VI <sup>0.1</sup>	Ibidi GmbH, Martinsried, Germany
Female Luer Lock Connector	10825	Ibidi GmbH, Martinsried, Germany
Male Luer Lock Connector	10824	Ibidi GmbH, Martinsried, Germany
Silicon Tube (1.6 mm inner diameter)	TYGON ND 100-65	Reichelt Chemietechnik GmbH + Co., Heidelberg, Germany
Plastic Syringe 2.5 mL		Terumo Deutschland GmbH, Eschborn, Germany
Pigtailed Luminescence Diode	650 nm/2A	DieMOUNT, Wernigerode, Germany
Sodium Chloride	NaCl 0.9%	B.Braun Melsungen AG, Melsungen, Germany
Blood Collection Bag System	CompuFlow	Fresenius Kabi AG, Homburg, Germany

Devices, Components and Reagents	Reference	Manufacturer
ATP Hexokinase FS	1 6201 R	DiaSys Diagnostic Systems GmbH, Holzheim, Germany
Buffer Solution	fHb	Bioanalytic GmbH, Freiburg, Germany
Automated Blood Separator	Compomat G4	Fresenius Kabi Deutschland, Germany
Hematology Analyzer	CELL-DYN Ruby	Abbott GmbH & Co. KG, Wiesbaden, Germany
Centrifuge	Rotina 38	Hettich GmbH & Co. KG, Tuttlingen, Germany
Spectrophotometer	DR 5000	Hach Lange GmbH, Düsseldorf, Germany
Blood Bag Rotator	ACR Rotator	LMB Technologie GmbH, Schwaig, Germany
Temperature Data Logger	ThermoScan Datenlogger™	TRANSMED, Nürnberg, Germany
Cooling Box	Pelican Crēdo ProMed™ 4-L	PELI Biothermal™, Plymouth, MN, USA
DRF Rescue Helicopter	Airbus EC 135 helicopter – Christoph 53	Airbus Helicopters, Marignane, France
Blood Gas Analyzer	ABL 80 Flex	Radiometer GmbH, Krefeld, Germany

## 2.2 Flow Morphometry Setup

### 2.2.1 Fluidic System and Fluid Dynamics

**Fluidic system.** The experimental setup is shown in Figure 8. It is based on an *in situ* microscope as described briefly in section 1.4.2 and explained in further detail in Sierra 2017, Suhr 2015 and Wiedemann 2011. The system captures images of RBCs moving in a flowing suspension.

The microfluidic chamber used is made of hydrophobic polymer (ibidi GmbH, Martinsried, Germany) with dimensions of 17 x 1 x 0.1 mm (L x W x H) and a total volume of 1.7  $\mu$ L. The bottom of the flow chamber is made of a transparent polymer

slide (thickness = 180  $\mu\text{m}$ ), similar to a cover glass and with a low birefringence, whose optical quality is suitable for high resolution light microscopy. The microfluidic chamber is coupled through silicon tubing (1.6 mm  $\varnothing$ ) with two syringes (2.5 mL, Terumo Deutschland GmbH, Eschborn, Germany). One syringe (without piston) only serves as an input reservoir. The other syringe is clamped in a syringe pump (Legato 270, KD Scientific Inc, Holliston, MA, USA). The syringe pump moves the RBC suspension through the microfluidic chamber with a flow rate of 0.1 mL/min. The flow rate corresponds to a mean velocity of 1.67 cm/s in the flow chamber. The fast passage of the cells through the sample volume of the microscope ensures the uncorrelated imaging of individual RBCs between consecutive frames.

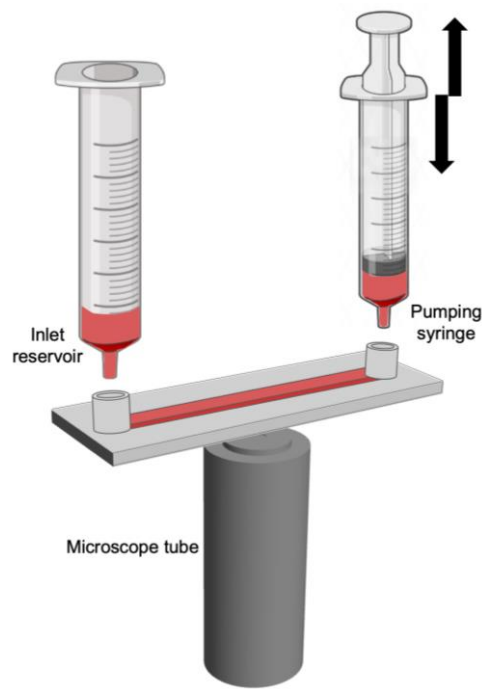


**Figure 8. Fluidic system.** The RBC suspension is moved through a microfluidic chamber by a syringe pump. The cell suspension moves cyclically with a constant flow rate of 0.1 ml/min. The flow chamber is coupled to an inverted microscope. Syringe illustrations modified from bioRender.

**Fluid Dynamics.** The dimensions of the channel provide a uniform flow across the channel width of 1 mm. The fluid velocity used creates a laminar flow within the flow chamber. Here, laminar flow corresponds to a Reynolds Number ( $Re$ ) of 137. A flow is considered laminar when the  $Re$  of the fluidic structure is less than 2000 (Batchelor, 1967). The Reynolds number is obtained as follows:

$$Re = \frac{\rho \bar{v} D_h}{\eta},$$

where

$\rho \approx 1 \text{ g/cm}^3$  Density of the medium (0.9% NaCl; 20°C)

$\bar{v} = 1.67 \text{ cm/s}$  Mean flow velocity

$\eta = 1.0 \cdot 10^{-3} \text{ Pa} \cdot \text{s}$  Dynamic viscosity (0.9 % NaCl; 20°C)

$D_h = 2 \cdot W = 1 \text{ cm}$  for  $W \gg H$  Hydraulic diameter

According to (Eibl et al., 2009), the local flow velocity  $v$  is defined as a function of the height position  $h$  above the bottom surface for a given flow rate  $F$ , channel height  $H$  and width  $B$  as follows:

$$v(h) = \frac{6F}{B \cdot H^3} |(Hh - h^2)|$$

The velocity gradient (shear rate) causes a shear stress of zero at the center of the flow and maximal at the inner wall surfaces. The shear rate is determined by the following equation:

$$\text{shear rate} = \dot{\gamma}(h) = \frac{6 \cdot F}{B \cdot H^3} \cdot |(H - 2h)|$$

and the corresponding shear stress is given by:

$$\tau = \eta \cdot \dot{\gamma}$$

Due to the highly diluted RBC samples in the 0.9% NaCl solution (see 2.3 and 2.5.3), no shear thinning effects are to be expected. Within the parameter set for the flow channel, a shear rate of  $760 \text{ s}^{-1}$  can be calculated at a height  $h$  of about  $12 \text{ }\mu\text{m}$  above the bottom surface as well as at a distance of  $12 \text{ }\mu\text{m}$  from the top surface. The shear stress at these positions is accordingly calculated as follows:

$$\tau = \eta \cdot \dot{\gamma} = 0.76 \text{ Pa}$$

At such values of shear stress in a laminar flow channel, the healthy discoid RBCs adopt a motion as if they were rolling on a surface parallel to the channel walls and in the direction of flow. This phenomenon is called rolling mode (Dupire et al., 2012; Sierra et al., 2017). The microscopic images of cells in rolling mode are elongated ovals aligned along the flow lines. This is a distinct morphological feature that clearly distinguishes discocytes from spherocytes and other morphologies (see Figure 21).

For this reason, the volume of the microscopic sample is adjusted to the position of the rolling mode. The corresponding experimental setup is shown in Figure 9.

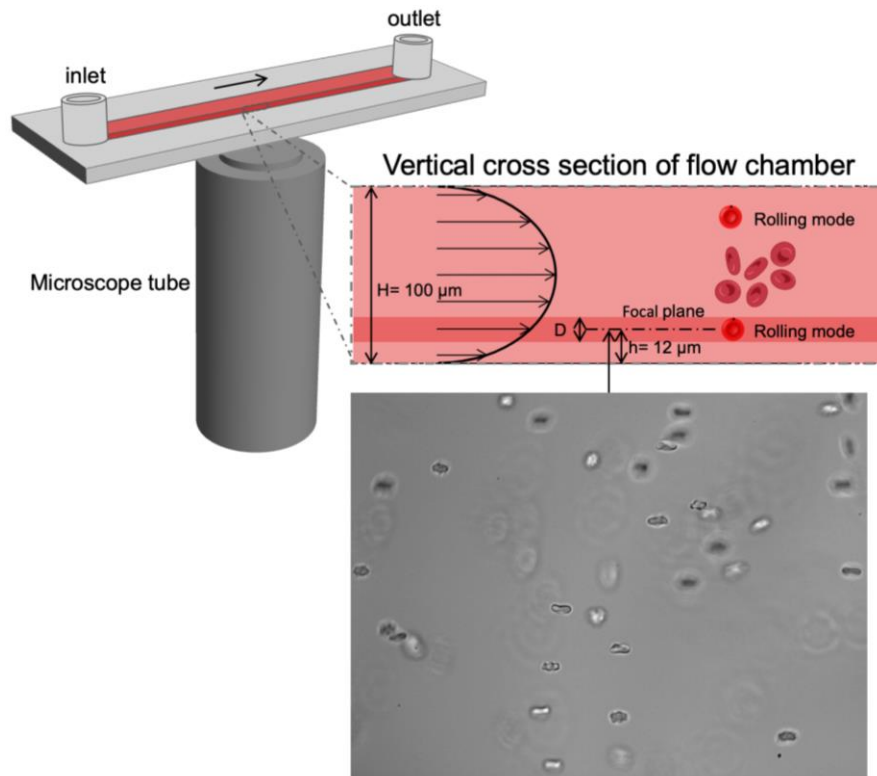


**Figure 9. Microscopic system and image acquisition.** The RBC suspension is moved by a syringe pump through a microfluidic chamber and imaged with an inverted microscope. The laminar flow manifests a parabolic velocity profile and a linearly varying shear rate over the channel height ( $H$ ). Images are acquired in a narrow focal range ( $D = 8 \mu\text{m}$ ) that covers only a thin layer within the entire channel height. Only the RBCs inside this sample volume surrounding the position of the focal plane ( $h$ ) are visible as sharp objects.

### 2.2.2 Microscopic System

For the microscopic visualization of RBCs in a laminar flow, an immersion objective (water immersion, 40x, NA 0.75, Lomo, St. Petersburg, Russia) is placed below the flow chamber (see above). Images are acquired with a 1392 x 1040 pixel CCD camera with a sensor size of 2/3" (A102f, Basler, Ahrensburg, Germany). The flow chamber is illuminated from above by a pigtailed luminescence diode (DieMOUNT, Wernigerode, Germany; 630 nm/2 A, 1 mm  $\varnothing$ ). The parameters of the light pulses are as follows: pulse width = 2  $\mu\text{s}$ , pulse frequency (= frame rate) = 15 Hz. The depth of field (effective focal range) is about 8  $\mu\text{m}$ . Only cells inside this narrow focal range appear as sharply imaged objects. The position of the focal plane in the flow channel can be set with

micrometer precision. This allows any focal plane height to be set within the total height (100  $\mu\text{m}$ ) of the flow channel. During measurement, the focal plane height is normally set to 12  $\mu\text{m}$  above channel bottom. If concentrations are measured as a function of height  $h$ , the sample volume is scanned through the range of height values by adjusting the position of the objective relative to the flow chamber.

### 2.2.3 Software Platforms

The experimental part of the flow morphometry, i.e. the acquisition of the images, is performed by the software platform ISM viewer (Asanza, 2009) (Hochschule Mannheim, Germany). The ISM viewer is a graphic user interface that controls the operation mode of the camera and the light pulse generator (which produces short light flashes emitted by the luminescence diode). The short LED-flashes (2  $\mu\text{s}$  pulse duration) and the image capturing of the camera are synchronized so that images without motion blur are captured at a desired image acquisition frequency (frame rate). The software is programmed in C# language and works on the latest version of Windows (32 or 64 bits, Windows 7 and 10).

We performed the image processing of the acquired RBC images and the CNN classification in the matrix-based MATLAB language (version R2019b, MathWorks Inc, Natick, MA, USA). MATLAB provides a software platform with prebuilt libraries for engineering computations and data analysis in various scientific fields. For this study, we had to install different MATLAB toolboxes for image processing and CNN application. For the image processing functions we used the *image processing toolbox*. The CNN application was realized by using the following toolboxes: *deep learning toolbox*, *parallel computing toolbox* and *statistics and machine learning toolbox*.

### 2.2.4 Image Processing

The captured images are processed by a custom-made algorithm which was developed in MATLAB (Halblaub, 2019; Sierra, 2017). Before segmenting individual cells, the background brightness is compensated to eliminate vignetting. An individual

micrograph (70 x 70 pixels) is created for each detected cell. An overview of the image processing steps is shown in Figure 10.

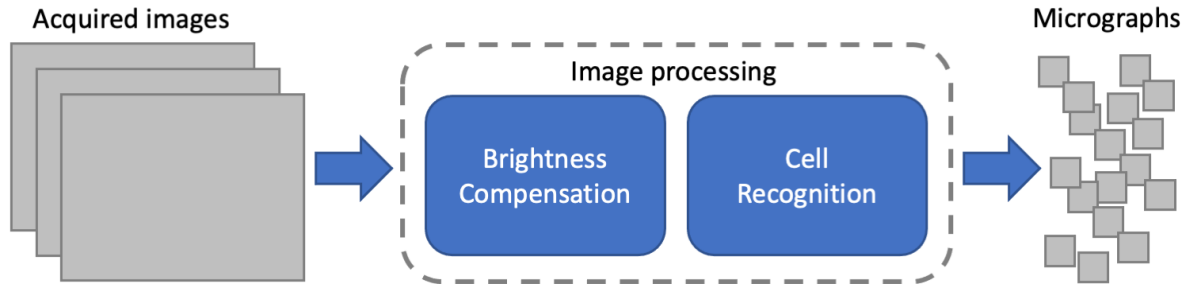


**Figure 10. Image processing overview.** The image processing of the acquired RBC suspension images is divided into two parts, the brightness compensation and the cell recognition. Through these steps sharp cells are segmented as RBC micrographs.

For the brightness compensation, the first 30 images of each sample are used. An array is created from these 30 images and in each pixel the most frequent grayscale value (mode) is determined. These mode values constitute the grayscale values of the background image ( $I_{BG}$ ) in the corresponding pixels. The background image represents the illumination pattern without any cell images. In this way it can be used as a compensation for the vignetting of each new input image ( $I_{IN}$ ). Each grey value of the input image is divided by the corresponding gray value background, creating a new image  $I_{DIV}$  with a uniform background intensity. In addition, a standard mean grey value of 160 is established by multiplying the constant factor  $\frac{160}{255}$ . All in all, the compensation of the raw input image is obtained by pixelwise calculation as follows:

$$I_{com} = \left(\frac{160}{255}\right) \frac{I_{IN}}{I_{BG}}$$

where

$I_{IN}$  is a grey value of the input image pixel,

$I_{BG}$  is a grey value of the background image pixel, and

$I_{com}$  is a grey value of the fully compensated image pixel.

The background compensation process is shown in Figure 11.

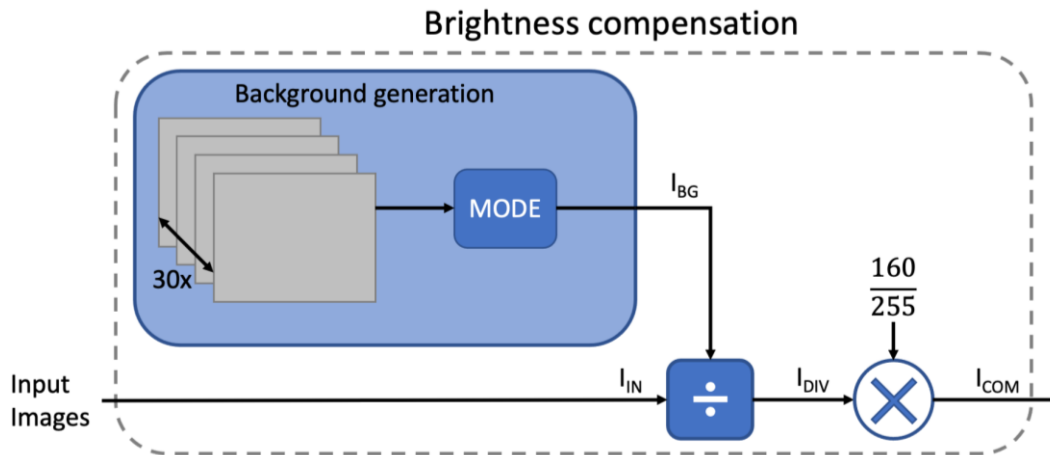


**Figure 11. Brightness compensation.** The first 30 input images are used to create an array as a basis for the calculation of the background image by the mode in the third dimension ( $I_{BG}$ ). Each input image  $I_{IN}$  is then divided by the background image. The resulting  $I_{DIV}$  is then standardized via multiplication by a preset gray value of 160. Finally, the compensated input image is labelled as  $I_{COM}$ . Figure modified from (Sierra, 2017).

The compensated images  $I_{COM}$  are used for the cell recognition. All sharp cells are selected in the images and small cell micrographs (70 x 70 pixels) are created. First, the compensated images are passed through a Gaussian low-pass filter that eliminates high-frequency noise. The low-pass filtered images are then reduced by a factor of 2 in each dimension. This process generates a compressed image ( $I_{SC}$ ) with 4 times fewer pixels than the original image. It is filtered again through a second low-pass filter. Subtracting the low-pass filtered image ( $I_{LP}$ ) from the original reduced image ( $I_{SC}$ ) produces a high-pass filtered image version ( $I_{HP}$ ) of the original image. The high-pass filtered image ( $I_{HP}$ ) has both positive and negative decimal values related to the brightness of the background. Therefore, the image is binarized by assigning pixels of interest (sharp cell) to "1" and the remaining to "0". This is achieved according to two predetermined thresholds for positive and negative pixels, respectively. The binarization is carried out with two binary images ( $I_{TL}$  and  $I_{TH}$ ) for positive and negative brightness changes (regions of sharp objects) in the original image  $I_{SC}$ . In this way the  $I_{TL}$  image represents negative brightness changes and  $I_{TH}$  positive brightness changes. Both binary images are added by the logical operation XOR in order to obtain a binary image ( $I_B$ ) with all information. The binarized image ( $I_B$ ) allows the creation of regions that correspond to the cell structure (high contrast regions) and can be recognized as an object (see Figure 12). These initial cell recognition steps have been explained in greater detail in (Halblaub, 2019; Sierra, 2017; Sierra et al., 2017).

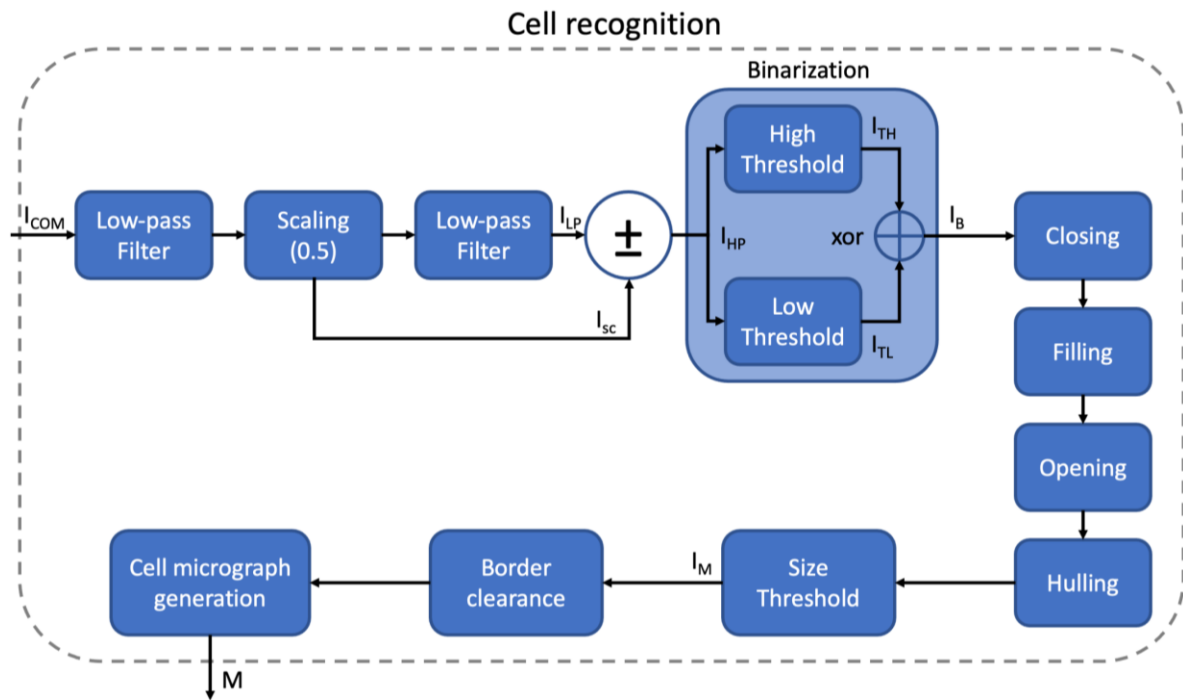


**Figure 12. Cell recognition.** The brightness-compensated image  $I_{COM}$  is filtered and scaled before binarization ( $I_{HP}$ ). During binarization XOR carries out the logical operations exclusively OR in between the two binary input images  $I_{TH}$  and  $I_{TL}$ . Afterwards, morphological operations are performed on the binarized image  $I_B$  (closing, filling, opening and hulling). Finally, the cell micrographs  $M$  are extracted from the binary image  $I_M$  by generating a bounding box around each cell. Figure modified from (Sierra, 2017).

After binarization, a series of closing, filling, opening and hulling steps combined with an elimination of small fragments is performed. A final size threshold eliminates bright blurred cells and clumped cells. As a result, the binary images contain only blobs for each identified cell. A blob is defined as a group of contiguous pixels that form a single object, i.e., a sharp imaged cell. As a last step, the resulting bounding box around each blob is used to extract cell micrographs ( $M$ ) (70 x 70 pixels) from the compensated full-size image.

## 2.2.5 Convolutional Neural Network (CNN)

CNNs are neural networks that are particularly efficient at recognizing and classifying specific objects in digital images when they have been pre-trained with these types of objects (LeCun, 1989; LeCun, 1998). In this study, we adopted the CNN architecture from GoogLeNet to classify different RBC morphologies. GoogLeNet is a deep network (Zhang, 2018) that uses the special features of inception modules with dimensionality reduction (Szegedy et al., 2015) (see Figure 13).

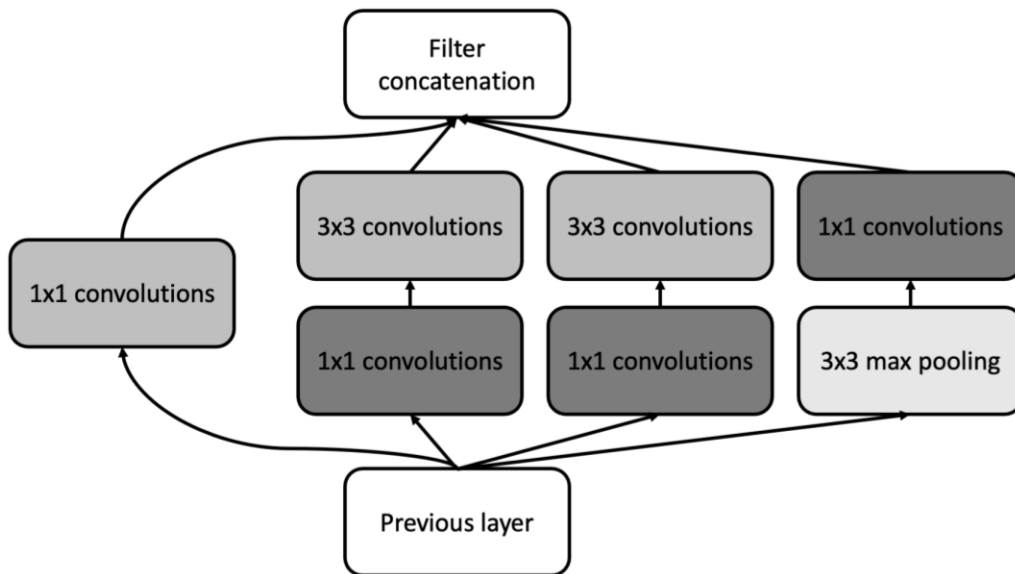


**Figure 13. Inception module.** GoogLeNets' main architecture consists of nine inception modules arranged in a consecutive way.

Inception modules use different sizes of convolutional kernels simultaneously (1x1, 3x3, 5x5 and max pooling) to cope with larger differences in the feature scale. A larger feature scale is more suitable for information that is distributed more globally, while a smaller feature scale is preferred for information that is distributed more locally. The extra 1x1 convolutions are used to compute dimensional reductions before the dimensional expensive 3x3 and 5x5 convolutions. Each convolutional kernel can be seen as a filter with a specific pattern that is optimized to detect certain features in the images. Examples of kernel patterns are given in Figure 14.

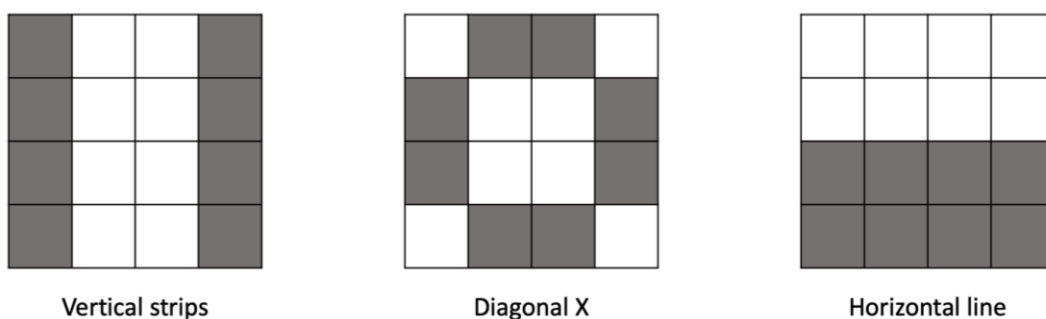


**Figure 14. Examples of Convolutional kernel structures.** Each kernel has a different pattern to extract a certain feature of the input images.

Inception is defined as a deepening of the network in the horizontal direction (Szegedy et al., 2015). A deepening of a network means that the number of layers is increased and the network becomes larger, so it is considered deeper. Deepening is usually performed by adding more layers to the network (thereby increasing its length). A network can also become deeper by increasing the numbers of artificial neurons in a layer (thereby increasing the width), which is considered akin to deepening in the horizontal direction. Deep networks can represent more complex features (e.g., different spatial perspectives of objects of the same class), which increases the robustness and performance of the model (He et al., 2016). The architecture of GoogLeNet is shown in Supplementary Figure 1. GoogLeNets' neurons are trained to classify general objects in images. This means that the convolution kernels and weights must first be trained for specific objects, such as red blood cells in this study. Training of the CNN requires a large and representative collection of data that is manually pre-classified.

### 2.2.6 Organization of the Data and CNN Training

We used two sets of samples: dataset A, which was derived from twelve RCCs, and a preexisting dataset B (Sierra et al., 2017), which consisted of five fresh RCCs. We classified the image data from set A manually and used it exclusively for the training of the CNN (section 3.2). After training, we used the resulting CNN to classify the image data from set B. The classification of set B represents the experimental results from sections 3.3 and 3.4.

**Table 3. Data organization.**

Dataset:	Sample size	Measurement weeks:
A	12 RCCs	0, 1, 2, 3, 4 and 5
B	5 RCCs	2, 5, 6, 8, 10 and 12

To produce the image data for CNN training, we monitored set A (twelve RCCs) for five weeks on a weekly basis (at day 0, 7, 14, 21, 28 and 35) using flow morphometry

(see above). The samples were prepared and measured identical as shown in section 2.3. In this way, a heterogeneous set of ~12,000 RBC micrographs was generated. After being manually sorted into nine predetermined morphology classes, they were used for the training process. Figure 22 shows examples of micrographs from each class. To increase the heterogeneity of the image data, we used image augmentation (LeCun, 1998). This form of data augmentation incorporates geometrical image transformations such as reflection, rotation, shear, and translation (see Figure 15).

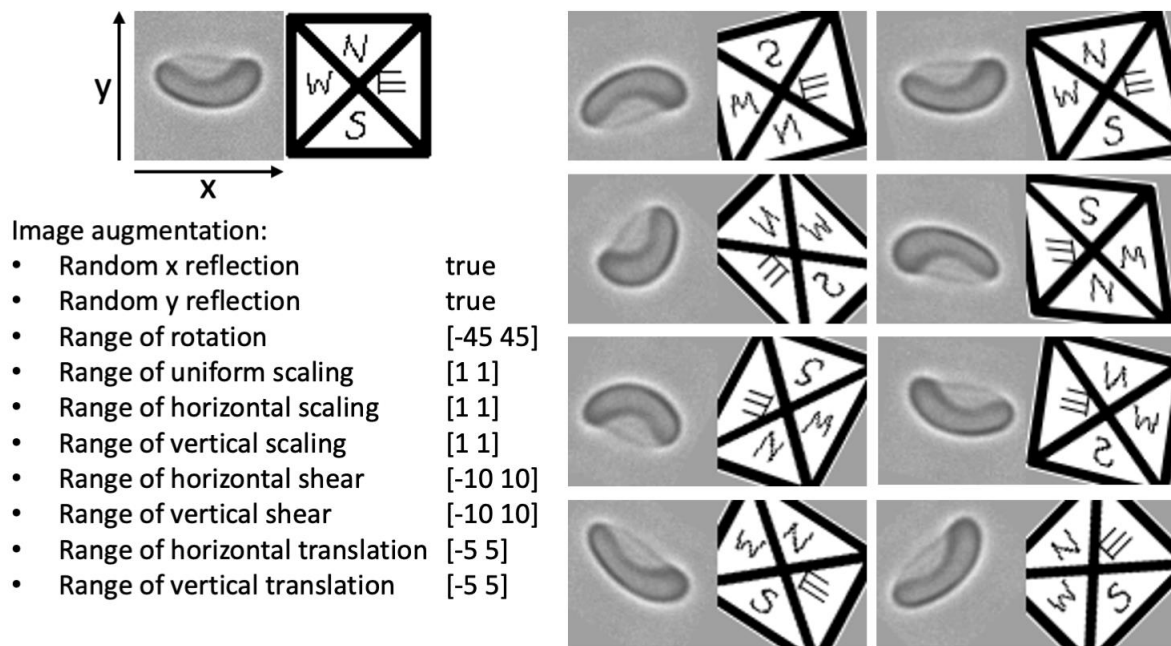


**Figure 15. Image augmentation.** Top left: Original image (stomatocyte) with respective reference image. Bottom left: Image augmentation settings. The two values in the square brackets indicate the range of possible augmentation. Range of uniform scaling [1 1], for example, indicates that no uniform scaling took place because the values are the same. Right side: 8 augmented sample images together with the respective reference image.

Augmentation enhances the robustness of the network classification regarding intraclass variances (Shorten & Khoshgoftaar, 2019). In addition, it helps to prevent the network from overfitting (Paris et al., 2004). Overfitting results in a network that cannot generalize well from training data to new unseen data. To further reduce the risk of overfitting, the image data were randomly divided into three parts: the training set (65%), the validation set (20%), and the test set (15%). The training set is used to teach the CNN the characteristics of the morphology classes by adjusting the kernels, weights and bias terms. Throughout this training process, the validation set is used repeatedly to monitor the training progress and avoid overfitting. Finally, the test set is

applied to assess the final classification accuracy of the trained CNN. Through this process, a confusion matrix is created so that precision, sensitivity, and F<sub>1</sub>-scores can be calculated (Sokolova et al., 2006).

Certain training options must be chosen to determine the rules according to which the CNN is trained. We chose the cross entropy (Bishop & Nasrabadi, 2006) as the loss function for the optimization of the CNN. The cross entropy is obtained by MATLAB as follows:

$$loss = \sum_{i=1}^n \sum_{j=1}^l t_{ij} \ln y_{ij}$$

where

n = number of samples,

l = number of classes,

t = indicator to which class the sample belongs, and

y = predicted value of the sample to its class.

The goal of the CNN is to minimize the training loss. The CNN achieves this by using the known training loss information and adjusting the values of the weights, starting with the output layer weights and ending with the input layer weights. The search for the global minimum of the cross entropy is conducted by an adaptive momentum estimation algorithm (Kingma & Ba, 2015), with a step-width of 0.0001. The process by which the CNN independently optimizes its own weights to enhance the responses and accuracy of the results is referred to as backpropagation (Ash, 1989; LeCun, 1989). One forward calculation in addition to one backpropagation is a pass. To achieve faster convergence, the training data was divided into mini-batches, each of which contains 32 cell micrographs (Hastie et al., 2009; Kubat & Kubat, 2017). These 32 images are analyzed simultaneously by the CNN, which adjusts its weights in parallel instead of analyzing each image sequentially. Furthermore, based on our validation set, we selected intermediate batches of 50 mini-batches each to generate intermediate validations and thereby reduce the risk of random fluctuations during training (Kihm et al., 2018). A complete pass of the training data is referred to as an epoch. A total number of ten epochs were chosen because this number ensured good training without overfitting.

### 2.2.7 Alternative CNN Architecture

This work is mainly based on the CNN architecture of GoogLeNet. However, of note before using GoogLeNet, we tested two other CNN architectures as well, namely AlexNet (Krizhevsky et al., 2012) and ResNet50 (He et al., 2016). On the one hand, AlexNet was sorted out relatively quickly after the first tests, as the classification accuracy was somewhat weaker than that of the other two networks. On the other hand, ResNet50 was the strongest CNN for RBC classification over a long period of time according to this study, since the networks were exclusively used to classify RBC morphologies measured in the rolling mode motion (this process is explained in detail in 3.2.1). Therefore, the architecture of ResNet50 will be elucidated in more detail in what follows.

ResNet50 is a deep network with 50 layers and 25.6 million weights. For orientation, GoogLeNet has 22 layers and only 7 million weights. ResNet50 is thus considerably “deeper”, and consequently one might expect it to provide a better performance (He et al., 2016). The main building blocks of ResNet50 are based on residual learning (see Figure 16) which allows for a deeper network structure without generating a usually observed degradation problem. Degradation (of the training accuracy) in this case means, that as the network’s depth increases, its accuracy becomes saturated and then degrades rapidly (He et al., 2016).

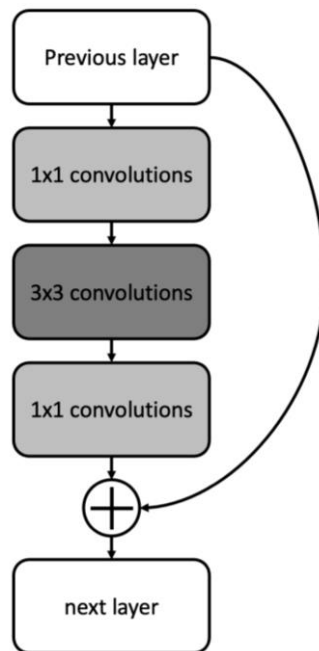


**Figure 16. Residual building block of ResNet50.** ResNet50's main architecture consists of 16 residual building blocks arranged in a consecutive way.

Each residual building block consist of three convolutional layers. The convolutional layers always contain the following convolutional kernels in the same arrangement: 1x1, 3x3 and 1x1. While the outputs of the previous layer are processed by the convolutional layers, an identity mapping layer is used to bypass the outputs simultaneously. The identity mapping layer creates a residual mapping of the outputs by skipping them forward. The skipped outputs and the processed outputs are then calculated elementwise. This structure is called a residual block, which greatly reduces the problem of degradation during training with deeper networks.

We trained this network accordingly to GoogLeNet. A small difference in training was the imposition of a lower maximal number of epochs, i.e., six instead of ten. The decision between the different CNN architectures is explained in detail in section 3.2.1.

### 2.3 RBC Sample Preparation and Morphology Classes

All RCCs we used in this work were produced by the German Red Cross Blood Donor Service in Mannheim by venipuncture from healthy adult donors aged 19 to 59. The donors gave informed consent that their blood may be used for research purposes or

quality control to enhance the safety of hemotherapy. The Ethics Committee of the University Medical Centre Mannheim (UMM) confirmed that no special ethical vote was required for conducting this work. The extracted blood (500 mL  $\pm$  10%) was collected into 70 mL of anticoagulant citrate phosphate dextrose (CPD). Through centrifugation (15 min, 3500 rpm) whole blood components were separated followed by a leucofiltration of RBCs. The RBCs were added to 110 mL of saline adenine glucose mannitol (SAG-M, 376 mOsm/L) using an automated blood separator (Compomat G4, Fresenius Kabi Deutschland GmbH, Germany) and prior to final storage at 4 °C. Samples were taken from 5 RCCs at week 2, 5, 6, 8, 10 and 12 to show more advanced morphological changes upon storage lesion. The currently accepted shelf-life of RCCs in SAG-M in Germany is 6 weeks. Before sampling, RCCs were rotated for 20 min at a speed of 0.1 rps (ACR Rotator, Lmb Technologie GmbH, Schwaig, Germany). These generated data represent dataset B.

To compute the level of hemolysis, hemoglobin (Hb) and hematocrit (Hkt) levels were measured from a 4 mL aliquot by means of a hematology analyzer (CELLDYN Ruby, Abbott GmbH & Co. KG, Wiesbaden, Germany). For the measurement of free hemoglobin (fHb), 2 mL aliquots were centrifuged at 4,000 rpm for 10 min (Rotina 38, Hettich GmbH & Co. KG, Tuttlingen, Germany). 50  $\mu$ L of the supernatant was diluted in 500  $\mu$ L buffer solution (fHb, Bioanalytic GmbH, Freiburg, Germany) and analyzed photometrically (DR 5000, Hach Lange GmbH, Düsseldorf, Germany). Hemolysis levels were then computed as follows:

$$\text{hemolysis}(\%) = \frac{(100 - \text{Hkt}[\text{l/l}] \cdot 100[\%]) \cdot \text{fHb}[\text{g/l}]}{\text{Hb}[\text{g/dl}] \cdot 10}$$

Aliquots were prepared for the microfluidic system as follows: 1.5  $\mu$ L samples were extracted from the agitated RCCs and then diluted 1:1000 in 0.9% NaCl. Triplicate measurements were carried out with an approximate intra-donor uncertainty of 3% out of absolute values with 90% confidence (as calculated based on experiments with three technical replicates; see (Boecker, 2018)). In addition to the measured concentration values of the individual morphology classes, we computed a morphological index (MI) as a weighted sum of the concentration values (Usry et al., 1975). As a single value, the MI provides a morphological scale for the quality of RCCs. RBC morphology classes corresponding to a higher quality receive weights close to 1. Accordingly, RBC morphology classes associated with lower quality receive weights close to 0. Therefore, an MI with a value close to 1 represents a RCC which is mainly

composed of RBCs with high quality associated morphologies. We changed the weights for the different morphologies slightly in comparison to the definition of the MI in (Usry et al., 1975). This was carried out in accordance with the morphological classification presented in this study: a weight of 1 was assigned to the concentration of discocytes (D), trilobes (T), deformed stomatocytes (DS) and stomatocytes (ST). A weight of 0.8 was assigned to echinocytes1 (E1), a weight of 0.6 to echinocytes2 (E2), a weight of 0.4 to echinocytes3 (E3), and a weight of 0.2 to the spherical forms of spherocytocytes (SE) and spherocytes (SP). Typical examples of each of these morphologies are shown in Figure 22.

## 2.4 Statistics

We evaluated the classification accuracy of the trained CNN by using a confusion matrix (CM) generated from the test data (see section 2.2.6) in MATLAB. The CM is used to compare the classification of individual RBC micrographs by the CNN with a manual reference classification (Stehman, 1997). In this way, each row in the CM represents the true class (manual classification) and each column represents the predicted class (CNN classification) (Powers, 2011). As an indicator of the performance of the network, an overall accuracy can be derived from the CM. The overall accuracy is defined as a quotient of the correctly classified RBCs and total analyzed RBCs. For a more detailed analysis, the following three commonly used indicators were calculated (Sokolova et al., 2006):

$$Precision = \frac{TP}{(TP + FP)}$$

$$Sensitivity = \frac{TP}{(TP + FN)}$$

$$F_1 - score = \frac{2 * TP}{(2 * TP + FP + FN)}$$

The abbreviations TP, FP, and FN stand for true positive, false positive, and false negative RBCs, respectively. These statistical measures give more information about the performance of the CNN from different points of view. The precision (positive predictive value) can be seen as a measure of the exactness of the CNN. It denotes which fraction of the prediction as a positive class were actually positive. The sensitivity

(true positive rate), also known as the recall or hit rate, is a measure of the selectivity of the CNN. The sensitivity measures the proportion of positives that are correctly identified. The  $F_1$ -score is defined as the harmonic mean of precision and sensitivity and thus represents a class-specific quality indicator of the trained CNN.

We carried out further statistical analysis using GraphPad Prism 9.3.1 (GraphPad Software, San Diego, California, USA). Data representing multiple measurements are presented as mean values with all measurement data points or the 95% confidence intervals as error bars. This was done to show general trends of the data and at the same time represent the inter donor variance between different RBC samples. Inter donor variance here means that RBC samples from different donors may react differently to storage conditions and can thus generate greater variations in the measurement data. Simple linear regression was used to compute the correlation of morphological proportions and hemolysis level. The linear regression coefficient was applied as a measurement for goodness of fit.

## 2.5 Flow Morphometry applied to Air Rescue RCCs

### 2.5.1 Storage and Transport Logistics

In order to provide patients suffering from life-threatening hemorrhage with blood components at an early stage, we established and validated a system that ensures the storage and transport of RCCs to the flight center (DRF Luftrettung GmbH) and then back to the blood bank of the Mannheim Institute of the German Red Cross Blood Services (blood bank) on a daily and routine basis. Due to regulatory requirements, a rotation system was implemented in which both RCCs and lyoplasma were transported every third day (Figure 18). Each day, two RCCs were packed with two lyoplasma units, 3 bedside tests, and a temperature data logger (ThermoScan Datenlogger™, TRANSMED, Nürnberg, Germany) in a passively cooled Pelican Crēdo ProMed™ 4l transport container (PELI Biothermal™, Plymouth, MN - USA) (Figure 17). These transport containers were validated by the manufacturer with ISTA7D profiles (a development test which evaluated the effects of external temperature exposures of individual packaged-products), in order to keep the RCCs at a regulatory compliant

temperature for up to 96 hours at outside temperatures of 30 °C. Prior to adding the blood products, the Crēdo box was provided with coolants filled with a phase change compound and vacuum insulated panels in order to ensure a temperature range of +2 °C to +6 °C (DAY 1).

### Crēdo ProMed™ Packing

1. Pre-cool 6 Crēdo ProMed™ coolants > 24 at -18°C.
2. Remove coolants and store for 35 min at RT, dry if necessary.
3. Pack the box with coolants as instructed.
4. Add 2 Lyoplasma flasks, 2 RCCs, 3 Bedside tests and a data logger.
5. Label the box as required.

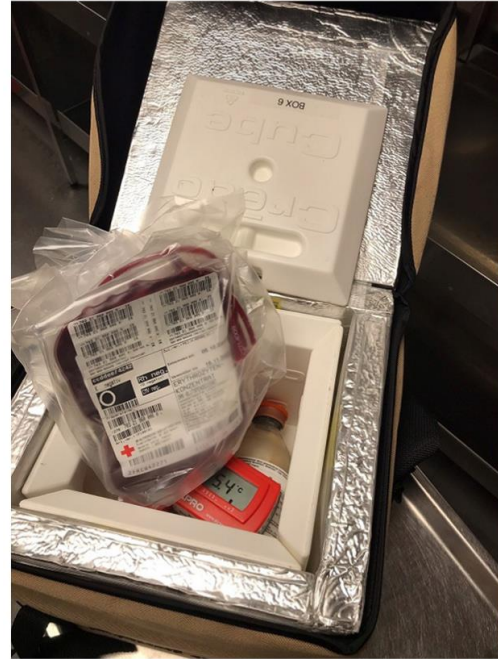


**Figure 17. Credo Crēdo ProMed™ carry bag packing.** The cooling bags were packed in compliance with a SOP. The photo shows a packed carry bag equipped with two RCCs, two lyoplasma units, three bedside tests and a temperature data logger. Prior to adding the blood products, the Credo box was packed with coolants containing phase changing material and vacuum insulated plates. Adapted from (Boecker et al., 2022).

The cool box was carried to the DRF station and taken along on each mission of the DRF rescue helicopter (helicopter Airbus EC 135, Christoph 53 of the DRF Stiftung Luftrettung, base Mannheim). At the end of the deployment day, the products were returned from the DRF station to the blood bank for exchange with the next products which were already packed in a Crēdo box (DAY 2). After return, the products were subjected to an initial visual inspection and their temperature was documented. The permissible transport temperature range is defined by a range from +2°C to +10°C. However, regulatory specifications require adherence to storage conditions defined by a range from +2°C to +6°C, as the RCCs were transported atypical often (Guideline Hemotherapy German Medical Association (Bundesärztekammer, 2020)). After one day of quarantine storage, the defined release criteria were checked by means of visual inspection, compliance with the temperature range and shelf life (DAY 3). Upon

demonstration of compliance, the products were returned to the rotation cycle. This procedure was repeated until the emergency use of the blood components or the end of the shelf life of the RCCs. Control samples were packed and unpacked in the same manner as the flight samples. Yet, instead of being transported to the DRF station, the control samples were stored in Crêdo transport containers kept at room temperature (RT) within the blood bank for the same period of time as the flight samples were kept in their transport containers.

The helicopter's operating hours were from sunrise (7 a.m. at the earliest) to sunset. The RCCs were loaded onto the helicopter during operating hours and carried on regular missions. Outside the helicopter's operating hours, the RCCs were delivered to the blood bank and stored in a temperature-controlled way in the cold room at +2 °C to +6 °C. In terms of flight altitude, the minimum safety altitude over obstacle scenery is 150 m and 300 m over densely populated areas. These limits can be undercut in the air rescue service. As a rule of thumb, the flight altitude was around 300 m. Flight times were recorded for each RCC and the total flight time duration was calculated at the end of the shelf life.

### 2.5.2 Rotation System and Sampling

In this study, we used rhesus D-negative RCCs of blood group 0 in the flight group, which can be given to any recipient. In comparison, the RCCs in the control group consisted mainly of rhesus D-positive RCCs of blood group AB. The difference in the blood group existed only because rhesus D-negative RCCs of blood group 0 are too rare and too valuable to be used as a control samples. We expect that the blood group has no influence on the quality of RCCs after repeated transport with a helicopter.

We collected end-point samples from both control and flight RCCs (a) when the RCCs reached the end of their shelf life or (b) after transfusion or (c) after they failed compliance testing based on visual inspection or temperature range (see Figure 18). Initial samples were taken only from some units, but initial sampling was not possible for all samples due to technical difficulties. Prior to sampling, the units were rotated for 20 minutes at 0.1 rpm (ACR Rotator, Lmb Technologie GmbH, Schwaig, Germany). Sampling from RCCs used in routine is critical: Once samples are extracted with a

syringe, the unit must be used immediately or discarded. In order to circumvent the critical extraction by syringe, we used two different sampling methods. Sampling was performed either by using the cross-matching segments attached to the RCCs or by directly withdrawing blood from the RCCs with a syringe. For the initial samples the cross-matching segment method was used in the majority of cases. Direct withdrawing of blood from the RCCs with a syringe was not possible for the initial sampling. In a few cases of initial samples, pilot tubes were attached to the RCCs that could be used for sampling. These pilot tubes were only available for RCCs without additional tubing which were already segmented for cross-matching purposes. The pilot tubes were filled with fresh blood from the RCCs before they were removed from them. In this way a direct withdrawal of blood with a syringe could be imitated for initial sampling.

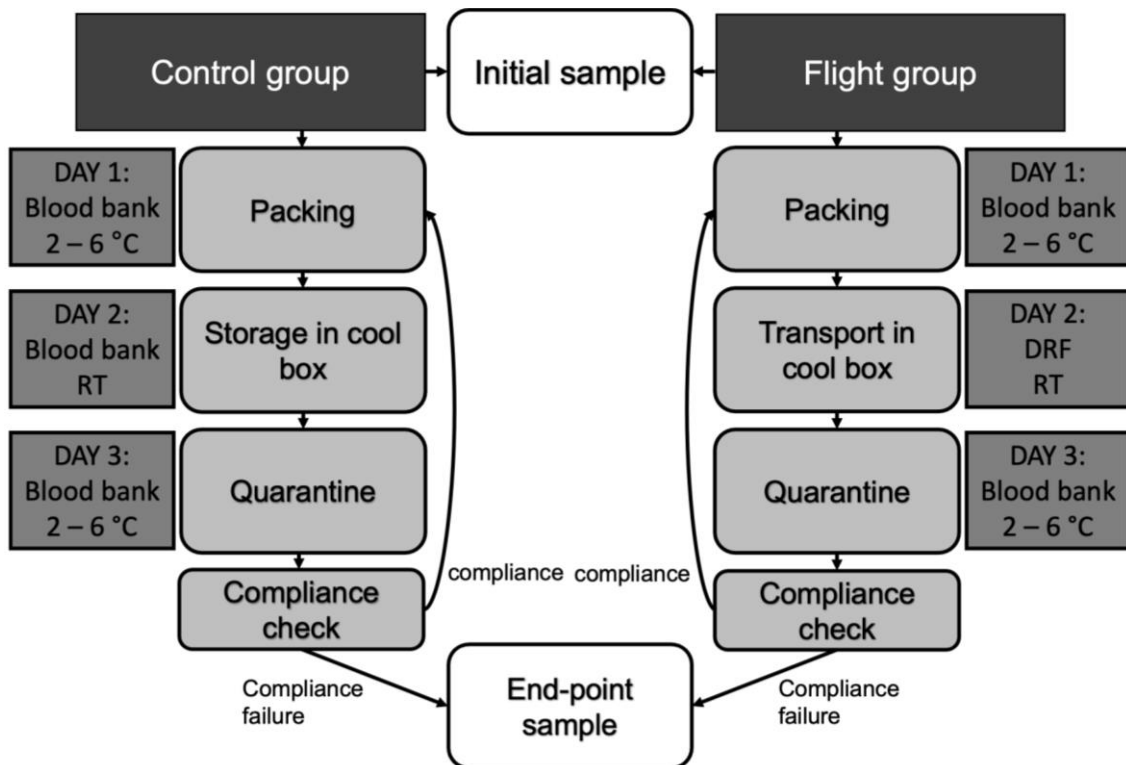


**Figure 18. Flow chart of the rotation system for RCC logistics.** White boxes denote sampling. Dark gray background denotes timing, location and temperature, whereas light gray background indicates the steps in the rotation cycle. Adapted from (Boecker et al., 2022)

### 2.5.3 Biochemical and Morphological Quality Control

We analyzed the end-point samples (flight and control groups) for hemoglobin (Hb), free hemoglobin (fHb), hematocrit (Hkt), hemolysis, mean corpuscular volume (MCV), potassium and pH.

Hb, fHb, Hkt and hemolysis were measured as described in section 2.3. In addition to Hb and Hkt, the MCV was measured from the same 4 mL aliquot using the hematology analyzer (CELLDYN Ruby, Abbott GmbH & Co. KG, Wiesbaden, Germany). Potassium levels and pH values were measured with a blood gas analyzer (ABL 80 Flex, Radiometer GmbH, Krefeld, Germany).

For flow morphometry measurement in the helicopter study, we diluted a 100  $\mu$ L sample 1:400 in 0.9% NaCl. The dilution is required to avoid overlapping of cells during the image capturing step. The diluted erythrocytes were given time to adjust to the medium and to stabilize their shapes for 10 minutes. Thereafter, the suspension was filled into the input reservoir syringe and it was moved into the flow chamber by manual operation of the syringe pump. This initial non-stationary flow causes a brief elevated shear stress and this generate reversible shear induces changes in the cell morphology. Therefore, the image capture was started after a delay of 20 seconds, allowing for morphological relaxation during stable and regular flow and controlled by the syringe pump. From each sample, we acquired about 3000 microscopic images of erythrocytes in the moving suspension. The focal plane was adjusted at a height of 12  $\mu$ m to facilitate differentiation among morphological classes by exploiting the rolling mode feature. After the image capturing, the images were analyzed to detect the sharply imaged cells and to generate individual cell-portraits for further analysis and classification by CNN.

We analyzed both the flight and the control samples in their final stage by end-point measurements to obtain their biochemical and morphological parameters. Only for morphology parameters were the net changes determined by measuring initial and end-point samples. In this case, the initial concentration values of specific morphologies were subtracted from the final values of the end-point measurements, resulting in difference measurements. Difference measurements are advantageous since they avoid the inter-donor dispersion displayed by the measurement of absolute parameters.

#### 2.5.4 Statistics for Air Rescue RCCs

We performed the statistical analysis with the statistical tool GraphPad Prism 9.3.1. Data are presented as scatter plots with the mean value and the 95% confidence interval (CI95%). Flight and control groups were compared by applying the unpaired two-tailed Mann-Whitney U tests. A p-value of 0.05 was considered statistically significant ( $\alpha = 0.05$ ). Potential effect sizes of flight are presented as Hodges-Lehmann estimates (medians of the calculated difference between each value in the flight group and each value in the control group) with 95% confidence intervals. The statistical analysis of the helicopter samples is exceptional based on 95% confidence intervals as error bars.

We used linear regression to compute the correlation between RBC quality parameters and flight time duration. As a measurement of goodness of fit, the linear regression coefficient was used in combination with the p-value to ascertain the obtained slope's difference to zero.

### 3 RESULTS

#### 3.1 Improvements of the Flow Morphometry Setup

We made two modifications to the original flow morphometry setup developed by Sierra (Sierra, 2017). Firstly, the mounting for the flow chamber was stiffened. This was achieved by installing two additional cross bracings to the flow chamber mounting device.

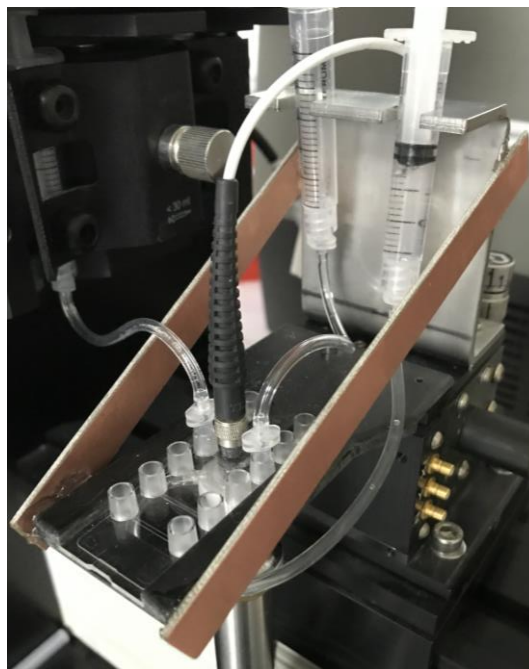


**Figure 19. Stiffening of flow chamber mounting device.** The two copper-colored cross bracings increased the stiffness of the flow chamber mounting device. They are attached to the mounting device by a strong glue.

Previously, when changing samples in the system, the changing forces on the sample reservoir were partly transduced to the mount of the flow chamber via the connection silicon tubing. This coupling caused slight variations in the position of the focal plane within the flow chamber. As a result, the focal plane height had to be readjusted. A quick readjustment, however, led to inaccurate measurements due to a one-sided hysteresis in the millimeter adjustment screws. Therefore, the position of the bottom of the flow chamber always had to be set beforehand by sedimented cells. From this position the desired setting of the position  $h$  in the flow chamber could be reset by adjusting the millimeter screws in one direction to avoid the one-sided hysteresis. By

stiffening the mounting of the flow chamber, we could resolve these focal plane height variations, eliminating the need for readjustment after an experiment has started.

Secondly, we replaced the objective cover cap for the water immersion by applying ultrasonic gel manually on the objective with a syringe equipped injection nozzle.

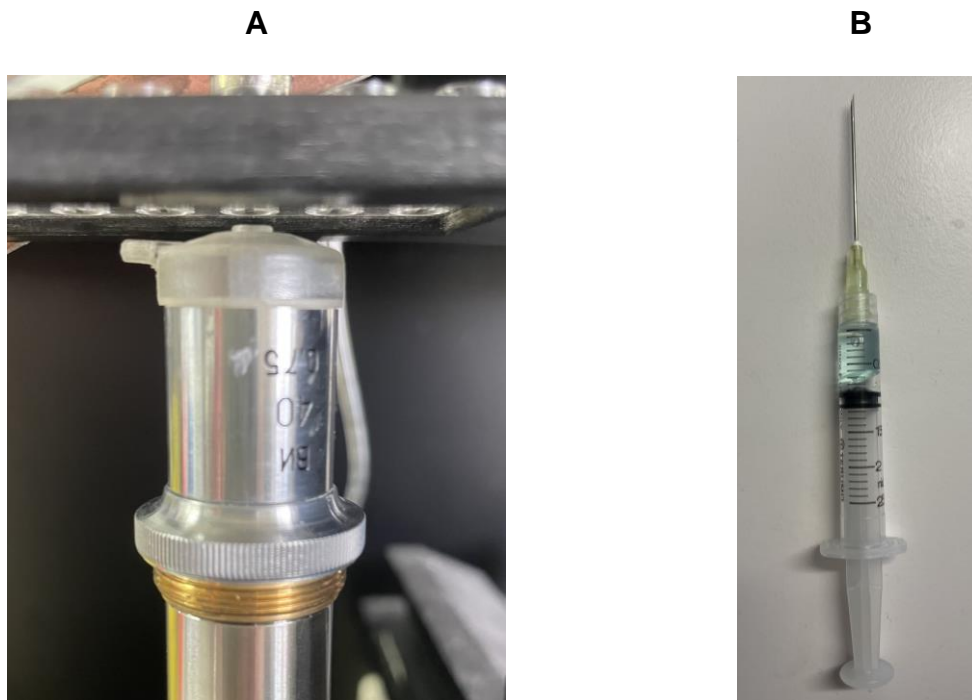


**Figure 20. Old and new immersion fluid system.** The objective cover cap (A) for the water immersion of the objective. The ultrasonic gel filled syringe with mounted injection nozzle for the ultrasonic immersion (B).

The ultrasonic gel has the advantage of being more durable than water against condensation, which keeps the optical properties constant when a measurement series takes several hours. The refractive index of ultrasound gel is almost identical to that of water, which is required to achieve the intended immersion objective.

## 3.2 Convolutional Neural Network Based Image Processing

### 3.2.1 CNN Architecture and Development of RBC Morphology Class Composition

The main focus of this study was to develop a CNN that performs outstandingly in classifying degradation-induced and shear-induced RBC morphologies. The most significant differentiation between RBC morphologies is given at a focal plane height of 12  $\mu\text{m}$  where healthy discocytes move predominantly in the rolling mode and thus offer an additional feature for their discrimination.

**CNN for oriented RBC micrographs.** For this specific classification task of RBC micrographs generated at 12  $\mu\text{m}$  focal plane height, we trained three different CNN network architectures: AlexNet, GoogLeNet and ResNet50. From the beginning on AlexNet achieved lower classification accuracies and got sorted out relatively quickly. GoogLeNet and ResNet50 had somewhat same classification accuracies of 92% and 93%, respectively. Ultimately, the overall classification results were slightly better with the CNN architecture of ResNet50. However, it is important to mention that ResNet50 was only best suited for classifying RBC morphologies on the basis of a training that emphasized the rolling mode dominance in the discocyte and early stage echinocyte classes. As a result, the set of training images of these morphology classes mainly represented RBCs in the typical orientation of the rolling mode motion, i.e., as waisted ovals. In this case, the variation in the RBC orientation was small and so we kept the image augmentation limited to variations between the RBC-sizes to account for inter-donor variation. However, image rotation as a possible geometric augmentation was not adopted in order to keep the training as close as possible near the specific rolling mode orientation. Typical RBC morphologies for each class at 12  $\mu\text{m}$  focal plane height are shown in Figure 21.

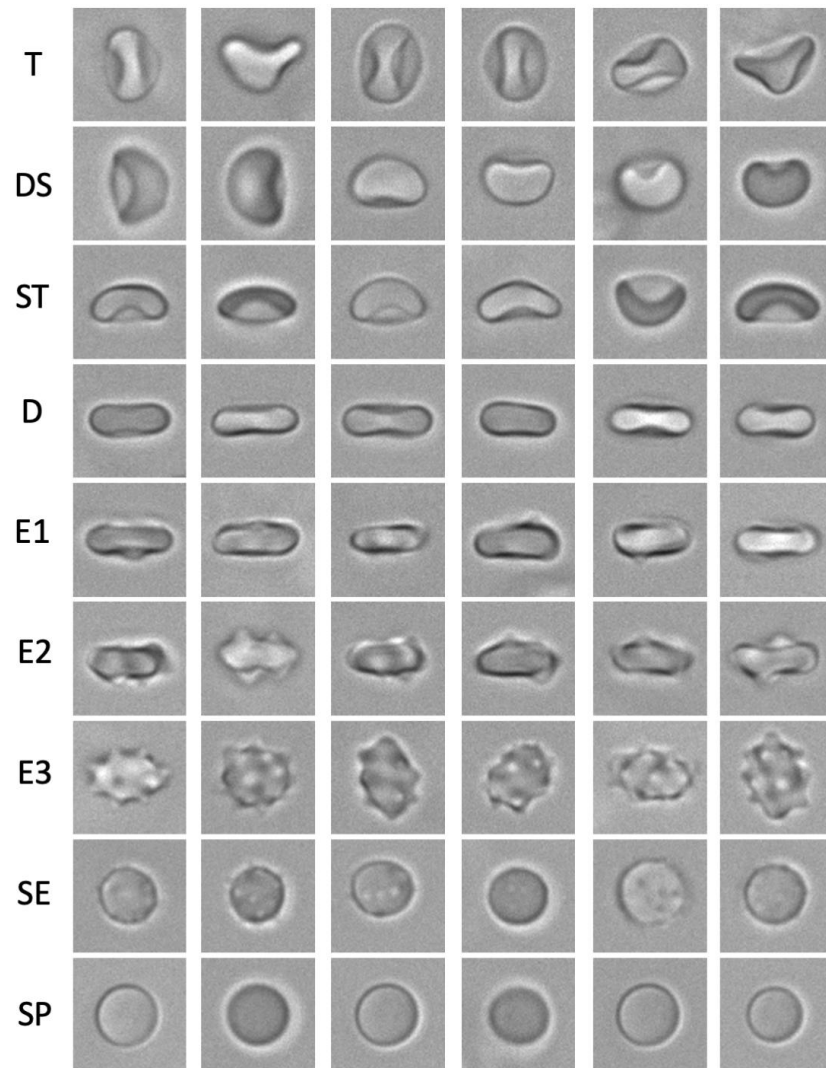


**Figure 21. Typical RBC morphologies of the different classes in training data for RBC classification at rolling mode position.** The six micrographs per RBC class show the small variations in RBC orientation in the training data. The following micrographs are shown for the classes: T (trilobe), DS (deformed stomatocyte), ST (stomatocyte), D (discocyte), E1 (echinocyte1), E2 (echinocyte2), E3 (echinocyte3), SE (spherocyte) and SP (spherocyte).

Based on this training, which emphasizes the rolling mode feature, ResNet50 was found to be best suited for classifying RBC morphologies. It achieved a high classification accuracy of 93%. Due to this results, the application of our CNN-based RBC classification on samples within a study of repeated air rescue mission transports of RCCs had been published on the basis of the ResNet50 network architecture (Boecker et al., 2022). This was done since all measurements of the study were carried out at a fixed focal plane height of 12  $\mu\text{m}$ .

**CNN for RBC micrographs without orientation.** However, we wanted to develop a CNN-based image classification that is not limited at analyzing image data of RBC micrographs acquired at 12  $\mu\text{m}$  focal plane height but that is flexible in the classification

of differently oriented RBC morphologies. For this reason, one objective of this study was to detect shear-induced morphologies at different heights of the flow channel. This is necessary to investigate to what extent the shear in our microfluidic system affects the transients between the different RBC morphology classes. Here the challenge was to classify RBCs correctly at positions in the flow channel where discocytes and early echinocyte stages do not roll but tumble and thus exhibit a variety of different orientations. Hence, the image data had to be analyzed with a CNN that does not rely on the rolling mode feature but is able to classify these RBC morphologies correctly in all orientations. Analyzing such an experiment with the ResNet50, if trained as described above, would lead to impaired sensitivity for the majority of discocytes and early echinocytes stages with random orientation. The ResNet50 could only detect and classify those RBC morphologies correctly that show an orientation as in Figure 21. In order to represent all possible orientations in the training, we included additional RBC micrographs which had been captured at different heights in the flow chamber with no rolling mode. In addition, we therefore expanded the augmentation of our data to include rotational variations of captured cell images.

Measuring at different heights in the flow chamber also results in a slightly different imaging contrast of the RBCs. The display of the lower contrast RBCs results from the fact that the contrast in the projected sample volume of the image decreases when the focal plane height position is increased in the flow chamber. At this higher focal plane position the contrast of the image is attenuated by a thicker layer of the RBC suspension.

As a result, the final training included RBC micrographs of discocytes and early echinocyte stages in all possible orientations and with a different contrast which represented a decreased imaging contrast at deeper channel positions. Examples of training images for the various RBC orientations in the RBC morphology classes are shown in Figure 22.

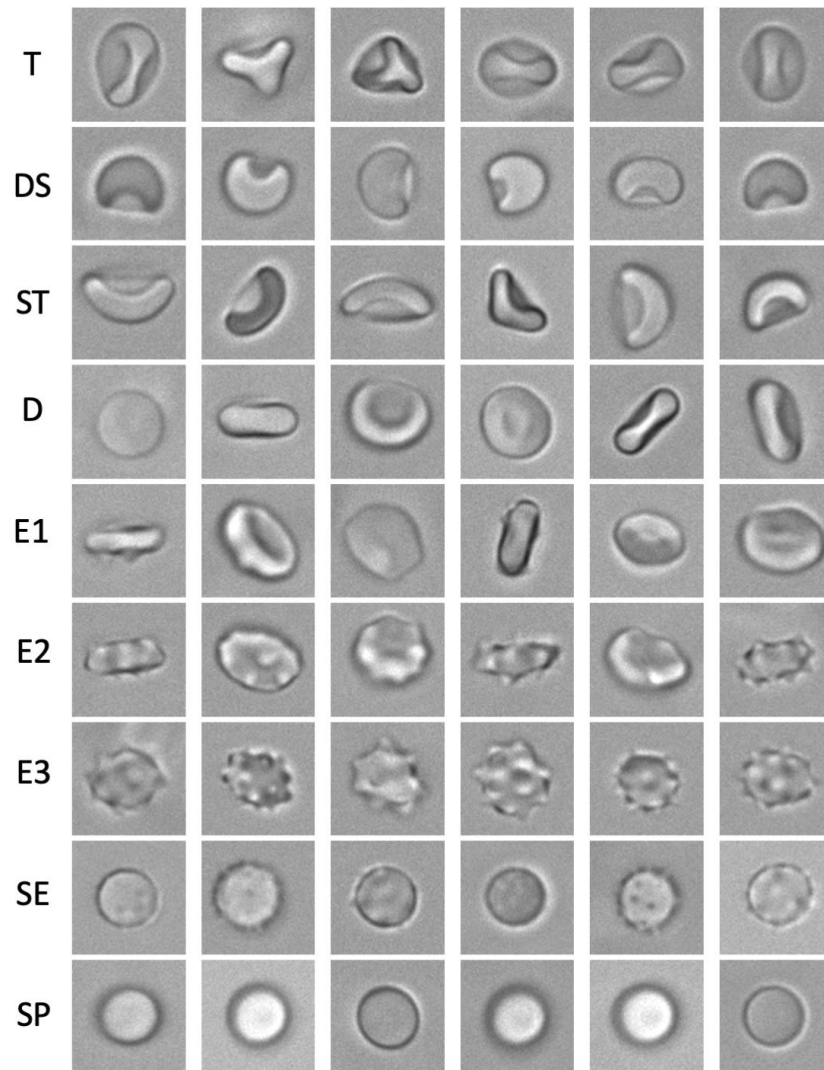


**Figure 22. Typical RBC morphologies of the different classes in training data for RBC classification that cover all RBC orientations in the different focal plane heights.** The six micrographs per RBC class show the large variations in RBC orientation in the training data. The following micrographs are shown for the classes: T (trilobe), DS (deformed stomatocyte), ST (stomatocyte), D (discocyte), E1 (echinocyte1), E2 (echinocyte2), E3 (echinocyte3), SE (spherocyte) and SP (spherocyte).

To differentiate correctly between spherocytes and flatly imaged discocytes it takes some effort. To accomplish this, we subdivided discocytes and spherocytes in two subclasses each, to ensure that very similar micrographs of both classes were still correctly classified. Through these extra classes, the CNN places additional emphasis on distinguishing these morphologies by treating them as separate morphology classes. These subclasses do not appear as separate classes in the RBC classification, but each contains cells as shown in Figure 23. These subclasses consist of slightly blurred cells but still provide enough information to be correctly classified. The flat discocytes are recognizable by the dark appearance of the (indented) center of the cell. Conversely, the spherocytes with the slightly blurred borders can be

recognized by their characteristic lack of such structures in the area of the center of the cells.



**Figure 23. Micrographs of discocytes and spherocytes subclasses to differentiate between the two RBC morphologies.** On the left, flat discocytes are recognizable by the dark center of the cell. On the right, spherocytes possess a slightly blurred border and light center of the cell.

When executing trainings under these conditions with both CNN architectures, ResNet50 and GoogLeNet, the CNN-based on the architecture of GoogLeNet had the higher classification accuracy in comparison to the ResNet50. The overall accuracies were 91% for ResNet50 and 92% for GoogLeNet. Therefore, we used the GoogLeNet based CNN that can classify RBC morphologies in all possible orientation shown in Figure 22 for all presented results in this thesis. This is important as the CNN can be used for all possible focal plane heights of our flow chamber with a good classification accuracy. The training progress of the GoogLeNet based CNN is described in detail in the following section.

### 3.2.2 CNN Training Progress of GoogLeNet

We carried out the CNN training using the manually pre-classified dataset A. The dataset was randomly split into three parts: the training set (65%), the validation set (20%), and the test set (15%). The training set was used to teach the CNN the characteristics of the different RBC morphology classes. The validation set was used to repeatedly monitor the training progress and to avoid overfitting. Finally, the test was used to assess the final classification accuracy of the trained CNN. During training, MATLAB provides a window that monitors the training progress of the network (Figure 24) by plotting various training parameters at every iteration of the training process. Each iteration is an estimate of the estimation algorithm that is used and updates the

network's parameters. Through the development of these parameters, it is possible to determine whether and how quickly the accuracy of the network is improving and whether the network tends towards an overfitting of the training data. The following training parameters are shown:

- **Training accuracy:** this parameter measures the classification accuracy of each individual mini-batch of the training dataset. The classification accuracy is calculated from the number of correctly classified RBC micrographs in the mini-batch and the total number of RBC micrographs in the mini-batch (here: 32 RBC micrographs).
- **Smoothed training accuracy:** this parameter measures the ratio of noisy training accuracy to unsmoothed accuracy in order to detect trends more easily. The smoothing is obtained by applying a smoothing algorithm to the training accuracy.
- **Validation accuracy:** this parameter measures the classification accuracy of the total validation set. The validation accuracy is obtained from the number of correctly classified RBC micrographs of the validation set and the total number of RBC micrographs of the validation set.
- **Training loss, smoothed training loss and validation loss:** this parameter measures the loss of each mini-batch, the smoothed version of it and the loss of the validation set, accordingly. The loss function used here is the cross-entropy loss, in which the loss function stands for the discrepancy between the predicted classification of an RBC micrograph and its expected classification.

During the training process, the weights of the CNN are adapted to optimally classify the RBC micrographs in the predetermined RBC morphology classes. The goal of the CNN in this process is to minimize the loss function, which is equivalent to classifying the RBCs in a way that is similar to the manual classification of the training data. The validation steps during the training are carried out to reduce the risk of overfitting the training data. To further reduce the risk of overfitting, the training is stopped if training accuracy/loss (blue and orange lines) starts to diverge from the validation accuracy/loss (black dotted lines). The training is also stopped when the maximum number of epochs is reached, or when the training accuracy meets a certain value (in this study this value was set to a training accuracy of 98%).

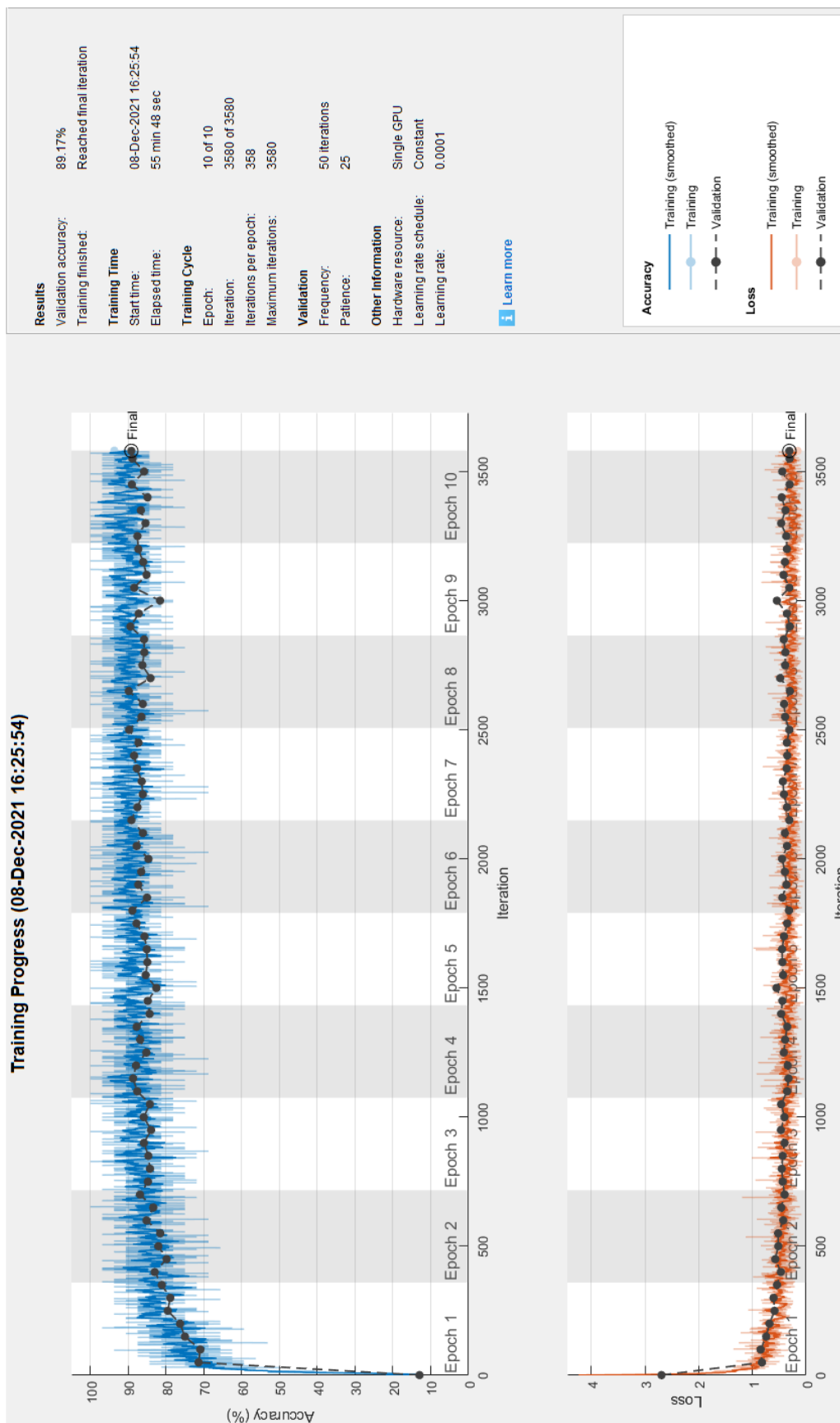


**Figure 24. CNN training process of GoogLeNet.** The training process of the CNN is represented by two plots, which respectively mark accuracy over iteration and loss over iteration. The training accuracy is depicted in light blue, its smoothed progress in blue and the validation steps in between are shown through black dots connected by a dashed black line. The training loss is depicted in the same way but with orange rather than blue colors. Additional information about the training results is shown in the upper right corner of the figure.

Each training epoch is highlighted by a shaded background. After the training is completed, the final score of validation accuracy is displayed and the reason for the training termination is given with further information on the training time and settings. For example, the training documented in Figure 24 was terminated because it reached the maximum epoch number of 10 epochs. The training could have been stopped earlier, as the training progress does not increase further after epoch 4. However, in this way it can be observed that there is no overfitting of the data. The training process of the CNN, which we used for the rest of this study, took 55 minutes and 48 seconds and resulted in a final validation accuracy of 89.17%.

### 3.2.3 High Resolution CNN Classification of Erythrocytes

The CNN, based on GoogLeNets architecture, successfully achieved a morphological resolution that corresponds to nine RBC classes (T, trilobe; ST, stomatocyte; DS, deformed stomatocyte; D, discocyte; E1, echinocyte 1; E2, echinocyte 2; E3, echinocyte 3; SE, spheroechinocyte; SP, spherocyte). Examples of micrographs for each class in different orientations are shown in Figure 25A. The sequence E1→E2→E3 of echinocyte morphologies indicate a gradual RBC degradation. However, it has to be kept in mind that these morphologies can reverse to a healthy disc-shaped morphology. The final stages of degradation are represented by the irreversible spherical morphologies SE and SP (Bessis, 1972; Hess, 2016; Longster et al., 1972). The stomatocyte morphologies ST and DS, as well as the trilobes (T), are essentially induced by shear stress (Bessis, 1972; Lanotte et al., 2016).

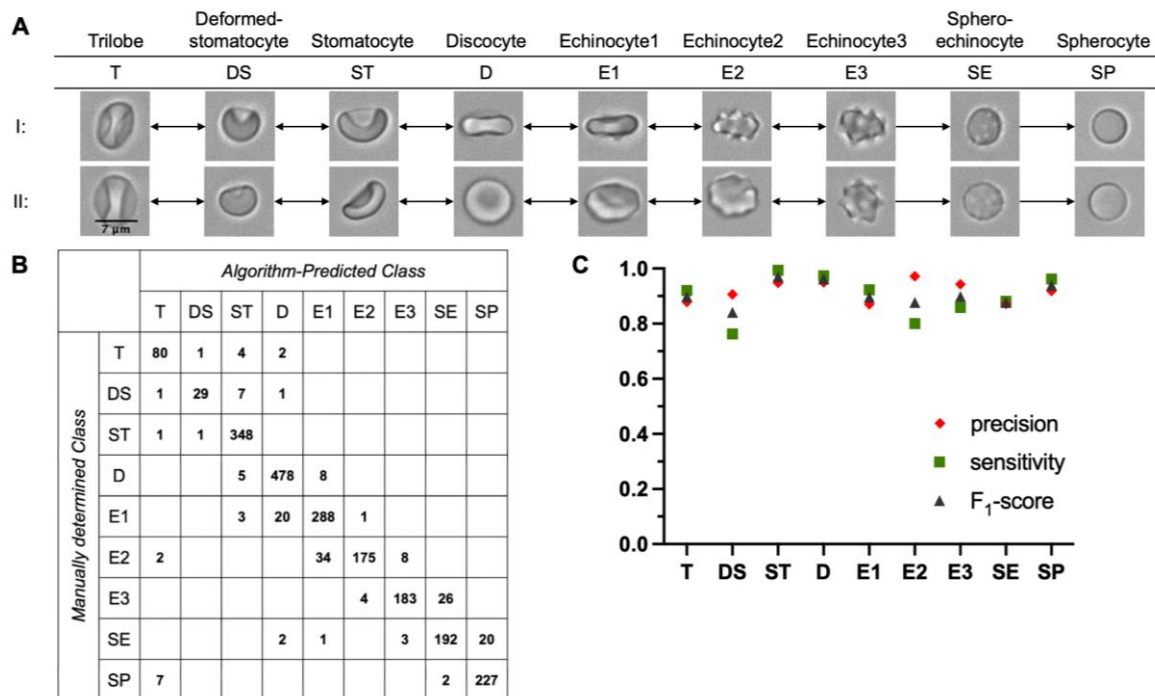


**Figure 25. RBC morphology classes and performance of CNN-based on GoogLeNet.** The CNN classifies erythrocytes according to the nine classes represented by the cell microscope images in (A): trilobe, deformed stomatocyte, stomatocyte, discocyte, echinocyte1, echinocyte2, echinocyte3, spheroechinocyte and spherocyte. The cell micrographs show typical morphologies at different positions in the flow channel (I = 12  $\mu$ m and II = 50  $\mu$ m above the channel bottom). The confusion matrix (CM) indicates the performance of the CNN regarding the classification of the test set, which had previously undergone manual classification (B). The precision, sensitivity, and F1 score for each morphology class are presented in (C). The test set was established from the dataset A = 12 RCCs.

In order to assess the classification accuracy of the trained CNN, we applied it to the test set of RBC micrographs (see 2.2.6). The results are presented in the form of a confusion matrix (CM) (see 2.4), which is shown in Figure 25B. From this CM, an overall accuracy of 92% was obtained as an indicator of the network's performance. For two reasons, the overall accuracy obtained from the test set is slightly higher than the validation accuracy (89%) which was obtained from the validation set. First, a class for bad cell shapes was not included in the definition of the overall accuracy of the test set. The test set has such a class, but it is used in order to preselect good RBC micrographs and therefore has nothing to do with the actual classification accuracy. This "bad class" is necessary to filter out disturbing morphologies from the sample. Otherwise, the CNN would classify them into one of the nine RBC morphology classes because it must assign a class to each input image (RBC micrograph). However, in the case of measuring validation accuracy, the bad class is integrated as an extra class, such that it generates further correctly and incorrectly classified RBC micrographs, which affects the accuracy of the CNNs. It is thus important to check if

micrographs of certain classes are incorrectly classified into the bad morphology class, as the CNN can also exaggerate when sorting out disturbing morphologies. Second, to obtain the validation accuracy and the classification accuracy two different sets of RBC micrographs are used (validation set and test set). The statistical variations among the different datasets generate statistical variances of all their statistical parameters including accuracy.

For a more detailed analysis of the CNN performance, we calculated the precision, sensitivity and  $F_1$ -score for each class of the trained CNN (see 2.4). The results of this are shown in Figure 25C. The  $F_1$ -scores represent class-specific quality indicators of the trained CNN. The  $F_1$ -scores for the nine classes were as follows: T = 89.9%, DS = 84.1%, ST = 97.1%, D = 96.2%, E1 = 89.6%, E2 = 87.7%, E3 = 89.9%, SE = 87.7% and SP = 94.0%. The lowest  $F_1$  score (84.1% for DS) is based on very few classification events (see numbers in CM of Figure 25B).

### 3.2.4 CNN Classes Match Reference Data from Decision Tree-Based Classification

In addition to its validation via a confusion matrix with a manual reference classification, we validated the trained CNN by comparing it to the previously used decision tree algorithm (Sierra et al., 2017). The comparison was performed by applying the CNN to the same set of image data that had previously been classified by Sierra et al. (Sierra et al., 2017) using the decision tree algorithm. The dataset B includes about 10 million RBC micrographs generated over a 12-week period (see Table 1), using flow morphometry as described in 2.3. The decision tree algorithm distinguished only three morphology classes: discocytes (D), echinocytes (E), and spherocytes (S). To compare these three classes with the CNN classification, we had to merge the nine CNN classes into three groups corresponding to the three classes of the binary decision tree. This pooling strategy was chosen according to the morphologies contained in the three classes of the decision tree. Stomatocyte morphologies as well as echinocyte 1 RBCs were classified as discocytes by the decision tree because they have a smooth cell surface compared to echinocytes 2, echinocytes 3 and spherocytes. Furthermore, their equivalent diameter exceeds the threshold that detects spherocytes in the decision tree algorithm. Trilobes were excluded completely from pooling as they were recognized by the decision tree as a disruptive kind of cell

morphology and sorted into the bad cell class. The pooling strategy with modified CM and the resulting precisions, sensitivities and  $F_1$ -scores are shown in Figure 26.

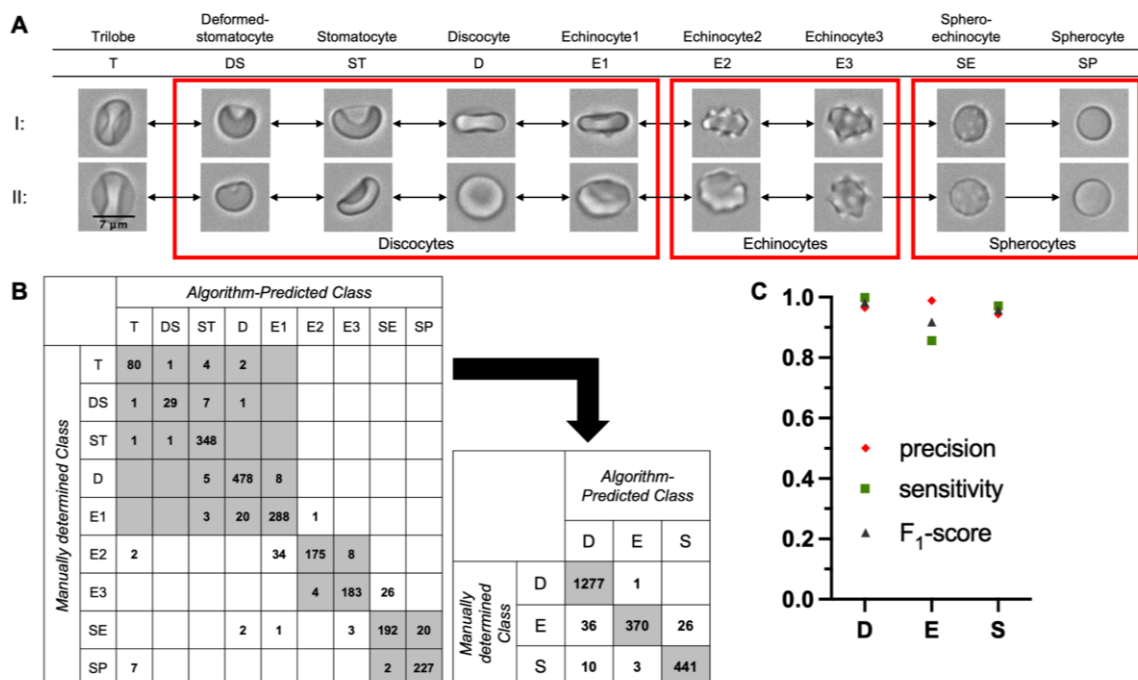


**Figure 26. Pooled RBC morphology classes and resulting CNN performance.** The CNN classifies erythrocytes according to the nine classes represented by the cell microscope images in (A): trilobe, deformed stomatocyte, stomatocyte, discocyte, echinocyte1, echinocyte2, echinocyte3 spheroechinocyte and spherocyte. The red boxes surrounding the cell micrographs show the pooling of the nine classes used for comparison with the classes reported in Sierra et al. (2017): Discocytes, Echinocytes, and Spherocytes. (B) The gray boxes in the original CM of the trained CNN with the nine RBC morphology classes show the CM with respect to the pooled classes. The resulting smaller CM depicts the calculated values for the pooled classes. The adapted precision, sensitivity and  $F_1$ -score for the pooled classes are shown in (C).

In comparison to the un-pooled CNN with nine RBC morphology classes and an overall accuracy of 92%, the classification accuracy of the pooled CNN is greater with an outcome of 96.5%. The obtained  $F_1$ -scores are, accordingly,  $D = 98.2\%$ ,  $E = 91.8\%$  and  $S = 95.8\%$ . We excluded trilobes from the pooling because the decision tree algorithm did not consider this shape as a classifiable morphology and categorized it in the bad cell category. The classification results of the pooled CNN and the decision tree are compared in Figure 27.

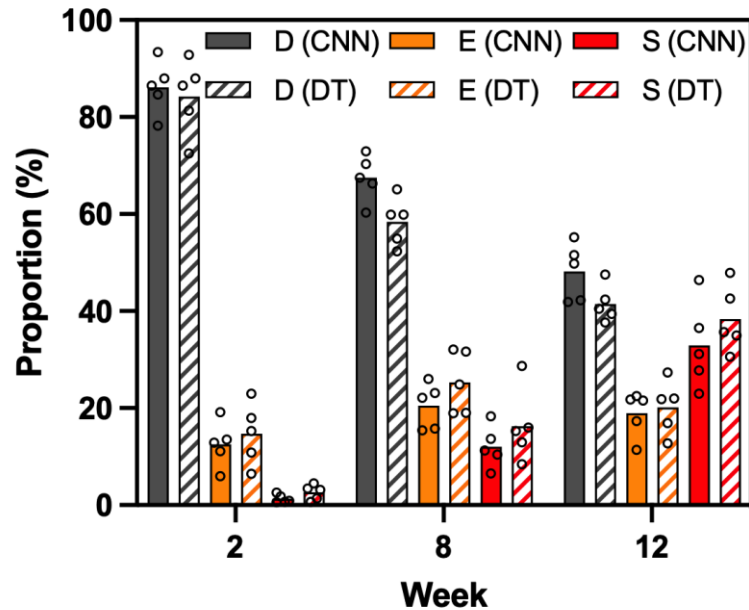


**Figure 27. Comparison of CNN classification and decision tree classification.** The solid-colored bars show the relative proportions of the three merged CNN classes discocytes (D) in grey, echinocytes (E) in orange and spherocytes (s) in red. The dashed comparison bars with the same colors show the corresponding proportions which are obtained by applying the decision tree (DT) algorithm to the same set of image data. Proportion values are means of five RCCs at the respective time points. Each data point is constituted by the measurement of three technical replicates. The results were obtained from dataset B,  $n = 5$  RCCs.

The pooled CNN classification agrees with the binary decision tree classification. Both classification systems reflect similar trends of aging: discocyte concentration gradually decreases, echinocyte concentration shows small changes but no clear trend, and spherocyte concentration increases over time. The CNN-based classification appears to show a small bias in favor of the pooled D class. However, considering the very different principles of CNN and decision tree, the mutual agreement between the two systems is excellent.

### 3.3 New Insights in Flow Morphometry of RBCs through High Resolution CNN Classification

#### 3.3.1 Shear Induced Stomatocyte Morphology in Flow Channels

Previously we described that, in the laminar flow channel used here, positions near the bottom and top surfaces are expected to have an accumulation of shear-induced artefactual stomatocyte morphologies. Such variances can be detected by adjusting the volume of the optical sample over the entire range of height positions  $h$  in the flow chamber and, accordingly, over a range of shear stress between 0 Pa and about 1 Pa.

In Figure 28, the concentration proportions of the morphology classes stomatocytes (ST), deformed stomatocytes (DS) and trilobes (T) are plotted as a function of the height position  $h$ . We defined stomatocytic morphology classes according to (Lanotte et al., 2016; Mauer et al., 2018; Reichel et al., 2019). These data were obtained from a single RCC at week 1 during storage.

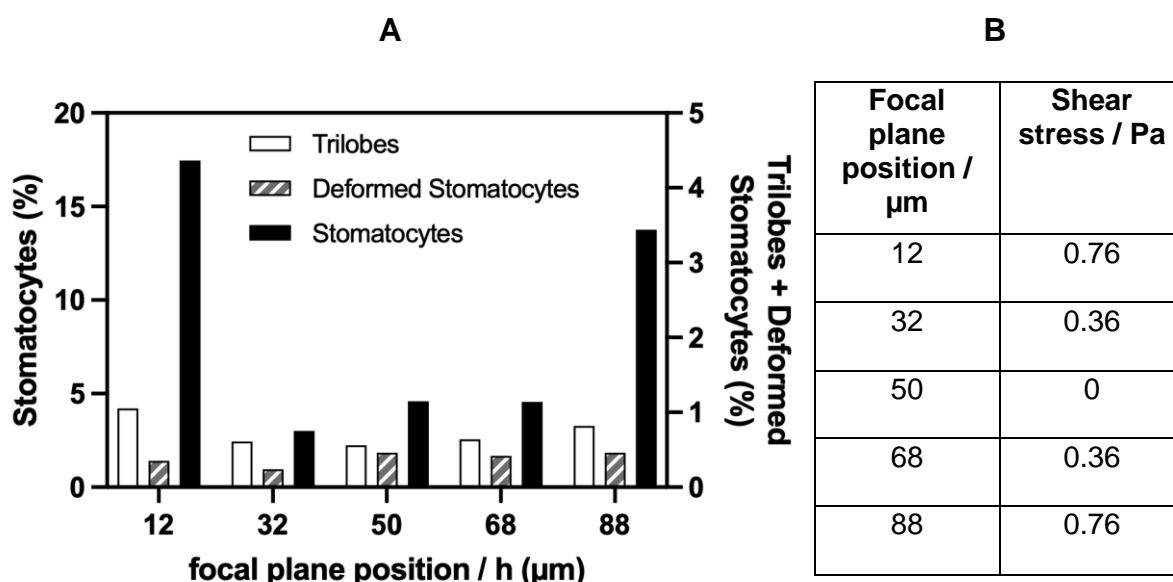


**Figure 28. Shear rate induced stomatocyte formation near the flow channel surfaces.** A: the concentrations of the RBC classes of a single RCC (stored for 1 week) are plotted as a function of position  $h$  in the flow channel.  $h$  represents the height of the focal plane in the channel above the bottom surface. The upper surface is at  $h = 100 \mu\text{m}$ . The measured morphology fractions are plotted as bars against the position of the focal plane height  $h$ . Through experiments with three technical replicates of RCCs, the intra donor uncertainty is approximately 3% of absolute values with 90% confidence. B: The respective shear rates are shown as a function of  $h$  in Pa.

The distribution of deformed stomatocytes (DS) and trilobes (T) as a function of height  $h$  within the flow channel reveal no clear trends. The corresponding proportions are small but non-zero at all positions and shear rates, which is consistent with previous findings (Lanotte et al., 2016; Piety et al., 2015). Since these concentrations show no clear dependence on the varying shear in the channel cross section, it can be assumed that they are not influenced by the shear rate but arise mainly from cell intrinsic degradation (Melzak et al., 2021) (see section 1.2).

In contrast to the behavior of the classes DS and T, the stomatocyte distribution (ST) reveals strong maxima near the chamber surfaces, where the shear rate is typically  $760 \text{ s}^{-1}$ , or a shear stress of 0.76 Pa. The local stomatocyte percentage at these two positions is about 15%, compared to only about 5% in the middle between the channel surfaces, where shear stress does not occur.

These data demonstrate the occurrence of shear-induced stomatocytes on each side of the center in the flow channel, even under moderate flow conditions such as the ones used here (see section 2.2.1). This transformation of the transient shear-induced morphology can only occur in flexible erythrocytes with intact membrane properties (Guo et al., 2014). Therefore, these cells should be considered as a subset of healthy erythrocytes that can reversibly alter from stomatocyte to discocyte morphology, a finding which agrees with (Lanotte et al., 2016; Mauer et al., 2018; Reichel et al., 2019).

### 3.3.2 RBC Morphology Progression during Storage Lesion and its Application for Storage Lesion Monitoring

With the CNN classification established and validated, we proceeded to use it to assess the storage lesion-associated morphological changes in stored RCCs. To determine class-specific trends during the aging of RBCs, the changing concentrations of all morphology classes were measured from a total of 5 RCCs (sample set B, see section 2.2.6) over a storage period of 12 weeks. The microscopic sample volume was specifically set to a height of  $12 \mu\text{m}$  above the channel bottom to facilitate the differentiation of discocytes from all other morphological classes, particularly spherocytes as a potential storage lesion marker, exploiting the rolling mode feature (see section 2.2.1 and (Sierra et al., 2017)). The general trends of all nine morphology classes throughout storage are shown in Figure 29.

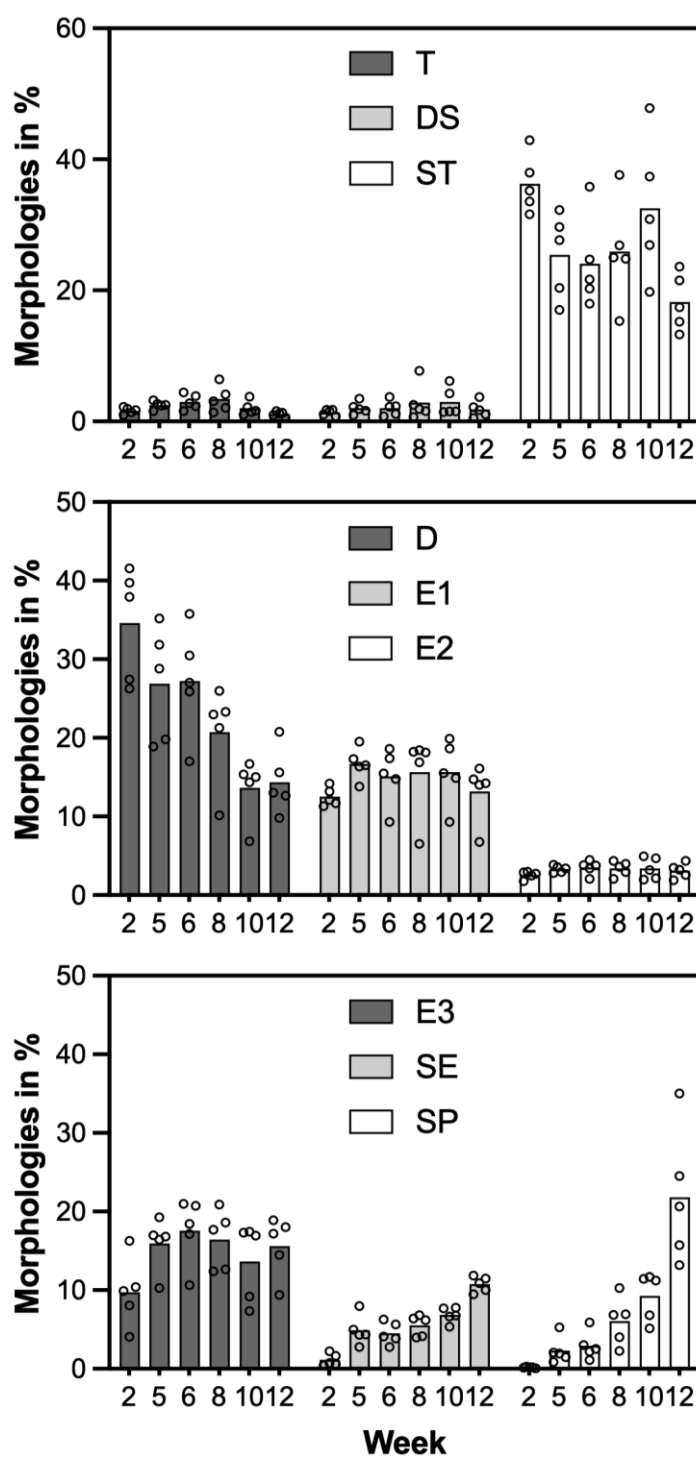


**Figure 29. RBC morphology transients during storage.** Measured class proportions are averaged over dataset B which consists of five RCCs and mean values are plotted as a function of time. Each data point is constituted by the measurement of three technical replicates. Abbreviations for morphologies are as follows: trilobe (T), deformed stomatocyte (DS), stomatocyte (ST), discocyte (D), echinocyte1 (E1), echinocyte2 (E2), echinocyte3 (E3), spherocyte (SE) and spherocyte (SP).

During storage, the concentration of discocytes (D) gradually decreases, although it is also subject to some random variations. These variations can be explained by the

bilayer-couple hypothesis (Sheetz & Singer, 1974), which describes the reversible transition from discocytes to other classes such as stomatocytes or echinocytes. Regardless of the reason for the apparently random variations in the D-signal, whether they are caused by reversible transition of discocytes or some other effect, the variations make the signal a potentially less suitable candidate for quality monitoring.

Concerning echinocytes (E1, E2, E3) and stomatocytes (T, DS, ST), these morphologies show only random variations and no distinct trend. Therefore, we decided not to incorporate them into the dataset for monitoring storage lesion; they would only generate signal noise.

In advanced stages of aging, erythrocytes adopt an irreversible spherical shape (Hess, 2016). For this reason, we expected the concentration of spherical morphologies (SE, SP) to increase monotonically over the storage time. As it turned out, the SE signal and the SP signal in Figure 29 increased continuously and monotonically over the entire time period. This implies that there are no reversible morphology changes which interfere with the SE and SP concentrations. We defined an index signal as a sum of SE and SP concentration with the same weighting (1.0) in order to use the information obtained from both signals simultaneously. We referred to this signal as the lesion index.

### 3.3.3 Illustration of Lesion Index as Indicator of Storage Lesion in Individual RCCs

The regulatory guidelines for the quality assessment of RCCs are mainly based on the measurement of the hemolysis level. To generate a morphological parameter that complies with regulatory guidelines for the quality control of RCCs, it is important to show that this morphological parameter correlates with the hemolysis level in RCCs. Therefore, we measured the hemolysis level for each RCC synchronously with the morphometric concentration data. From these data, we calculated correlation coefficients for each class signal as well as for the MI and lesion index with respect to the hemolysis level. The measurement data with the resulting correlation coefficients are shown in Table 4, having been generated by the dataset B of five RCCs.

**Table 4. Hemolysis and morphological measurement data with resulting correlation coefficients.** The data was generated by the dataset B of five RCCs.

<b>Hemolysis</b>	<b>Trilobe</b>	<b>Deformed stomatocyte</b>	<b>Stomatocyte</b>	<b>Discocyte</b>	<b>Echino-cyte1</b>	<b>Echino-cyte2</b>
0.09	1.91	0.78	37.97	41.56	11.33	1.78
0.09	1.70	1.58	31.61	39.71	12.11	2.73
0.10	0.97	1.76	42.93	27.45	11.69	2.99
0.10	1.36	1.07	33.57	37.92	14.20	2.91
0.17	1.57	1.86	20.38	31.85	16.34	3.56
0.19	3.89	2.22	21.70	27.00	15.49	3.76
0.21	2.22	1.79	35.24	26.29	13.18	2.49
0.24	2.43	2.24	32.26	19.81	16.50	3.85
0.26	2.52	0.96	29.69	28.81	19.51	3.41
0.29	4.41	2.32	20.27	25.91	14.75	3.81
0.31	1.56	0.77	24.71	35.76	17.40	3.40
0.31	4.13	2.53	25.02	22.96	16.91	3.59
0.33	2.66	1.64	17.03	35.18	17.30	2.95
0.42	2.31	1.11	17.96	30.49	18.60	4.49
0.64	2.06	1.88	24.81	21.25	18.16	3.97
0.65	3.80	4.27	30.87	14.36	15.54	3.18
0.69	1.38	0.65	26.90	25.99	18.42	2.94
1.04	3.08	1.55	15.34	23.33	18.21	4.34
1.15	3.22	3.49	27.68	18.90	13.83	2.82
1.23	2.77	3.72	35.81	17.04	9.31	2.07
1.48	1.03	1.42	26.91	15.36	19.91	4.94
1.76	1.45	1.52	37.35	15.00	14.88	2.16
2.58	6.42	7.74	37.62	10.14	6.53	2.05
2.75	2.18	1.53	19.79	16.67	18.65	4.68
4.77	0.60	1.71	17.41	15.61	14.74	3.48
5.46	1.63	6.17	47.82	6.87	9.31	1.96
9.01	1.57	0.51	15.22	20.75	14.23	2.58
9.89	1.22	2.18	23.64	12.64	16.11	4.36
15.29	1.34	1.07	13.28	13.01	14.01	3.23
15.42	0.97	3.72	21.50	9.83	6.76	1.88
<b>correlation coefficient:</b>	<b>0.109</b>	<b>0.012</b>	<b>0.103</b>	<b>0.327</b>	<b>0.125</b>	<b>0.028</b>

<b>Hemolysis</b>	<b>Echinocyte3</b>	<b>Sphero- echinocyte</b>	<b>Spherocyte</b>	<b>Morphological index</b>	<b>Lesion index</b>
0.09	4.08	2.22	0.29	0.94	0.58
0.09	9.89	7.96	5.29	0.90	0.67
0.10	10.40	6.25	5.90	0.89	1.81
0.10	8.08	6.83	10.29	0.90	0.88
0.17	19.29	1.66	0.15	0.80	5.16
0.19	20.99	4.98	1.48	0.79	4.95
0.21	16.27	5.65	2.17	0.85	2.51
0.24	16.45	6.18	4.01	0.80	6.45
0.26	10.26	0.42	0.17	0.85	4.85
0.29	20.71	2.79	2.06	0.77	7.83
0.31	10.63	2.77	3.01	0.84	5.77
0.31	18.60	4.13	6.95	0.79	6.26
0.33	16.96	0.71	0.17	0.80	6.28
0.42	18.45	4.35	1.93	0.78	6.59
0.64	17.68	4.09	2.50	0.76	10.19
0.65	17.45	5.36	5.16	0.77	10.52
0.69	12.63	6.40	6.86	0.79	11.08
1.04	20.89	0.62	0.05	0.71	13.26
1.15	16.81	4.30	0.86	0.75	13.26
1.23	17.13	3.84	1.10	0.77	12.15
1.48	16.95	6.66	6.82	0.73	13.49
1.76	9.19	6.76	11.68	0.76	18.44
2.58	12.39	3.98	2.28	0.77	17.12
2.75	17.30	7.77	11.44	0.69	19.20
4.77	18.88	11.85	15.72	0.62	27.58
5.46	7.35	7.68	11.21	0.78	18.89
9.01	14.48	10.03	20.64	0.63	30.67
9.89	17.18	9.48	13.18	0.67	22.66
15.29	18.03	11.49	24.54	0.56	36.04
15.42	9.40	10.91	35.03	0.56	45.94
<b>correlation coefficient:</b>	<b>0.002</b>	<b>0.514</b>	<b>0.801</b>	<b>0.665</b>	<b>0.837</b>

Among all morphological signals, only spherocytes (SP), spherocytocytes (SE), morphological index (MI) and lesion index show a strong correlation with hemolysis. Out of these signals, the spherocytocyte (SE) concentration shows the weakest correlation. Therefore, it is even more interesting that the lesion index, which is composed of SE and SP concentrations, has the best correlation with hemolysis among all morphological signals. To further illustrate the correspondence between the progressively increasing lesion index and the progressively increasing hemolysis, the

respective measurements for each individual RCC are shown in Figure 30. Data points represent the simultaneous measurements of lesion index and hemolysis level between weeks 2 and 12 of the storage period of each RCC from the dataset B.

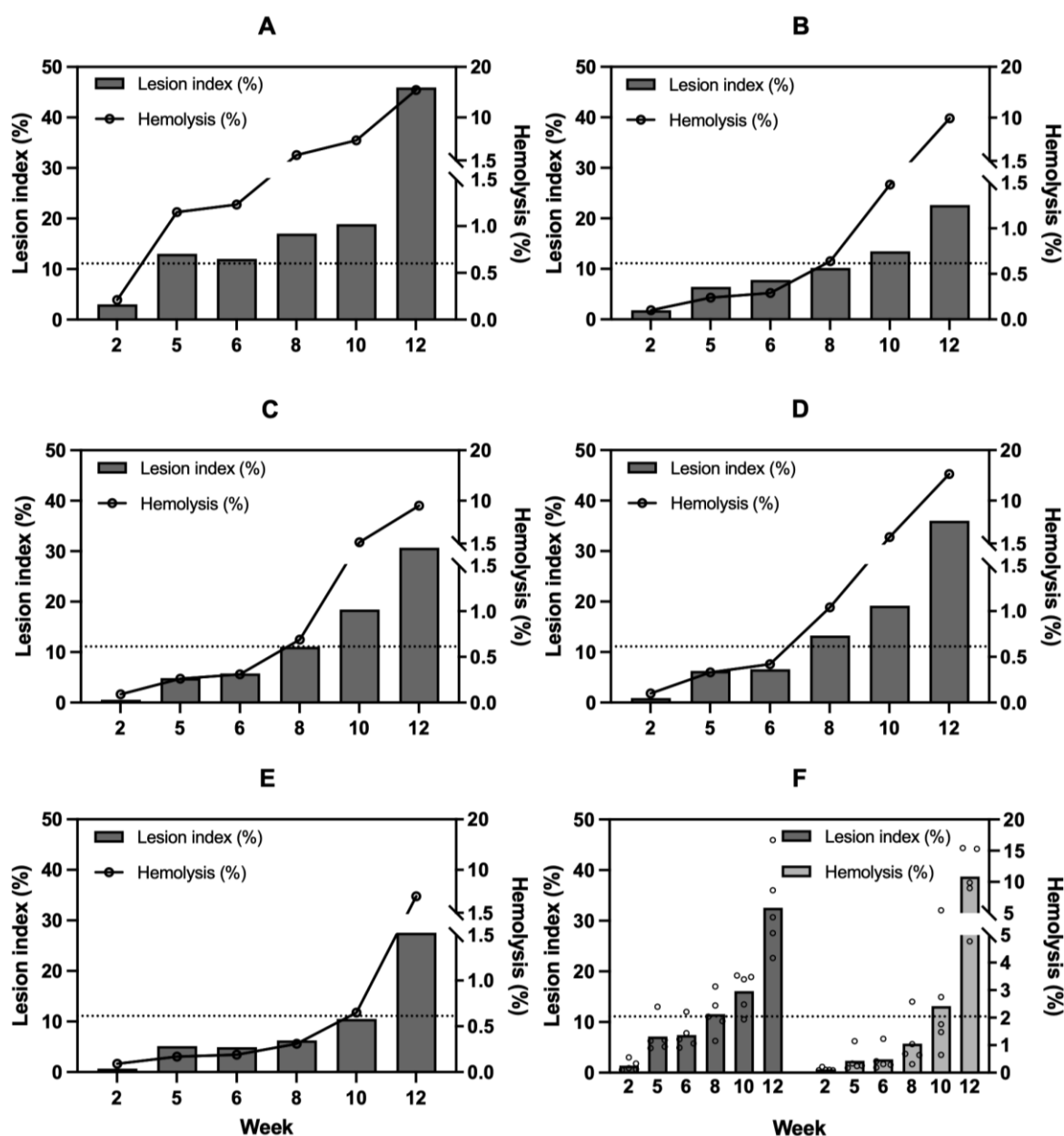


**Figure 30. Comparison of lesion index and hemolysis level in individual RCCs.** A-E: For five individual RCCs, lesion indices (depicted as bars) are plotted against time. For comparison, the respective hemolysis levels are plotted as data points connected by lines for visual reference. F: Mean values of lesion index and hemolysis determined over the total set of RCCs are plotted against time. Each data point is constituted by the measurement of three technical replicates. The dotted lines represent a lesion index threshold of 11.1%, which evaluates the acceptability of RCCs in the same manner as the hemolysis threshold.

In each case, the lesion index and the hemolysis level increase continuously throughout the storage period. However, the individual RCCs exhibit strong variances

between donors. For example, the RCC in Figure 30A already shows a remarkable high hemolysis value at week 5: this value is above the regulatory guideline threshold of 0.8% hemolysis, which is the minimum quality that an RCC has to have in order to be used for transfusion. The corresponding lesion index also indicates exceptionally high values, so that in week 5 it is above a provisionally established threshold of 11.1% (see below for further explanation of this threshold). In contrast, the RCC in Figure 30E shows much lower hemolysis values; throughout the storage period until week 10, they remain below the regulatory guideline threshold of 0.8%. During this period, the corresponding lesion index also remains below the preliminary set threshold of 11.1%. In order to depict a general trend of the individual observations (A-E), the mean values (over the total set of RCCs) of the lesion index and the hemolysis level are shown as functions of time in Figure 30F. The error bars (CI95%) indicate the strong inter donor variance between the different donors depicted in A-E.

#### 3.3.4 The Lesion Index as Indicator for the Hemolysis Level

The results displayed above show that the lesion index strongly correlates with hemolysis levels. The next step was to observe whether the lesion index is a suitable predictor variable for hemolysis. In other words, can the lesion index be used to predict the hemolysis level in an RCC, such that it confirms compliance with regulatory guidelines? To ascertain this, we plotted the lesion index data points of the five RCCs against their respective measured hemolysis level in a scatter plot (see Figure 31). In this scatter plot we set a threshold for the lesion index that corresponds to the hemolysis threshold of 0.8% above which RCCs must be discarded.

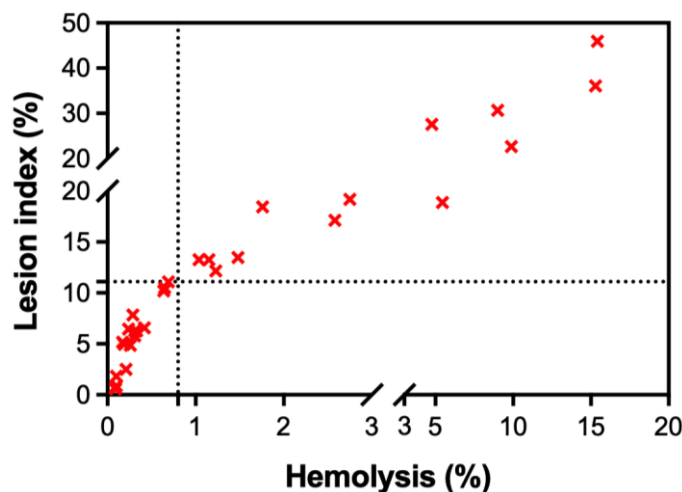


**Figure 31. Lesion index as hemolysis predictor variable.** A: data points represent all simultaneous lesion index / hemolysis measurements performed on all five RCCs. The dashed lines show the RCC quality threshold (lesion index = 11.1% and hemolysis level = 0.8%). B: data points also show all simultaneous MI / hemolysis measurements carried out on all five RCCs. The MI threshold of 0.78 (dashed lines) corresponds to the hemolysis threshold of 0.8%.

The data plot in Figure 31 reveals a high correlation ( $R^2 = 0.84$ ) between the lesion index and the hemolysis level as extracted from the entire dataset of all RCCs from several donors. Based on this dataset, we set a lesion index threshold of 11.1%, which is equivalent to a critical hemolysis level of 0.8%. This implies that a morphological threshold of 11.1% may predict the compliance of a RCC regarding the 0.8% hemolysis limit (Bundesärztekammer, 2020) within the context of blood bank storage. However, this morphological threshold is only preliminary because the sample group of 5 RCCs is small and therefore statistically limited. For comparison, similar data plots with thresholds for all MI, spherocytosis and spherocyte data points against their corresponding hemolysis values are shown in Figure 32.

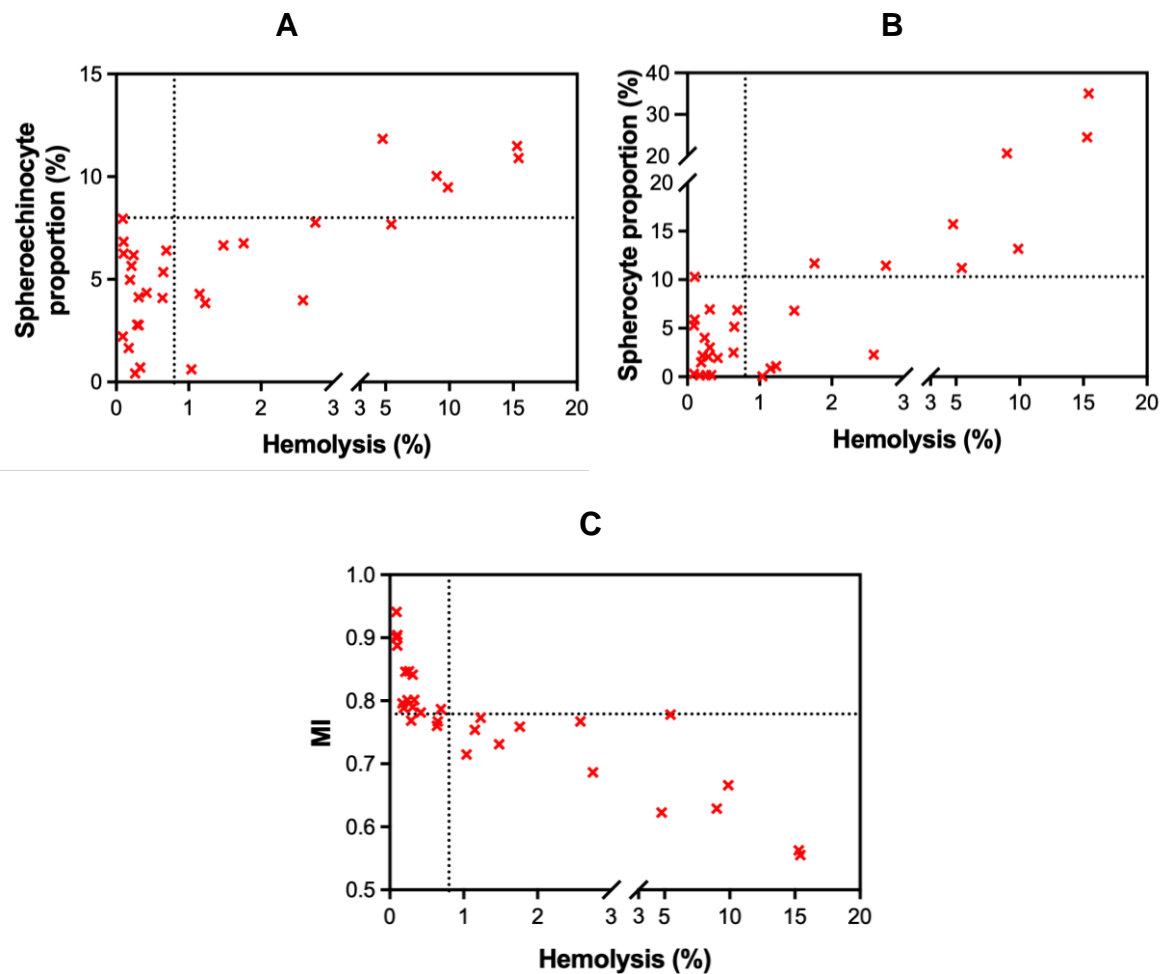


**Figure 32. Spherochinocyte proportion, spherocyte proportion and MI as hemolysis predictor variable.** A: data points represent all simultaneous spherochinocyte proportion / hemolysis measurements performed on all five RCCs. The dashed lines show the RCC quality threshold (spherochinocyte proportion threshold = 8.0% and hemolysis level = 0.8%). B: data points also show all simultaneous spherocyte proportion / hemolysis measurements carried out on all five RCCs. The spherocyte proportion threshold of 10.3% (dashed lines) corresponds to the hemolysis threshold of 0.8%. C: data points show all simultaneous MI and hemolysis measurements carried out on all five RCCs. The dashed lines show the obtained RCC quality thresholds (MI threshold = 0.78 and hemolysis level = 0.8%).

Compared to the lesion index, the concentration signal of class SE shows substantially less correlation ( $R^2 = 0.51$ ) with hemolysis and is therefore less suitable for the prediction of the hemolysis level. Even the concentration of the spherocyte class (SP) alone does not correlate as well with hemolysis ( $R^2 = 0.80$ ) as the lesion index. A similarly inferior performance is given by the morphological index MI (as defined in section 2.3). With respect to hemolysis, it exhibits a correlation coefficient of only  $R^2 = 0.67$ . Similar to the case of the lesion index, equivalent thresholds for SE, SP and MI can be found that correspond to the hemolysis threshold of 0.8%. However, these thresholds could not be set to generate correct predictions for all data points. For example, an optimized value of 0.78 for the MI threshold leads to the correct prediction of 27 out of a total of 30 data points, i.e., in which there are 3 false positive events.

Therefore, the performance of the MI as a predictor variable for the hemolysis criterion is inferior when compared to the lesion index. The same is true for the performance of SE and SP proportions, each of which is used alone as a predictor variable for the hemolysis criterion.

### 3.4 Non-inferior RCC Quality after Repeated Air Rescue Mission Transport for Prehospital Transfusion

#### 3.4.1 A Rotation System Allows Regulatory-compliant Storage and Transport Logistics of RCCs for Repeated Air Rescue Missions

Having established the system for the morphologies of RBCs through Flow Morphometry and CNN, and after verifying the ability of this system to monitor time-dependent changes of RBC morphologies, we proceeded to apply our system to evaluate possible RBC deteriorations due to repeated air rescue mission transport for prehospital transfusion. As mentioned already, more and more air rescue missions aim to provide RCCs for emergency prehospital transfusion. Yet, it remains an open question whether the RBCs become compromised. We regarded our system as presenting a unique opportunity to assess quantitatively these possible changes and correlate them to biochemical parameters.

We carried out the entire study during a period of regular air rescue missions. The highest standards of quality control and temperature monitoring were applied in accordance with German hemotherapy guidelines at all times. A brief overview of the sample distributions for the different measurements is shown in Figure 33. Identically to routine operations, not all RCCs could be used before their expiration date. We therefore had to exclude some RCCs early because they failed during visual quality control. These excluded RCCs were consequently significantly younger compared to those that had reached their expiration date. Samples included in the statistical analysis of this study had to meet certain criteria. Only samples that remained within the temperature limits (2-6°C) during use were included. Furthermore, they had to be older than 30 days at the time of their exclusion from the study.

A total of 81 rhesus D-negative RCCs of blood group 0 were included in the flight group and a total of 50 rhesus D-positive RCCs of blood group AB were included in the control

group. RCCs were dispatched between 7 and 13 times, with the average being 11 times before they were excluded from the study, mainly because they had reached the end of their shelf-life. The average flight time was 18.3 hours, with a minimum of 6.6 hours and a maximum of 28.8 hours. Within the flight group, a total of 30 RCCs were used for prehospital transfusions during the study (Rudolph et al., 2021).

Flight group	Sample numbers		Control group
	81	50	
Transfused	30	-	
Biochemical end-point measurements (Hb, free Hb, Hkt, hemolysis, MCV, potassium, pH)	51	50	Biochemical end-point measurements (Hb, free Hb, Hkt, hemolysis, MCV, potassium, pH)
	6   <b>45</b>   48   2		
Morphology end-point measurement	36	42	Morphology end-point measurement
	1   <b>35</b>   40   2		
Morphology change rate measurement (end-point – initial)	24	26	Morphology change rate measurement (end-point – initial)
	1   <b>23</b>   24   2		

**Figure 33. RCC subgroups in the flight and control group presented separately with regard to different quality control measures.** RCCs included in the study and analysis are indicated by bold numbers. The number of samples excluded from the analysis due to temperature deviations or failure of visual inspection are indicated by gray boxes. Samples were only analyzed if they had been stored for longer than 30 days. Figure adapted from (Boecker et al., 2022).

The handling of RCCs used in the rotation system ensured compliance with the regulatory guidelines, in particular for the defined transport temperature ranges. Our rotation system consisted of three steps, with one day of packing (preparing the cool boxes with the RCCs and adjusting the correct temperature), one day of transport, and one day of quarantine storage throughout the entire RCC shelf life (for more detail see section 2.5.1). The project ran over a total period of 12 months and thus covered all typical seasonal temperatures and daylight characteristics. In Figure 33 a small amount of RCCs that could not be included in the statistical analysis is represented (grey fields). Only four of the 131 RCCs in total showed problems with temperature deviations, which corresponded to two in each study group. We had to exclude three additional units from the study after visual inspection because they seemed to indicate hemolysis. However, the suspicion of hemolysis was not confirmed by the quantitative

measurement. None of the samples, regardless of whether they were included or excluded from the statistical analysis, revealed measurement values that fell outside the guidelines for hemotherapy. The rotation system introduced was suitable in practice, insofar as it allowed packaging, transportation and storage of RCCs with quality assurance between cycles.

### 3.4.2 Biochemical Parameters of RBC Quality Show Non-Inferiority of RCCs after Repeated Air Rescue Missions

The next step was to examine whether repeated air rescue missions could influence the quality features of the erythrocytes. The German hemotherapy guidelines require that the integrity of the RCC bags is documented such that no hemolysis occurs during visual inspection and that the hemolysis rate at the end of the shelf life is below 0.8%. Figure 34 summarizes the biochemical measurement data of all used RCCs. This graph allows for direct comparison of the flight group and the control group with respect to the biochemical quality parameters, whereby each value is measured after the corresponding RCCs were excluded from the rotation system. For the comparison we used the following parameters: hematocrit, free hemoglobin, hemolysis, MCV, potassium and pH.

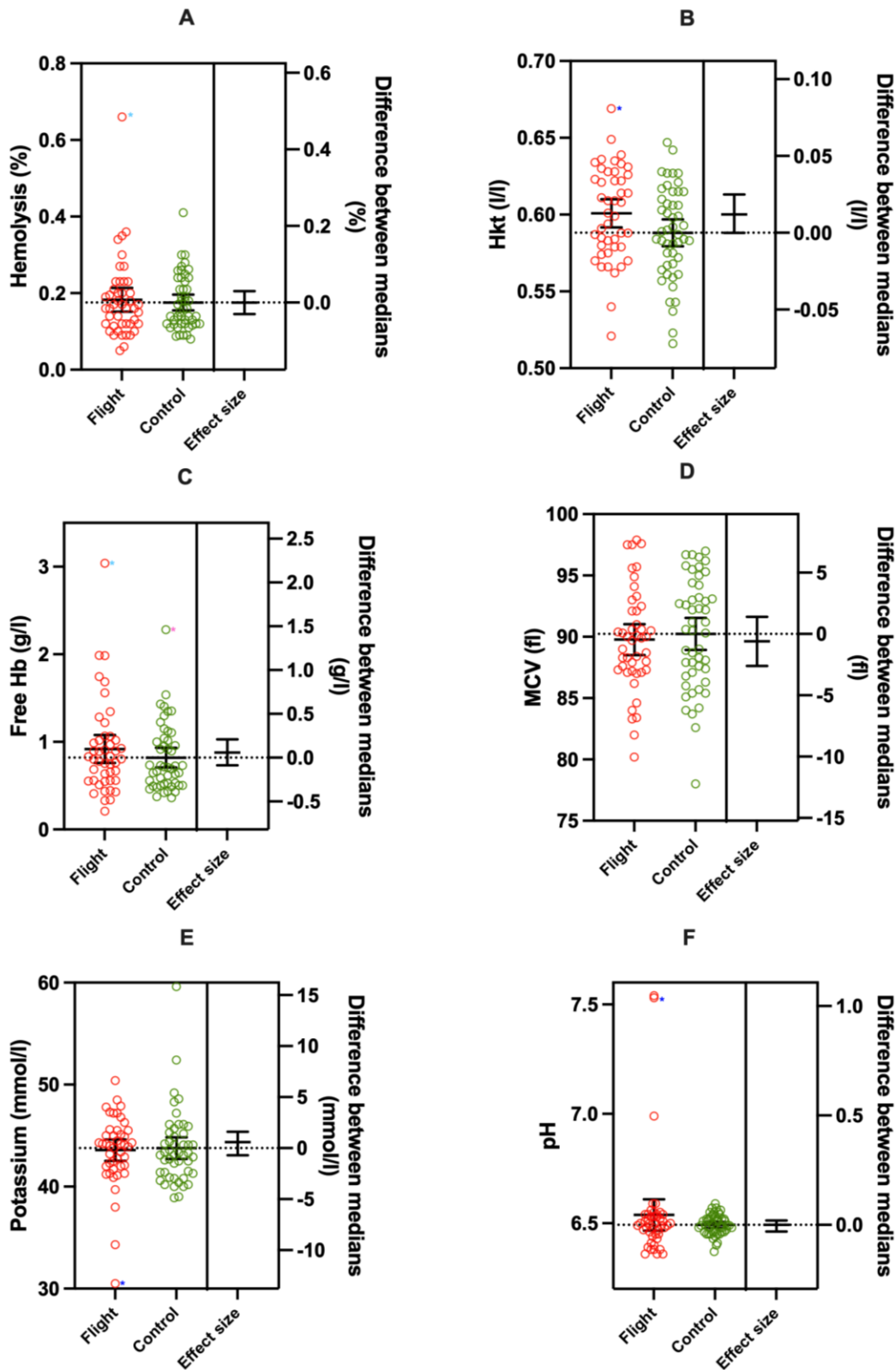


**Figure 34. Biochemical parameter comparison of RCCs in flight and control groups.** The biochemical parameters (hemolysis, Hkt, Free Hb, MCV, potassium and pH) are shown on the left y-axis and the Hodges-Lehmann estimate is shown on the right y-axis. The sample groups (n= 45 flight and n= 48 control groups) are shown as scatterplots with means and confidence intervals (CI95%). The Hodges-Lehmann estimate including the requested range of CI95% indicates the potential effect size of the flight. The effect sizes of biochemical parameters with their respective p values and CI95% were as follows: A Hemolysis: 0.0 (%) (p= 0.962, CI= -0.03 to 0.03 (%)); B Free hemoglobin: 0.059 (g/l) (p= 0.396, CI= -0.088 to 0.209 (g/l)); C Hematocrit: 0.012 (l/l) (p= 0.053, CI= 0.00 to 0.025 (l/l)); D MCV: -0.6 (fl) (p= 0.542, CI= -2.6 to 1.4 (fl)); E potassium: 0.6 (mmol/l) (p= 0.396, CI= -0.7 to 1.6 (mmol/l)); and F pH: 0.0 (p= 0.983, CI= -0.03 to 0.02). Noticeable samples that correlate with lesion index measurement are marked with a colored star. Figure adapted from (Boecker et al., 2022).

The measured variables are plotted according to the scale of the left vertical axis. On the right side (with reference to the right vertical axis) the Hodges-Lehmann estimate of the difference of the medians is plotted. This estimate, together with its requested range of the 95% confidence interval, represents the measured effect size of the flight and its statistical uncertainty. The effect sizes of the biochemical parameters with corresponding p-values and CI95% were as follows: 0.012 (l/l) (p= 0.053, CI= 0.0 to 0.025 (l/l)) - hematocrit; 0.059 (g/l) (p= 0.396, CI= -0.088 to 0.209 (g/l)) - free hemoglobin; 0.0 (%) (p= 0.962, CI= -0.03 to 0.03 (%)) - hemolysis; -0.6 (fl) (p= 0.542, CI= -2.6 to 1.4 (fl)) - MCV; 0.6 (mmol/l) (p= 0.396, CI= -0.7 to 1.6 (mmol/l)) - potassium and 0.0 (p= 0.983, CI= -0.03 to 0.02) - pH.

At the time of the end-point measurements, all corresponding RCC bags were intact and their concentrates had a hemolysis rate below the 0.8% threshold. We could observe no clinically relevant effects between the flight and control samples with respect to any of the assessed biochemical parameters (Figure 34).

### 3.4.3 Flow Morphometric Analysis Confirms Non-Inferiority of RCCs after Repeated Air Rescue Missions

We based the morphometric analysis of the quality of the two sample groups (flight and control) in the context of helicopter transport entirely on the above introduced lesion index. The lesion index is the sum of the relative concentrations of the spherical morphologies SE and SP. RBCs which possess these morphologies have reduced oxygen transport capacity and are immediately eliminated by the human body after transfusion (Deplaine et al., 2011; Roussel et al., 2021). Sampling from RCCs used in routine is a critical task, once a sample is extracted with a syringe, the unit must be used immediately or discarded. To circumvent the critical extraction by syringe, we used two different sampling methods (pouch and segment technique) (see section 2.5.2). We compared these sampling techniques to see whether there were any differences in the samples due to the two methods (see Figure 35).

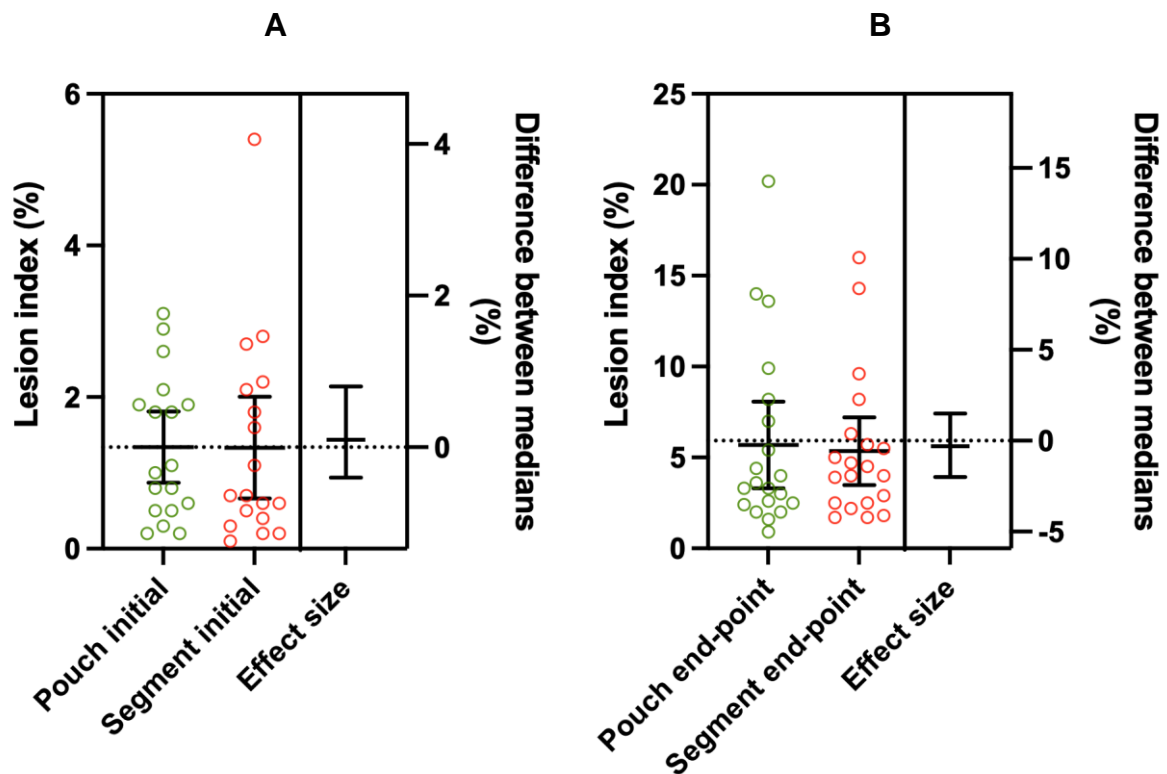


**Figure 35. Sampling mode analysis of lesion index.** The initial sampling (pouch  $n=18$ , segment  $n=18$ ) (A) and the end-point sampling (pouch  $n=20$ , segment  $n=20$ ) (B) of the lesion index are shown on the left y-axis and the Hodges-Lehmann estimate is shown on the right y-axis. The sample groups are shown as scatterplots with means and confidence intervals (CI95%). The Hodges-Lehmann estimate including the requested range of CI95% indicates the potential effect size of the different sampling method. The effect size of the initial sampling is measured as 0.1% with its respective p value 0.589 and CI95% ranging from -0.4 to 0.8%. The effect size of the end-point sampling between pouch and segment sampling is -0.3%, with a p-value of 0.743 and a CI95% ranging from -2.0 to 1.5%.

The statistical analysis in Figure 35 did not exhibit any biological or clinically important differences between these sampling techniques and thus generated no measurement bias.

To characterize the morphological quality of the RCCs, we performed two types of measurements. One measurement is a simple end-point measurement, i.e., a final measurement of the individual proportions of morphology classes, just before the RCC is discarded. The other measurement determines the net change (i.e., RBC aging) of these proportions in the RCC, beginning from the point when it enters the study and ending until it is sorted out. We evaluated the results of both measurements by computing the lesion indices and the morphological indices MI separately for the flight and the control group. A summary of the determined end-point lesion indices and their net changes during this study are shown in Figure 36. A similar summary for the MI data is shown in Figure 37.

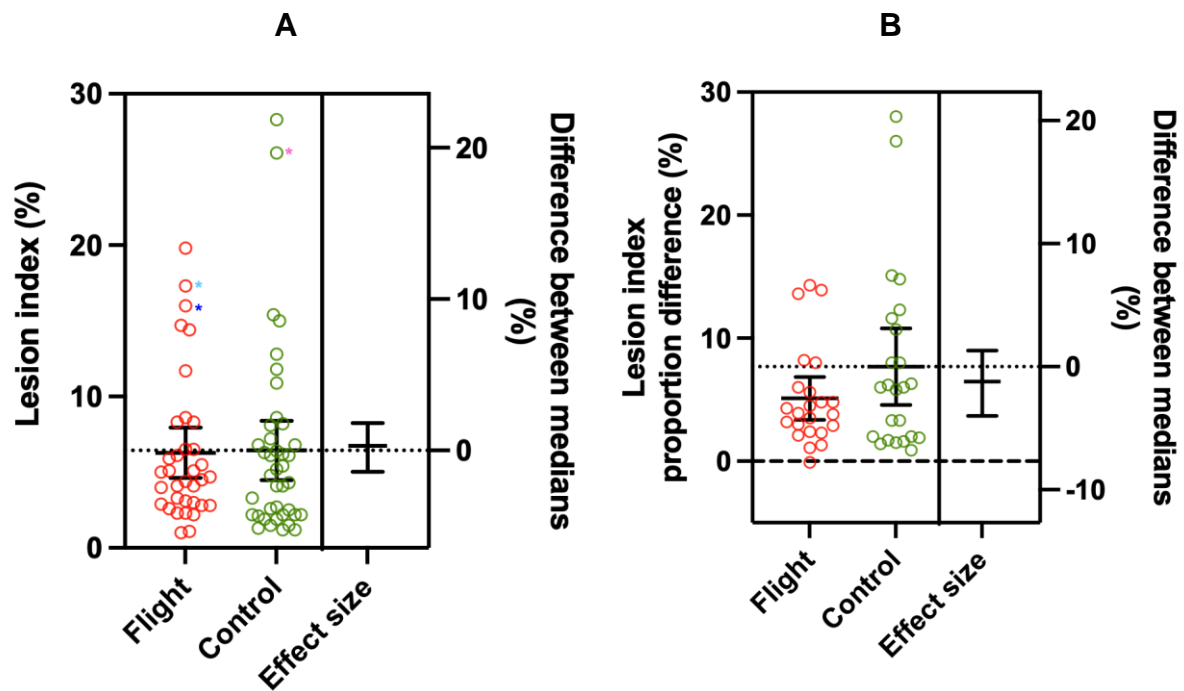


**Figure 36. Flow morphometry of lesion index.** The percentage of the lesion index (end-point measurement; flight  $n = 35$ , control  $n = 40$ ) is shown in (A). The change in this proportion between the initial and end-point measurement of each RCC (net change; flight  $n = 23$ , control  $n = 24$ ) is shown in (B). Sample groups are shown as scatter plots with mean and CI95%. (A) and (B) each show a second y-axis indicating the Hodges-Lehmann estimates for the flight and control groups (effect size). The effect size of the lesion index caused by flights is measured as 0.3%, with a p-value of 0.655 and a CI95% ranging from -1.4 to 1.8%. The effect size of the lesion index net change between the initial and end-point measurements is -1.2%, with a p-value of 0.389 and a CI95% ranging from -4.0 to 1.3%. Noticeable samples that correlate with biochemical measurements are marked with a colored star.

The left vertical axis scales the lesion index (A) and correspondingly its net change (B). Both right vertical axes in A and B scale the Hodges-Lehmann estimates, assessing the impact of helicopter transport as the difference between medians. We used the Hodges-Lehmann estimate shown here with requested CI95% as an illustrative measure of the effect due to the helicopter transport. The lesion index exhibits an effect size of 0.3% with a p-value of 0.655 and CI95% ranging from -1.4 to 1.8%. This means that there is no significant difference between the flight and the control group with respect to the final lesion index.

The effect size of the net change of the lesion index is -1.2%, with a p-value of 0.389 and CI95% from -4.0 to 1.3%. This means that there is also no significant difference between the flight and the control group with respect to the net change of the lesion index during the residence time of the RCCs in the rotation system.

In agreement with the biochemical data, the morphological data of the flight and control groups exhibit no clinically relevant differences.

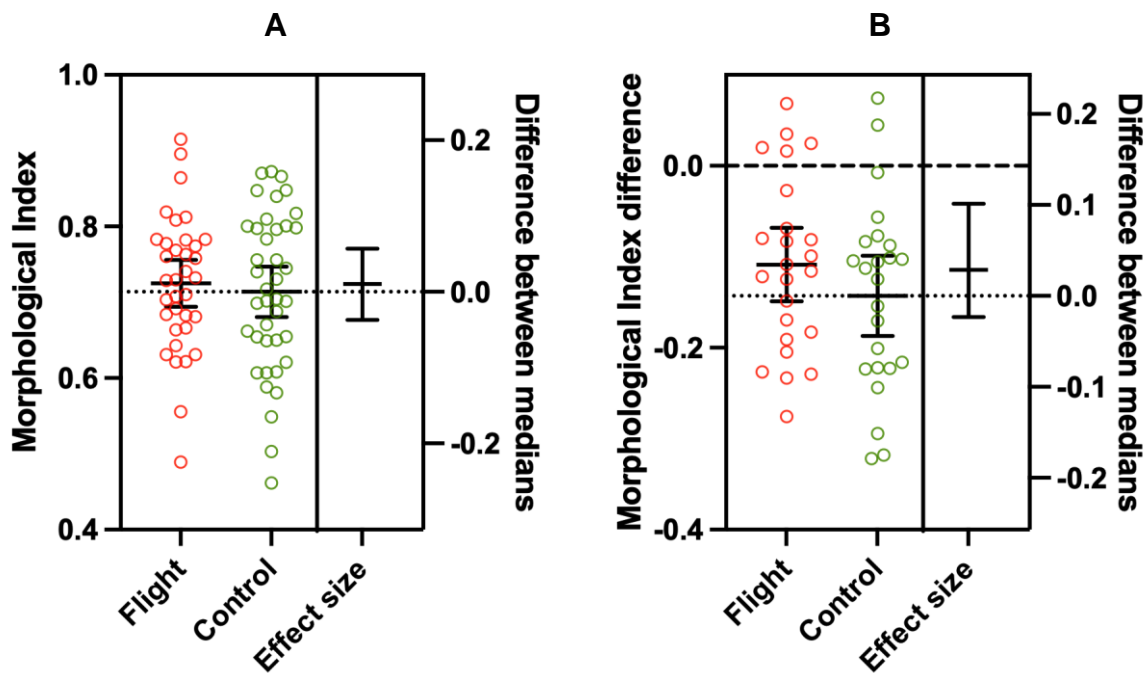


**Figure 37. Flow morphometry of morphological index.** The percentage of the morphological index (end-point measurement; flight  $n = 35$ , control  $n = 40$ ) is shown in (A). The change in this proportion between the initial and end-point measurement of each RCC (net change; flight  $n = 23$ , control  $n = 24$ ) is shown in (B). The sample groups are depicted as scatter plots with mean and CI95%. (A) and (B) each show a second y-axis representing the Hodges-Lehmann estimates for the flight and control groups (effect size). The effect size of the MI caused by flights is measured as 0.01, with a p-value of 0.724 and a CI95% ranging from -0.04 to 0.06. The effect size of the MI net change between the initial and end-point measurements is 0.028, with a p-value of 0.32 and a CI95% ranging from -0.02 to 0.1.

According to the results of the lesion index, the results of the MI are shown in an identical way. The left vertical axis scales the morphological index (A) and correspondingly its net change (B). In the same way, both right vertical axes in A and B scale the Hodges-Lehmann estimates. The MI exhibits an effect size of 0.01 with a p-value of 0.724 and CI95% ranging from -0.04 to 0.06%. The effect size of the net change of the MI is 0.028 with a p-value of 0.32 and CI95% from -0.02 to 0.1%.

Like the lesion index, the MI data showed no clinically relevant differences between the two groups either.

Another important observation was that samples with particular biochemical parameter values (extremely high/low) also exhibited strongly increased values in the morphological measurement. For example, the samples that stood out with a hemolysis level of 0.66% were also identified by a high morphological lesion index value of 17.3%. We labelled those samples which had a correlated high morphological and biochemical values in Figure 34 and Figure 36 with identically colored stars.

#### 3.4.4 RBC Quality Parameters were not Affected by Flight Time Duration

The above results document the non-inferiority of RBC quality parameters after repeated air rescue missions with respect to total flight duration. In addition, we calculated the correlation between quality parameters and total flight duration using simple linear regression models. All measurement values were analyzed for correlation with the flight time duration. The results are shown in Figure 38.

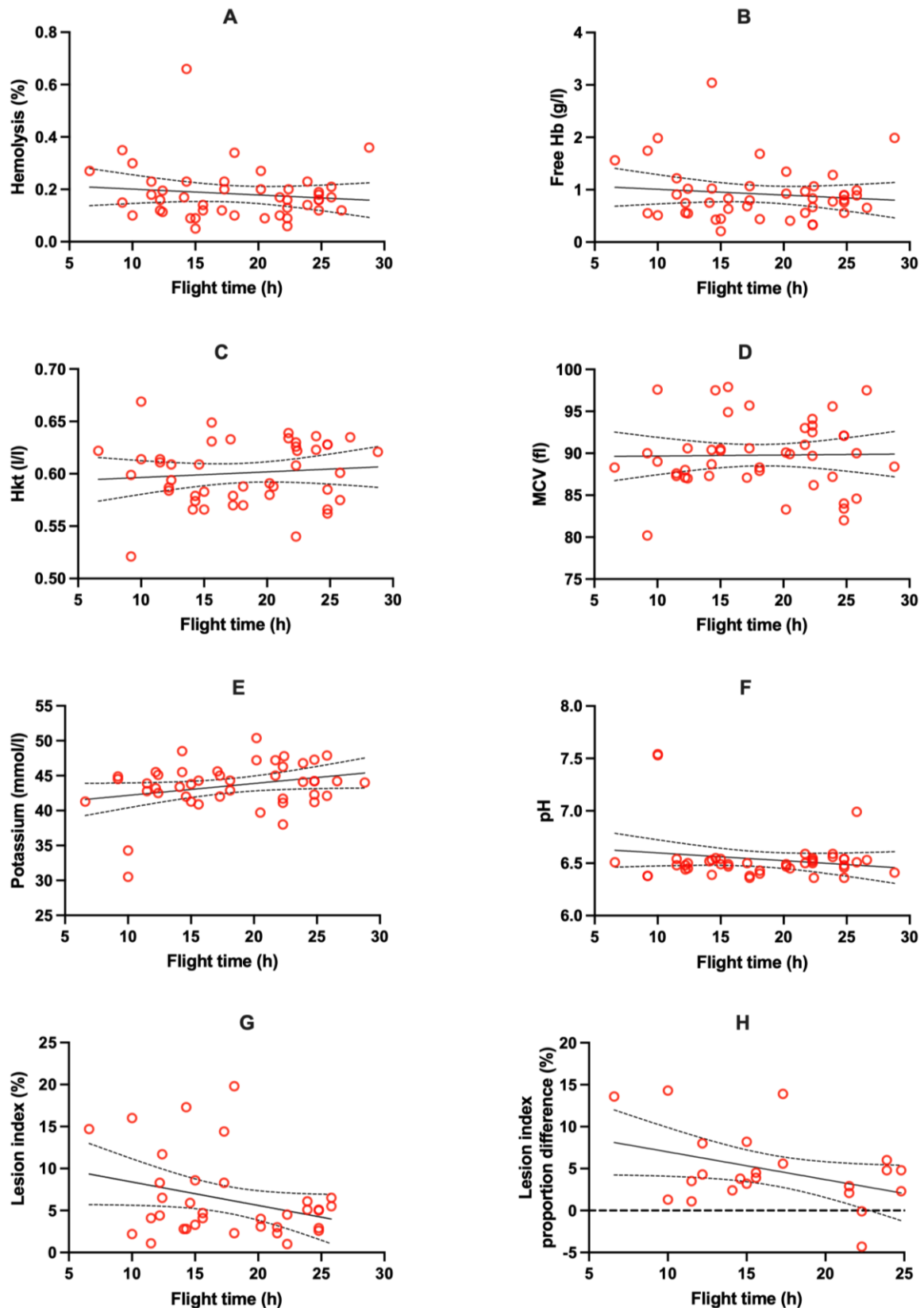


**Figure 38. Correlation between flight duration and RBC quality characteristics.** Biochemical (A-F, n = 45) and morphological (G, n = 35; H, n = 23) parameters plotted against flight duration. The straight lines depict linear regression fittings. The confidence bands of the fitted lines are depicted by the dashed curved lines. The slopes of the straight lines along with the regression coefficients and the p values for the difference of these slopes from zero are as follows: A Hemolysis: -0.002,  $R^2=0.003$  ( $p=0.42$ ); B Free hemoglobin: -0.011,  $R^2=0.014$  ( $p=0.43$ ); C Hematocrit: 0.001,  $R^2=0.010$  ( $p=0.51$ ); D MCV: 0.012,  $R^2=0.0$  ( $p=0.92$ ); E Potassium: 0.171,  $R^2=0.079$  ( $p=0.06$ ); F pH: -0.007,  $R^2=0.032$  ( $p=0.24$ ); G Lesion index: -0.279,  $R^2=0.099$  ( $p=0.07$ ); H lesion index proportion difference (aging effect) -0.330,  $R^2=0.163$  ( $p=0.06$ ). Figure adapted from (Boecker et al., 2022).

The linear regression coefficients with the p-values of the obtained slope's difference with respect to zero for the biochemical parameters were as follows: 0.010 ( $p= 0.51$ ) - hematocrit, 0.014 ( $p= 0.43$ ) - free hemoglobin, 0.003 ( $p=0.42$ ) - hemolysis, 0.0 ( $p= 0.92$ ) - MCV, 0.079 ( $p= 0.06$ ) - potassium and 0.032 ( $p= 0.24$ ) - pH. The values of all linear regression coefficients are close to zero which indicates that the flight time does not correlate with one of the biochemical parameters. The slopes of the linear regression models are not significantly different from zero.

Similar results are obtained from the lesion index data. The linear regression coefficient for the correlation of the lesion index is 0.099, with a p-value of 0.07 for the slope's differences with respect to zero. The linear regression coefficient for the net changes of the lesion index is 0.163, with a p-value of 0.06 for the slope's differences to zero.

## 4 DISCUSSION

This study presents a classification of RBC morphology with a high resolution in a flow chamber by combining flow morphometry and a trained convolutional neural network. Through the introduction of the CNN-based image classification we could achieve all aims. The following aspects of the achieved results will be discussed:

- 1) Greatly improved classification resolution and accuracy using CNNs in the image classification;
- 2) Morphometric measurement with the inclusion of shear induced morphologies in flow chambers;
- 3) Lesion index (= sum of SE and SP proportions), which is a suitable predictor variable for hemolysis level;
- 4) Lesion index, which provides additional information as storage lesion marker;
- 5) Standardization of sample and measurement preparation of flow morphometry to generate a robust signal; and
- 6) Non-inferiority of RCC quality after repeated air rescue mission transport.

### 4.1 Improved Classification Resolution of RBC Morphologies by CNNs

In this project, we coupled a custom-made flow morphometry system to an CNN-based image classification method instead of a binary decision tree-based analysis. Current limitations of the image analysis of RBCs are either a low classification resolution or a low classification accuracy. Using the CNN-based image classification method, we achieved to classify RBCs into nine morphology classes with a high overall accuracy of 92%. The corresponding F1-scores for detailed accuracy specification of each morphology class ranged from 84% to 97%. To put this improvement in perspective, these numbers were compared to the previous decision tree-based studies. Those RBC classifications systems achieved in similar microfluidic systems overall accuracies of 75% for eight RBC classes (Piety et al., 2015) or comparable accuracies to those of CNNs, but for a maximum of three RBC classes in total (Piety et al., 2015; Sierra et al., 2017).

**Table 5. Different classification systems with corresponding classification accuracies.** Classification accuracy for Sierra et al. had to be assumed because no accuracy validation of the system was reported. Assumption was made on the basis of the results in section 3.2.4.

Classification system	RBC morphology classes	Classification accuracy
CNN	9	92 %
CNN	3	97 %
Sierra et al.	3	~ 92 - 94 %
Piety et al.	8	75 %
Piety et al.	3	92 %

These results show that our CNN is well equipped for the task of the image classification of RBC morphologies. This seems to be true not only for the CNNs based on the architecture of GoogLeNet but in general for CNNs (see section 3.2.1, ResNet50 results and (Boecker et al., 2022)). Nowadays, CNNs are increasingly used in many areas of medical image analysis because they achieve better classification accuracy without the need for tedious feature selection procedures (Greenspan et al., 2016; Litjens et al., 2017; Shen et al., 2017). The main advantage of CNNs is that they locate the required features of the different RBC morphologies independently and adjust the optimal values (weights) that lead to the correct classification into the different morphology classes. Furthermore, the extracted features do not have to be typical global features of the cells, such as border roughness, texture inhomogeneity, equivalent diameter or non-circularity, as it is in the case of decision trees (Sierra et al., 2017). The features, patterns and threshold (weights) used by the CNN are automatically learned without human supervision. They can be as global as the decision tree features above or they can account for small differences between cell types, such as smaller bumps or a weaker contrast ratio of certain cell regions. During training, the discrimination of these features and their weights are improved in every iteration step. In this way, they can only be passively influenced via training options and the training data. The preparation of training material with defined RBC morphologies is therefore of highest importance, and a time-consuming step. The training options set by the user and the training data can have a large impact on the resulting classification and was therefore evaluated after each training. We carry out the evaluation of the CNN by assessing a confusion matrix that is generated for each training and by visually inspecting the morphology classes of the sorted RBCs. The

training data, however, has a much greater impact and is therefore key to a good classification of the trained CNN. The training data must be specific enough so that the different morphology classes can be distinguished. At the same time, it needs to be general enough so that slight variances in the cell micrographs are still properly classified. This can be achieved by heterogenic training data and can be further enhanced by augmentation. As a result, the trained CNN becomes robust to variations in the RBC micrographs obtained by different experiments, for example different exposure and contrast ratios of the cells or different orientations of the RBCs within a morphology class. This is a major advantage of CNNs compared to decision tree classification and other supervised classification systems, as these systems are much more rigid and focused on a specific application, and do not cope well with variations in the image data (Sierra, 2017). As our results show, generating heterogenic training data and finding good training options as well as a suitable CNN architecture is an evolving process. Therefore, we started with a simple classification task in two different CNNs and during the training process increased the complexity and variability of our application (see section 3.2.1). The resulting overall accuracy of 92% for the trained CNN-based on the GoogLeNet architecture presented here is already very high (we used this CNN to obtain all results). Further improvement would need more complex techniques such as K-Fold Cross-validation, a technique which optimally uses the training data (Stone, 1974). Such a near-100% accuracy arises because there are no sharp boundaries between the respective adjacent classes of RBC morphologies, i.e., the classes smoothly merge into each other. It is the confusion matrix (CM) that indicates the morphologies which the network has difficulties to differentiate between (examples: E1↔E2 or SE↔SP) (see Figure 25 and Figure 26). It is also not surprising that the CNN has differentiation problems typically with those classes, where manual differentiation is problematic as well.

We validated the excellent performance of the trained CNN further by comparing it to the formerly used decision tree classification (see Figure 27, (Sierra et al., 2017)). Considering the very different principles of classification when using a CNN compared to classification using a decision tree, it was somewhat surprising that the two methods agreed so well. While the decision tree algorithm requires the predefinition of binary categories (see above), the CNN performs this classification autonomously. Consistently with the two external studies (He et al., 2022; Pinto et al., 2019) that adapted and reproduced the formerly used decision tree (Sierra et al., 2017) and

applied it as a model for RBC classification, this high level of agreement demonstrates the quality of the dataset used in the decision tree-based classification. The close agreement is even more astonishing when one considers that the decision tree algorithm did not integrate a feature or class for stomatocyte morphologies. It is very likely that the decision tree classified a large amount of the stomatocytes morphologies into the discocyte class. This unintended pooling of stomatocyte morphologies and discocytes is entirely correct in terms of a lower classification resolution (see 3.3.1 and 4.2).

#### 4.2 Shear Induced Morphologies by Morphometric Measurements in Flow Chambers

The CNN-based classification enables the monitoring of characteristic morphological changes caused either by aging or by exterior stress. Until now, no other microfluidic analysis platform has been able to combine the monitoring of these two effects. Morphological changes are not necessarily related to biochemical changes but may be biased by the analytical method, especially influenced by the shear rate within the chamber. The velocity gradient in the flow and the shear rate generated through it has been shown to influence RBC morphology (Abkarian et al., 2008; Lanotte et al., 2016; Mauer et al., 2018; Reichel et al., 2019). Shear rates that affect the erythrocytes morphology are generated even in imaging flow cytometry (IFC), a technique known for its gentle cell handling. In IFCs, the shear is not generated in the hydrodynamic focusing section, where the actual measurement takes place, but microseconds before in the sample injection nozzle (for details see Supplementary Figure 2 and (Shapiro, 2003)).

In flow regimes with shear stress, stomatocyte morphologies have been detected as artefacts (see 1.4.1 and (Abkarian et al., 2008; Mauer et al., 2018; Reichel et al., 2019)). Indeed, our own results show that the proportion of stomatocytes is increased near the border surfaces of the laminar flow channel (Figure 28). Since the shear stress is maximal at positions closer to the channel surfaces, it can be concluded that the increase of stomatocyte proportion in these positions consists of formerly healthy discoid cells. These cells are only temporarily of stomatocyte morphology, after being deformed by the shear stress. However, the same results show that stomatocyte morphologies (T, DS and ST) are also present in the middle between the flow

chamber's surfaces (where the shear stress is zero), albeit at a much lower concentration. This implies that, in addition to the shear-induced stomatocytes, some of these stomatocyte morphologies are generated due to intrinsic degradation (Melzak et al., 2021).

The increased stomatocyte appearance close to the channel borders points out a general assumption with regard to any morphological RBC characterization which is based on laminar flow channels, including imaging flow cytometry. Specifically, if the respective measurement setup generates local shear stress above about 0.7 Pa directly at the point of measurement or shortly before, then shear-induced stomatocyte morphologies should be expected (Shapiro, 2003). Since this effect is only temporary, it would certainly complicate studies which aim at observing cell intrinsic morphological changes (see below 4.3). In contrast, there are some research groups that target exactly this temporary deformation of the cells as a physical measurement related to deformability (Guo et al., 2014; Otto et al., 2015). However, in these deformability measurements, the shear stress is three orders of magnitude higher (around 1 kPa, (Otto et al., 2015)) than the typical stress in the flow chamber of this study. As a result of this, a strong individual deformation of each cell is obtained. This unique deformational fingerprint can then be used to classify the RBCs in the different morphology classes.

If shear-induced morphologies or deformations are present in flow channels but cannot be used to assess the storage lesion signal, the question arises whether microfluidic measurements are still advantageous compared to manual light microscopic methods (blood smear), where such morphologies are not present. Flow channel measurements are indeed advantageous because the much higher statistics provided by microfluidic systems facilitates a very high sensitivity towards the measurement of subtle morphological effects. However, shear-induced morphology deformation may affect RBC morphology classification and should therefore be characterized and considered in any microfluidic setup. However, as we have shown in our setup and classification, the shear-induced stomatocyte morphologies are unlikely to affect the lesion index because it is caused exclusively by irreversible biochemical changes.

### 4.3 Prediction of Hemolysis Level Based on the Lesion Index

Several international guidelines, including the European guideline for use and quality assurance of blood components (European Directorate for the Quality of Medicines & HealthCare, 2020), determine the hemolysis level to be the decisive biochemical quality parameter for RCCs. If the hemolysis level in a RCC exceeds the official threshold of 0.8%, this RCC must be discarded. Our results presented here show that the lesion index correlates well with hemolysis level over storage time at an individual RCC level (see Figure 30). Therefore, there is strong evidence that the morphological lesion index can predict the level of hemolysis in RCCs during storage.

In the analyzed dataset B (see Table 3), the threshold level of 0.8% of hemolysis corresponds to a preliminary set threshold value of 11.1% of lesion index. With this threshold, the lesion index of a RCC reliably predicts whether a particular concentrate is of adequate quality in accordance with its hemolysis level. This updated morphological storage lesion marker generates a clearer corresponding threshold compared to the one based on the formerly used decision tree. However, the current numerical value for the threshold of the lesion index is only a preliminary estimate because its statistical basis is limited. In order to apply such a threshold as a compliance criterion for the quality of RCCs, the flow morphometry method used, including the trained CNN, has to be standardized (see below). Further clinical studies with independent datasets and appropriate statistics should be performed to be able to establish and confirm a final numerical threshold for the true prediction estimate of the lesion index with respect to the reference hemolysis.

In general, the correlation between the hemolysis level and the lesion index is comprehensible, because the SE and SP morphologies included in the lesion index represent the final morphological stages of erythrocyte degradation before cell lysis occurs. Further, the irreversibility of these spherical morphologies leads to a robust signal that is not disturbed by random variations due to reversible morphology changes (see below and 4.2). In spherical morphologies, the loss of the outer membrane surface area to the inner membrane has progressed so far that the cells can no longer revert to their original disc shape (Melzak et al., 2021). In the spherocytocyte stage, the larger membrane spicules are already irreversibly separated from the cells by vesiculation (Hess, 2016). For this reason, the further development of

spheroechinocytes (SE) will necessarily acquire a minimal surface area which necessarily requires a smooth spherical shape. These spheres are rigid since their minimal surface-to-volume ratio does not allow any other shape. From this point, there is no pathway back to the previous degradation morphologies.

RBCs in this morphological stage are close to lysis and therefore close to increasing the hemolysis level in RCCs. Nevertheless, the cells must pass through the stage of spherical morphologies before they lyse and thus before their lysis becomes evident by the increased hemolysis level. As a result of this, we expected that the lesion index can identify (and consequently predict) RCCs with poor quality slightly earlier than hemolysis. So far, our data (see Figure 30) does not include any information on the question whether the lesion index does precede the hemolysis level as a signal in time. To test this conjecture, more profound timing experiments will have to be carried out.

In contrast to spherical morphologies, all other individual RBC classes, including discocytes, undergo reversible transitions among themselves. These transitions are related to the process known as stomatocyte-discocyte-echinocyte sequence (SDE) (Sheetz & Singer, 1974), which involves interactions with shear and other temporal stress factors (Glaser & Donath, 1992; Glaser et al., 1987; Lanotte et al., 2016). The SDE sequence is based on the bilayer-couple hypothesis, which shows how the addition of different detergents can alter the morphology within the SDE sequence in a reversible way (Lim et al., 2002; Sheetz & Singer, 1974; Wong, 1999). This reversibility has been demonstrated experimentally for RBCs in E3 morphology stages back to discocytes by a washing step of the cells during storage (Lu & Shevkoplyas, 2020), as well as for trilobes back to discocytes by temporary shear stress (Lanotte et al., 2016). Such fluctuating influences result in a lower signal-to-noise ratio of the T, DS, D, ST, E1, E2, and E3 signals and the morphological index MI. The correlation of each of these signals with the hemolysis level is therefore weaker than that of the lesion index.

All in all, the results of this study indicate that the lesion index is indeed the most suitable and feasible quality parameter for RCCs.

#### 4.4 The Lesion Index as an Additional Storage Lesion Marker

The good correlation of the lesion index with the hemolysis facilitates a reliable prediction of the RBC's quality (as defined by hemolysis) by using its lesion index value. This is advantageous in two respects. First, the lesion index can be used to determine whether an RCC is still of sufficient quality as defined by the guidelines. Second, the measurement of the lesion index could replace the hemolysis measurement in the long term because it requires much fewer consumables and is less labor-intensive. The measurement of the lesion index itself requires only one dilution step of the sample with 0.9 % NaCl. In addition, by fully automating the system, a high throughput in combination with complete standardization of the measurement can be achieved. In contrast, the measurement of hemolysis involves several measurement methods and steps, such as centrifugation, accurate separation of the supernatant, and the subsequent measurement of Hkt, Hb, and free Hb. Conversely, a major disadvantage of hemolysis measurement is a lack of standardization, as there are different methods of hemoglobin measurement (Janatpour et al., 2004). Historically, due to a lack of alternatives and despite these disadvantages, hemolysis has established itself as the gold standard of RBC quality assessment.

Based on our data, we would like to suggest that the lesion index could indeed be included in clinical routines as an additional marker for RBC storage lesion, given that, in contrast to hemolysis, the lesion index is a good indicator of the post-transfusion survival rate of RBCs (Roussel et al., 2021). This is defined as the percentage of transfused cells which still circulate in the patient 24 hours after transfusion (Roussel et al., 2017). The post-transfusion survival rate, along with hemolysis, is one of the two metrics recommended by the FDA to measure in order to provide a good indication of the quality of RCCs (FDA, 1986). A post-transfusion survival rate of at least 75% is recommended. However, because the measurement is very complex, it is mainly used to validated new storage systems (D'Alessandro et al., 2010). The standard measurement for post-transfusion survival is the Chromium-51 labeling method. Thereby, 15-30 mL of labeled RBCs with  $^{51}\text{Cr}$  are injected to the recipient and the RBC recovery is quantified after transfusion by taking blood samples at different measurement points. The radioactive RBCs are then counted in each taken sample and extrapolated by linear regression (Roussel et al., 2018). In contrast to hemolysis, which is intended to provide information about the percentage of cells within an RCC

that are already lysed, the post-transfusion survival rate provides additional information about the state of the cells that are still alive in the RCCs.

It has already been shown that the proportion of spherical morphologies strongly correlates with post-transfusion survival (Roussel et al., 2021). A high proportion of spherical morphologies leads to lower post-transfusion recovery, which is mainly due to the elimination of spherical morphologies in the body. Spherical morphologies are mainly degraded by macrophages in the spleen and liver. Therefore, the quantification of spherical morphologies could improve the evaluation of blood product quality (Pinto et al., 2019; Roussel et al., 2021). The lesion index, which is composed exclusively of these spherical morphologies, may thus provide additional information on post-transfusion cell survival in addition to hemolysis rate. Thus, both measurements together would generally ensure increased safety and efficacy of RCCs. This increased safety has long been called for (D'Alessandro et al., 2010; Garcia-Roa et al., 2017; Roussel et al., 2017), but until now there has been no suitable measurement system that could easily provide a reliable marker of post-transfusion survival in RCC quality control. The next step would be to carry out a clinical study comparing lesion index of RCCs before transfusion and actual post-transfusion recovery rates of RBCs after the recipient received the transfusion.

#### 4.5 The Standardization of Flow Morphometry for the Measurement of Storage Lesion

To ensure consistent long-term measurements of the lesion index as well as its reproducibility between different laboratories, it is important to standardize and automate it. We have already implemented some standardization measures within the scope of the air rescue mission study (see sections 2.5.3 and 3.1). For example, in the sample preparation, we defined that all samples are diluted at least 10 minutes before measurement. This time allows the cells to adapt to the diluted environment (osmotic stress). In addition, only large pipette tips were used for pipetting (smallest tip 200  $\mu$ L), as these have relatively large tip openings so that less shear stress occurs. To fill the tubing and the flow chamber with the cell suspension, the sample was introduced by manually operating the syringe pump at maximum pumping power. During this process, the cells experience increased shear stress. This is especially true for the

cells which are already in the flow chamber, since the small diameter of the flow chamber leads to higher shear stress. To prevent the transient and reversible shear-induced morphologies from being incorporated into the data, the actual measurement was not started until 20 seconds after the correct volume flow rate has been set in the regularly filled system. This problem of raised shear during the initial introduction of the RBC suspension is common to any microfluidic system.

The standardization requires also an adjustment of the position of the focal plane in the flow chamber. So far, this adjustment has to be performed manually and is therefore associated with a certain bias between different measurements (readjustment). We minimized this bias by stiffening of the flow chamber mounting, thanks to which the need of readjustment during a measurement series was eliminated. However, a future way of adjusting the height of the focal plane automatically is to incorporate a piezoelectric stage into the system. This requires the development of an autofocus algorithm along with a custom interface that could be controlled from the PC.

In future developments, the problem of reproducibility regarding the focus adjustment within the flow channel could be alleviated by using an adjustment-free imaging system, as presented by Herkommer and Suhr (Suhr & Herkommer, 2015). Instead of a flow chamber, an agitated cuvette would be used which is simpler to operate than a microfluidic system but does not facilitate the rolling mode motion.

#### 4.6 Non-Inferiority of RCC Quality after Repeated Air Rescue Missions under Specific Regulations of a Rotation System

Having established a system for assessment of RBC morphologies, that is highly sensitive and easy to run yielding robust statistical data, we aimed to translate it into a quality control setting and applied it in the so called “Heli-Blood” project to assess RCCs before and after repeated air rescue mission transport.

In order to establish empirical knowledge about safe storage and transport logistics for RCCs in air rescue missions, i) a rotation system for repeated air rescue missions of RCCs in compliance with regulations was established and ii) the non-inferior quality of RCCs after repeated air rescue transport was verified.

To comply with regulatory conditions for transport and storage, Dr. Sitzmann and colleagues from the Red Cross Blood Donor Service Institute Mannheim adapted a system initiated in Greifswald (Selleng, 2020). She accomplished optimized transport and storage logistics by introducing a rotation system which relied on a passive cooling box (Klose et al., 2010; Rentas et al., 2004). This ensured the maintenance of the specified temperature throughout the whole process.

From the total sample size of 131 RCCs, the number of 30 prehospitally transfused RCCs is large, considering that 50 RCCs were used as the control. The prehospital transfusion helped to save the lives of 9 patients with various severe injuries; a more detailed view on these patients' outcomes can be found in (Rudolph et al., 2021). The remaining RCCs were analyzed in detail. The results of the detailed analysis showed that the quality of RCCs after repeated helicopter transport was non-inferior to control samples during storage for up to 42 days.

Concerning the hemolysis level, the statistical analysis revealed no difference between the flight and control group with a very high p-value. The average increase of hemolysis for the flight (0.18%) and control (0.18%) groups fell within the limits (0.55%) of regular hemolysis increase after 42 days of storage through the normal aging process of RCCs (Makroo et al., 2011).

However, as has already been mentioned in sections 1.2 and 1.4, there is growing concern that more parameters should be considered to ensure the safety and efficacy of stored RBCs quality (D'Alessandro et al., 2010; Garcia-Roa et al., 2017; Glynn et al., 2016; Roussel et al., 2017). Therefore, the MCV, potassium and pH were included, all of which are closely related to storage lesion (D'Alessandro et al., 2010; Hess, 2010; Roussel et al., 2017). In order to enhance the information about the RCCs' quality, in particular with respect to their expected post-transfusion recovery, the newly developed lesion index was also included in this study. In the case of the lesion index, it was possible to generate an additional net change measurement to the end-point measurements. This net change of the lesion index represents a difference measurement of the degradation effect.

Neither the lesion index itself nor its net change revealed any quality difference between the flight group and the control group.

Despite the large variety of different performed measurements, the statistical analysis of all measured data showed no difference between the flight group and the control

group. The data do not give any reason to reject the null hypothesis that the statistical distributions of data in both groups are identical. It can be concluded that any conceivable residual differences between the RCCs used in flight and the RCCs which are permanently stored are very small and therefore clinically irrelevant. These findings agree with the result of closely related studies, which also investigated the influence of helicopter transport on the quality of RBCs (Bjerkvig et al., 2020; Brade et al., 2020; Selleng, 2020).

The number of helicopter-missions of individual RCCs during this study varied from 7 to 13 times. The total duration of flight time which the RCCs experienced varied from 6.6 to 28.8 hours. Despite these large ranges, neither the biochemical parameters nor the morphological parameters showed any correlation with the flight time. The null hypothesis of no correlation (i.e., in which the linear regression coefficient is smaller than 0.5 and the p-value for the slope of linear regression line equals zero) between any of the measured parameters and the flight time must be accepted. This agrees with the direct comparison results between flight and control samples from above, since correlation to the flight time should have shown at least a small alteration effect between the two sample groups.

We believe that four factors having the biggest impact on the RCCs during the helicopter transport: i) the temperature, ii) the repeated packing process, iii) the helicopter vibration and iv) the air pressure of the flight height.

Ad i: Temperature monitoring is an essential part of quality control in transfusion medicine, as increased or decreased temperature may compromise the product quality (Blaine et al., 2019; Brunskill et al., 2012; Nilsson et al., 1983). Therefore, the packing process was optimized with respect to thermal stability. As a result, only 4 out of 131 RBC units were excluded from this study because of temperature deviation exceeding the limits +2°C to +6°C. This remains well within the limit of RBC storage temperatures according to the German Guidelines (Bundesärztekammer, 2020).

Ad ii: The temperature control has a large impact on how the RCCs have to be handled in the storage process and also in the repeated packing process. Although this makes the packing process more complicated (see packing procedure in section 2.5.1), our results justify the extra effort.

Ad iii: Whether the vibration of the helicopter is a factor that is of positive or negative relevance or whether it is relevant at all is unclear (Bjerkvig et al., 2020; Boecker et al.,

2022; Brade et al., 2020). RBCs have evolved to become capable of being squeezed and pushed through the vascular system. The type of mechanical stress encountered in this process is far greater than the moderate stress caused by the vibration of the helicopter. Furthermore, it is not impossible that the vibration of the helicopter leads to a more homogeneous mixing of the transported RCCs, which could have a beneficial effect on the RCC quality.

Ad iv: A further influence on the flight RCCs is given by the change in air pressure during different flight heights. Almanza et al. (Almanza et al., 1995) investigated the effect of pressure changes on RCCs during long-distance flights with flight heights of 2000 m. They could show that pressure changes at 2000 m have a significant influence on the RCCs' quality (Almanza et al., 1995). However, the flight altitudes of the air rescue service in our study are about 300 m. Our results show that the pressure changes at these altitudes are without clinical relevance on the RCCs. Nevertheless, before applying a flight regime like the one presented here in mountainous regions, an additional study should be conducted in such regions where the absolute altitude and the changes in altitude during flights are much greater.

#### 4.7 Outlook

Given that flow morphometry combined with CNN image processing proved to be a powerful and very flexible system, we now aim to transfer it to a diagnosis platform and to create a spin-off. The next steps for the lesion index application are a larger clinical study regarding the true threshold for RCC quality control and a comparison study with the standard for post-transfusion recovery measurements. However, with the helicopter study we could show that the technique is already on a technology readiness level (TRL) of 6-7. To develop the system towards a TRL level of 9 (use in routine diagnostics), there are certain steps to be implemented. First, the system has to be automated: automated sample injection and cleaning steps. Second, the analysis software has to be implemented in the system: ideally, sample measurement and image analysis can be conducted and monitored in one program.

To expand the diagnosis platform, further applications for blood diseases such as sickle cell anemia and thalassemia are planned. In all future applications high TRL

levels are necessary to make a successful transition of our technology from laboratory to routine application in the industry.

## 5 SUMMARY

Red blood cell transfusion is routinely performed to improve tissue oxygenation in patients with decreased hemoglobin levels and oxygen-carrying capacity. Generally, blood banks process and store packed red blood cells as RCCs. During storage, RBCs undergo progressive biochemical and morphological changes which are collectively described as storage lesion. According to regulatory guidelines, the quality of RCCs is assessed by quantifying hemolysis before transfusion. However, the hemolysis level only gives an indication of the already lysed erythrocytes; it does not indicate the degree of deterioration of aged cells, which are known to compromise the post-transfusion survival. Morphological analysis, a method that has the potential to provide a simple and practical diagnosis, is suitable for indicating the degradation of RBCs and thus has considerable power to predict actual post-transfusion survival.

Microfluidic systems with suspended RBCs can enable fully automated morphological diagnosis based on image analysis with large cell statistics and high sample throughput. The previous version of the flow morphometry system, which was based on a binary decision tree was able to show in a first attempt that spherocytes are a suitable candidate for such a morphological storage lesion marker. However, due to the low classification resolution (three morphology classes), possible shear-induced morphology changes of the measurement system could not be evaluated.

In this study, the image classification of the flow morphometry system was substantially enhanced by using a convolutional neural network to strongly improve the resolution and accuracy of the morphology classification. The resulting CNN-based classification achieved a high overall accuracy of 92% with RBCs being classified into nine morphology classes. Through this improved classification resolution, it was possible to assess degradation-induced morphologies at high resolution simultaneously with shear-induced morphologies in RCCs. The overall goal was to provide a robust and strong marker for storage lesion that reflects post-transfusion survival of RBCs. Therefore, it was necessary to analyze the extent to which the shear in the microfluidic system affected the morphological transients between RBC classes.

Indeed, it could be shown that shear-induced morphology changes appear dependent on the position of the focal plane height in the flow chamber. The proportion of stomatocytes is increased near the surfaces of the laminar flow chamber. This temporary shear-induced morphology transformation can occur only in flexible

erythrocytes with intact membrane properties. Therefore, these cells should be considered a subset of healthy erythrocytes that can reversibly alter from stomatocyte to discocyte morphology.

The nine RBC morphology classes of the improved classification resolution were further analyzed to determine whether they exhibit a particular pattern based on their relative proportions during storage that could be used as a storage lesion marker. All individual RBC classes, except for the spherical morphologies, undergo reversible transitions among themselves that are related to the SDE sequence and result in a low signal-to-noise ratio. The proportions of the irreversible spherical morphologies, spherocytocytes and spherocytes, were defined as the lesion index. This lesion index showed a strong correlation to hemolysis levels. In fact, the correlation between the hemolysis level and the lesion index was so good that it persisted at an individual RCC level. A preliminary lesion index threshold of 11.1% could be established, which is equivalent to a hemolysis threshold of 0.8% established in regulatory guidelines, to assess whether an RCC is of appropriate quality for transfusion. However, the lesion index, besides predicting the hemolysis level, can also be used to generate more information about post-transfusion survival, since it consists exclusively of the RBC morphologies that are removed by the body in a very short time after transfusion in the recipient.

Finally, we translated the newly established lesion index and standard biochemical parameters into a quality assessment of RCC shipped and transported repeatedly on air rescue missions to assess an eventual deterioration of the RBCs. We showed that the quality of RCCs was not inferior to control samples after repeated air rescue missions during storage. German regulations allow RCCs to be stored for 42 days in a temperature range of +2°C to +6°C. Compliance with this regulation can be secured during air rescue missions by means of suitable logistics based on a rotation system. By using efficient cooling devices, the logistics and maintenance of the thermal conditions are both safe and feasible. A well-defined rotation system for the use of RCCs during routine air rescue missions offers a resource-saving option and enables the provision of RCCs in compliance with German transfusion guidelines. This innovative concept enables life-saving prehospital transfusions directly at the incident scene.

CNN-based flow morphometry and the calculated lesion index allow a reliable assessment of RCC quality. The method also decreases the demand for complex laboratory procedures. Therefore, it is highly advisable to include the lesion index as an additional marker for storage lesion in routine clinical practice. Unlike hemolysis, the lesion index may serve as a good indicator of post-transfusion survival. Thus, both measurements together could provide increased safety and efficacy of stored RCCs.

## 6 REFERENCES

- Abkarian, M., Faivre, M., Horton, R., Smistrup, K., Best-Popescu, C. A., & Stone, H. A. (2008, Sep). Cellular-scale hydrodynamics. *Biomed Mater*, 3(3), 034011. <https://doi.org/10.1088/1748-6041/3/3/034011>
- Acker, J. P., Hansen, A. L., Kurach, J. D., Turner, T. R., Croteau, I., & Jenkins, C. (2014, Oct). A quality monitoring program for red blood cell components: in vitro quality indicators before and after implementation of semiautomated processing. *Transfusion*, 54(10), 2534-2543.
- Almanza, L., Lataillade, J. J., Almanza, B. A., Pats, B., & Joussemet, M. (1995). Erythrocyte concentrated and air transport: evaluation of quality. *Transfus Clin Biol*, 2(5), 343-347. [https://doi.org/10.1016/s1246-7820\(05\)80077-1](https://doi.org/10.1016/s1246-7820(05)80077-1) (Concentres érythrocytaires et transport arien: evaluation de la qualite.)
- Almizraq, R., Tchir, J. D., Holovati, J. L., & Acker, J. P. (2013, Oct). Storage of red blood cells affects membrane composition, microvesiculation, and in vitro quality. *Transfusion*, 53(10), 2258-2267. <https://doi.org/10.1111/trf.12080>
- Arduini, A., Minetti, G., Ciana, A., Seppi, C., Brovelli, A., Profumo, A., Vercellati, C., Zappa, M., Zanella, A., Dottori, S., & Bonomini, M. (2007, Jan). Cellular properties of human erythrocytes preserved in saline-adenine-glucose-mannitol in the presence of L-carnitine. *Am J Hematol*, 82(1), 31-40. <https://doi.org/10.1002/ajh.20753>
- Asanza, D. F. (2009). Entwicklung eines Frameworks für On-Line Bildanalyse für das In-Situ Mikroskop. *Hochschule Mannheim*.
- Ash, T. (1989, 1989/01/01). Dynamic Node Creation in Backpropagation Networks. *Connection Science*, 1(4), 365-375. <https://doi.org/10.1080/09540098908915647>
- Aubron, C., Nichol, A., Cooper, D. J., & Bellomo, R. (2013, Jan 15). Age of red blood cells and transfusion in critically ill patients. *Ann Intensive Care*, 3(1), 2. <https://doi.org/10.1186/2110-5820-3-2>
- Arbeitsgemeinschaft der Wissenschaftlichen Medizinischen Fachgesellschaften (AWMF) – Ständige Kommission Leitlinien. AWMF-Regelwerk „Leitlinien“. 1. Auflage 2012. Verfügbar: <http://www.awmf.org/leitlinien/awmf-regelwerk.html> (Zugriff am 19.07.2021), (2012).
- Batchelor, G. K. (1967). *An Introduction to Fluid Dynamics*. Cambridge University Press.
- Berezina, T. L., Zaets, S. B., & Machiedo, G. W. (2004, Jul). Alterations of red blood cell shape in patients with severe trauma. *J Trauma*, 57(1), 82-87. <https://doi.org/10.1097/01.ta.0000135492.24111.24>
- Bessis, M. (1972). Red cell shapes. An illustrated classification and its rationale. *Nouvelle revue francaise d'hematologie*, 12(6), 721-745.
- Bishop, C. M., & Nasrabadi, N. M. (2006). *Pattern recognition and machine learning* (Vol. 4). Springer.
- Bjerkvig, C., Sivertsen, J., Braathen, H., Lunde, T. H. F., Strandenes, G., Assmus, J., Hervig, T., Cap, A., Kristoffersen, E. K., Fosse, T., & Apelseh, T. O. (2020, Jul). Cold-stored whole blood in a Norwegian emergency helicopter service: an observational study on storage conditions and product quality. *Transfusion*, 60(7), 1544-1551. <https://doi.org/10.1111/trf.15802>
- Blaine, K. P., Cortes-Puch, I., Sun, J., Wang, D., Solomon, S. B., Feng, J., Gladwin, M. T., Kim-Shapiro, D. B., Basu, S., Perlegas, A., West, K., Klein, H. G., & Natanson, C. (2019, Jan). Impact of different standard red blood cell storage temperatures on human

- and canine RBC hemolysis and chromium survival. *Transfusion*, 59(1), 347-358. <https://doi.org/10.1111/trf.14997>
- Blasi, B., D'Alessandro, A., Ramundo, N., & Zolla, L. (2012, Apr). Red blood cell storage and cell morphology. *Transfus Med*, 22(2), 90-96. <https://doi.org/10.1111/j.1365-3148.2012.01139.x>
- Boecker, C. (2018). Flow Cytomorphometry for Assessment of Red Blood Cells. *Hochschule Mannheim*.
- Boecker, C., Sitzmann, N., Halblaub Miranda, J. L., Suhr, H., Wiedemann, P., Bieback, K., Rudolph, M., & Klüter, H. (2022). Noninferior Red Cell Concentrate Quality after Repeated Air Rescue Mission Transport for Prehospital Transfusion. *Transfusion Medicine and Hemotherapy*, 49(3), 172-179. <https://doi.org/10.1159/000520650>
- Bosman, G. J., Lasonder, E., Lutén, M., Roerdinkholder-Stoelwinder, B., Novotny, V. M., Bos, H., & De Grip, W. J. (2008, May). The proteome of red cell membranes and vesicles during storage in blood bank conditions. *Transfusion*, 48(5), 827-835. <https://doi.org/10.1111/j.1537-2995.2007.01630.x>
- Brade, M., Dahmen, J., Zeiger, S., Ohmann, T., Figner, C., Unnerstall, B., Zeiler, T., & Suck, G. (2020). Auswirkung von Hubschraubertransporten auf die Hämolyserate von Erythrozytenkonzentraten bei deren Einsatz in der Luftrettung. *Notarzt*, 36, 151- 159.
- Brown, J. B., Cohen, M. J., Minei, J. P., Maier, R. V., West, M. A., Billiar, T. R., Peitzman, A. B., Moore, E. E., Cuschieri, J., Sperry, J. L., Inflammation, & the Host Response to Injury, I. (2015, May). Pretrauma center red blood cell transfusion is associated with reduced mortality and coagulopathy in severely injured patients with blunt trauma. *Ann Surg*, 261(5), 997-1005. <https://doi.org/10.1097/SLA.0000000000000674>
- Brown, J. B., Sperry, J. L., Fombona, A., Billiar, T. R., Peitzman, A. B., & Guyette, F. X. (2015, May). Pre-trauma center red blood cell transfusion is associated with improved early outcomes in air medical trauma patients. *J Am Coll Surg*, 220(5), 797-808. <https://doi.org/10.1016/j.jamcollsurg.2015.01.006>
- Brunskill, S., Thomas, S., Whitmore, E., McDonald, C. P., Doree, C., Hopewell, S., Staves, J., Cardigan, R., & Murphy, M. F. (2012, Jul). What is the maximum time that a unit of red blood cells can be safely left out of controlled temperature storage? *Transfus Med Rev*, 26(3), 209-223 e203. <https://doi.org/10.1016/j.tmr.2011.09.005>
- Bundesärztekammer. (2017). Richtlinie zur Gewinnung von Blut und Blutbestandteilen und zur Anwendung von Blutprodukten (Richtlinie Hämotherapie) gemäß §§ 12a und 18 des Transfusionsgesetzes (TFG).
- Bundesärztekammer. (2020). Querschnitts-Leitlinien (BÄK) zur Therapie mit Blutkomponenten und Plasmaderivaten.
- Cancelas, J. A., Dumont, L. J., Maes, L. A., Rugg, N., Herschel, L., Whitley, P. H., Szczepiokowski, Z. M., Siegel, A. H., Hess, J. R., & Zia, M. (2015, Mar). Additive solution-7 reduces the red blood cell cold storage lesion. *Transfusion*, 55(3), 491-498. <https://doi.org/10.1111/trf.12867>
- Card, R. T. (1988, Mar). Red cell membrane changes during storage. *Transfus Med Rev*, 2(1), 40-47. [https://doi.org/10.1016/s0887-7963\(88\)70030-9](https://doi.org/10.1016/s0887-7963(88)70030-9)
- Cardo, L. J., Wilder, D., & Salata, J. (2008, Apr). Neutrophil priming, caused by cell membranes and microvesicles in packed red blood cell units, is abrogated by leukocyte depletion at collection. *Transfus Apher Sci*, 38(2), 117-125. <https://doi.org/10.1016/j.transci.2008.01.004>
- Carson, J. L., Grossman, B. J., Kleinman, S., Tinmouth, A. T., Marques, M. B., Fung, M. K., Holcomb, J. B., Illloh, O., Kaplan, L. J., Katz, L. M., Rao, S. V., Roback, J. D., Shander, A., Tobian, A. A., Weinstein, R., Swinton McLaughlin, L. G., Djulbegovic, B., & Clinical

- Transfusion Medicine Committee of the, A. (2012, Jul 3). Red blood cell transfusion: a clinical practice guideline from the AABB\*. *Ann Intern Med*, 157(1), 49-58. <https://doi.org/10.7326/0003-4819-157-1-201206190-00429>
- Carson, J. L., Guyatt, G., Heddle, N. M., Grossman, B. J., Cohn, C. S., Fung, M. K., Gernsheimer, T., Holcomb, J. B., Kaplan, L. J., Katz, L. M., Peterson, N., Ramsey, G., Rao, S. V., Roback, J. D., Shander, A., & Tobian, A. A. (2016, Nov 15). Clinical Practice Guidelines From the AABB: Red Blood Cell Transfusion Thresholds and Storage. *JAMA*, 316(19), 2025-2035. <https://doi.org/10.1001/jama.2016.9185>
- D'Alessandro, A., Liumbruno, G., Grazzini, G., & Zolla, L. (2010, Apr). Red blood cell storage: the story so far. *Blood Transfus*, 8(2), 82-88. <https://doi.org/10.2450/2009.0122-09>
- D'Amici, G. M., Rinalducci, S., & Zolla, L. (2007, Aug). Proteomic analysis of RBC membrane protein degradation during blood storage. *J Proteome Res*, 6(8), 3242-3255. <https://doi.org/10.1021/pr070179d>
- Dean, L. (2005). *Blood groups and red cell antigens*. NCBI.
- Deplaine, G., Safeukui, I., Jeddi, F., Lacoste, F., Brousse, V., Perrot, S., Biligui, S., Guillotte, M., Guitton, C., Dokmak, S., Aussilhou, B., Sauvanet, A., Cazals Hatem, D., Paye, F., Thellier, M., Mazier, D., Milon, G., Mohandas, N., Mercereau-Puijalon, O., David, P. H., & Buffet, P. A. (2011, Feb 24). The sensing of poorly deformable red blood cells by the human spleen can be mimicked in vitro. *Blood*, 117(8), e88-95. <https://doi.org/10.1182/blood-2010-10-312801>
- Dhabangi, A., Ainomugisha, B., Cserti-Gazdewich, C., Ddungu, H., Kyeyune, D., Musisi, E., Opoka, R., Stowell, C. P., & Dzik, W. H. (2015, Dec 15). Effect of Transfusion of Red Blood Cells With Longer vs Shorter Storage Duration on Elevated Blood Lactate Levels in Children With Severe Anemia: The TOTAL Randomized Clinical Trial. *JAMA*, 314(23), 2514-2523. <https://doi.org/10.1001/jama.2015.13977>
- Doan, M., Sebastian, J. A., Caicedo, J. C., Siegert, S., Roch, A., Turner, T. R., Mykhailova, O., Pinto, R. N., McQuin, C., Goodman, A., Parsons, M. J., Wolkenhauer, O., Hennig, H., Singh, S., Wilson, A., Acker, J. P., Rees, P., Kolios, M. C., & Carpenter, A. E. (2020, Sep 1). Objective assessment of stored blood quality by deep learning. *Proc Natl Acad Sci U S A*, 117(35), 21381-21390. <https://doi.org/10.1073/pnas.2001227117>
- Dupire, J., Socol, M., & Viallat, A. (2012, Dec 18). Full dynamics of a red blood cell in shear flow. *Proc Natl Acad Sci U S A*, 109(51), 20808-20813. <https://doi.org/10.1073/pnas.1210236109>
- Eibl, R., Eibl, D., Pörtner, R., & al., e. (2009). *Cell and Tissue Reaction Engineering*. Springer.
- European Directorate for the Quality of Medicines & HealthCare. (2020). Guide to the preparation, use and quality assurance of blood components. *EDQM, 20th* 200-200.
- FDA. (1986). FDA summary basis of approval for red blood cells frozen and red blood cells deglycerolized. (Reference number 86-0335). US License Number 635-10. Applicant-Department of the Navy, Navy Hospital, Bethesda, MD.
- Fergusson, D. A., Hebert, P., Hogan, D. L., LeBel, L., Rouvinez-Bouali, N., Smyth, J. A., Sankaran, K., Tinmouth, A., Blajchman, M. A., Kovacs, L., Lachance, C., Lee, S., Walker, C. R., Hutton, B., Ducharme, R., Balchin, K., Ramsay, T., Ford, J. C., Kakadekar, A., Ramesh, K., & Shapiro, S. (2012, Oct 10). Effect of fresh red blood cell transfusions on clinical outcomes in premature, very low-birth-weight infants: the ARIPI randomized trial. *JAMA*, 308(14), 1443-1451. <https://doi.org/10.1001/2012.jama.11953>
- Garcia-Roa, M., Del Carmen Vicente-Ayuso, M., Bobes, A. M., Pedraza, A. C., Gonzalez-Fernandez, A., Martin, M. P., Saez, I., Seghatchian, J., & Gutierrez, L. (2017, May). Red blood cell storage time and transfusion: current practice, concerns and future perspectives. *Blood Transfus*, 15(3), 222-231. <https://doi.org/10.2450/2017.0345-16>

- Glaser, R., & Donath, J. (1992). Temperature and transmembrane potential dependence of shape transformations of human erythrocytes. *Journal of Electroanalytical Chemistry*, 342(3), 429-440.
- Glaser, R., Fujii, T., Müller, P., Tamura, E., & Herrmann, A. (1987). Erythrocyte shape dynamics: influence of electrolyte conditions and membrane potential. *Biomedica Biochimica Acta*, 46(2-3), S327-333.
- Glynn, S. A., Klein, H. G., & Ness, P. M. (2016, Jun). The red blood cell storage lesion: the end of the beginning. *Transfusion*, 56(6), 1462-1468. <https://doi.org/10.1111/trf.13609>
- Greenspan, H., Ginneken, B. v., & Summers, R. M. (2016). Guest Editorial Deep Learning in Medical Imaging: Overview and Future Promise of an Exciting New Technique. *IEEE Transactions on Medical Imaging*, 35(5), 1153-1159. <https://doi.org/10.1109/TMI.2016.2553401>
- Griggs, J. E., Jeyanathan, J., Joy, M., Russell, M. Q., Durge, N., Bootland, D., Dunn, S., Sausmarez, E. D., Wareham, G., Weaver, A., Lyon, R. M., Kent, S., & Sussex Air Ambulance, T. (2018, Nov 20). Mortality of civilian patients with suspected traumatic haemorrhage receiving pre-hospital transfusion of packed red blood cells compared to pre-hospital crystalloid. *Scand J Trauma Resusc Emerg Med*, 26(1), 100. <https://doi.org/10.1186/s13049-018-0567-1>
- Guo, Q., Duffy, S. P., Matthews, K., Santoso, A. T., Scott, M. D., & Ma, H. (2014). Microfluidic analysis of red blood cell deformability. *Journal of biomechanics*, 47(8), 1767-1776.
- Halblaub, J. L. (2019). Deep Neuronal Networks for the Assessment of Stored Red Blood Cells Degradation Stages. *University of Ulm*.
- Hamasaki, N., & Yamamoto, M. (2000). Red blood cell function and blood storage. *Vox Sang*, 79(4), 191-197. <https://doi.org/10.1159/000056729>
- Han, V., Serrano, K., & Devine, D. V. (2010, Feb). A comparative study of common techniques used to measure haemolysis in stored red cell concentrates. *Vox Sang*, 98(2), 116-123. <https://doi.org/10.1111/j.1423-0410.2009.01249.x>
- Hastie, T., Tibshirani, R., Friedman, J. H., & Friedman, J. H. (2009). *The elements of statistical learning: data mining, inference, and prediction* (Vol. 2). Springer.
- He, K., Zhang, X., Ren, S., & Sun, J. (2016). Deep residual learning for image recognition. Proceedings of the IEEE conference on computer vision and pattern recognition,
- He, L., Shao, M., Yang, X., Si, L., Jiang, M., Wang, T., Ke, Z., Peng, T., Fang, S., Zhang, S., Ouyang, X., Zhao, G., & Zhou, J. (2022, Mar 3). Morphology analysis of unlabeled red blood cells based on quantitative differential phase contrast microscopy. *Cytometry A*. <https://doi.org/10.1002/cyto.a.24546>
- Heaton, W. A., Holme, S., Smith, K., Brecher, M. E., Pineda, A., AuBuchon, J. P., & Nelson, E. (1994, Jun). Effects of 3-5 log<sub>10</sub> pre-storage leucocyte depletion on red cell storage and metabolism. *Br J Haematol*, 87(2), 363-368. <https://doi.org/10.1111/j.1365-2141.1994.tb04923.x>
- Hebert, P. C., Wells, G., Blajchman, M. A., Marshall, J., Martin, C., Pagliarello, G., Tweeddale, M., Schweitzer, I., & Yetisir, E. (1999, Feb 11). A multicenter, randomized, controlled clinical trial of transfusion requirements in critical care. Transfusion Requirements in Critical Care Investigators, Canadian Critical Care Trials Group. *N Engl J Med*, 340(6), 409-417. <https://doi.org/10.1056/NEJM199902113400601>
- Heddle, N. M., Cook, R. J., Arnold, D. M., Liu, Y., Barty, R., Crowther, M. A., Devereaux, P. J., Hirsh, J., Warkentin, T. E., Webert, K. E., Roxby, D., Sobieraj-Teague, M., Kurz, A., Sessler, D. I., Figueroa, P., Ellis, M., & Eikelboom, J. W. (2016, Nov 17). Effect of Short-Term vs. Long-Term Blood Storage on Mortality after Transfusion. *N Engl J Med*, 375(20), 1937-1945. <https://doi.org/10.1056/NEJMoa1609014>

- Hess, J. R. (2006, Jul). An update on solutions for red cell storage. *Vox Sang*, 91(1), 13-19. <https://doi.org/10.1111/j.1423-0410.2006.00778.x>
- Hess, J. R. (2010, Aug). Red cell changes during storage. *Transfus Apher Sci*, 43(1), 51-59. <https://doi.org/10.1016/j.transci.2010.05.009>
- Hess, J. R., Sparrow, R. L., van der Meer, P. F., Acker, J. P., Cardigan, R. A., & Devine, D. V. (2009, Dec). Red blood cell hemolysis during blood bank storage: using national quality management data to answer basic scientific questions. *Transfusion*, 49(12), 2599-2603. <https://doi.org/10.1111/j.1537-2995.2009.02275.x>
- Hess, J. R. S., B.G. (2016). Red blood cell metabolism, preservation, and oxygen delivery. In T. L. M. Simon, J.; Snyder, E.L.; Solheim, B.G.; Trauss, R.G.S. (Ed.), *Rossi's Principles of Transfusion Medicine* (pp. 97-109). John Wiley & Sons. <https://doi.org/10.1002/9781119013020.ch09>
- Hod, E. A., Brittenham, G. M., Billote, G. B., Francis, R. O., Ginzburg, Y. Z., Hendrickson, J. E., Jhang, J., Schwartz, J., Sharma, S., Sheth, S., Sireci, A. N., Stephens, H. L., Stotler, B. A., Wojczyk, B. S., Zimring, J. C., & Spitalnik, S. L. (2011, Dec 15). Transfusion of human volunteers with older, stored red blood cells produces extravascular hemolysis and circulating non-transferrin-bound iron. *Blood*, 118(25), 6675-6682. <https://doi.org/10.1182/blood-2011-08-371849>
- Hod, E. A., & Spitalnik, S. L. (2011, Apr). Harmful effects of transfusion of older stored red blood cells: iron and inflammation. *Transfusion*, 51(4), 881-885. <https://doi.org/10.1111/j.1537-2995.2011.03096.x>
- Hoffbrand, A. V., Pettit, J.E., Moss, P.A., Hoelzer, D. (2002). *Grundkurs Hämatologie* (2nd. Ed. ed.). Thieme.
- Hogman, C. F., de Verdier, C. H., Ericson, A., Hedlund, K., & Sandhagen, B. (1985). Studies on the mechanism of human red cell loss of viability during storage at +4 degrees C in vitro. I. Cell shape and total adenylate concentration as determinant factors for posttransfusion survival. *Vox Sang*, 48(5), 257-268. <https://doi.org/10.1111/j.1423-0410.1985.tb00181.x>
- Holcomb, J. B., Tilley, B. C., Baraniuk, S., Fox, E. E., Wade, C. E., Podbielski, J. M., del Junco, D. J., Brasel, K. J., Bulger, E. M., Callcut, R. A., Cohen, M. J., Cotton, B. A., Fabian, T. C., Inaba, K., Kerby, J. D., Muskat, P., O'Keefe, T., Rizoli, S., Robinson, B. R., Scalea, T. M., Schreiber, M. A., Stein, D. M., Weinberg, J. A., Callum, J. L., Hess, J. R., Matijevic, N., Miller, C. N., Pittet, J. F., Hoyt, D. B., Pearson, G. D., Leroux, B., van Belle, G., & Group, P. S. (2015, Feb 3). Transfusion of plasma, platelets, and red blood cells in a 1:1:1 vs a 1:1:2 ratio and mortality in patients with severe trauma: the PROPPR randomized clinical trial. *JAMA*, 313(5), 471-482. <https://doi.org/10.1001/jama.2015.12>
- Janatpour, K. A., Paglieroni, T. G., Crocker, V. L., DuBois, D. J., & Holland, P. V. (2004, Jul). Visual assessment of hemolysis in red blood cell units and segments can be deceptive. *Transfusion*, 44(7), 984-989. <https://doi.org/10.1111/j.1537-2995.2004.03315.x>
- Karl, A., Pham, T., Yanosky, J. D., & Lubin, J. (2016, Nov-Dec). Variability of Uncrossmatched Blood Use by Helicopter EMS Programs in the United States. *Prehosp Emerg Care*, 20(6), 688-694. <https://doi.org/10.1080/10903127.2016.1182607>
- Karon, B. S., Hoyer, J. D., Stubbs, J. R., & Thomas, D. D. (2009, Jul). Changes in Band 3 oligomeric state precede cell membrane phospholipid loss during blood bank storage of red blood cells. *Transfusion*, 49(7), 1435-1442. <https://doi.org/10.1111/j.1537-2995.2009.02133.x>
- Kihm, A., Kaestner, L., Wagner, C., & Quint, S. (2018). Classification of red blood cell shapes in flow using outlier tolerant machine learning. *PLoS computational biology*, 14(6), e1006278.

- Kingma, D. P., & Ba, J. (2015). Adam: A Method for Stochastic Optimization. *CoRR*, *abs/1412.6980*.
- Kleber, C., Giesecke, M. T., Tsokos, M., Haas, N. P., & Buschmann, C. T. (2013, May). Trauma-related preventable deaths in Berlin 2010: need to change prehospital management strategies and trauma management education. *World J Surg*, *37*(5), 1154-1161. <https://doi.org/10.1007/s00268-013-1964-2>
- Klose, T., Borchert, H. H., Pruss, A., Roth, W. K., Bohnen, H. R., & Putzker, M. (2010, Jul 1). Current concepts for quality assured long-distance transport of temperature-sensitive red blood cell concentrates. *Vox Sang*, *99*(1), 44-53. <https://doi.org/10.1111/j.1423-0410.2009.01302.x>
- Korgun, D. K., Bilmen, S., & Yesilkaya, A. (2001). Alterations in the erythrocyte antioxidant system of blood stored in blood bags. *Res Commun Mol Pathol Pharmacol*, *109*(5-6), 357-363.
- Koza, J. R., Bennett, F.H., Andre, D., Keane, M.A. (1996). Automated Design of Both the Topology and Sizing of Analog Electrical Circuits Using Genetic Programming. In J. S. Gero, Sudweeks, F., (Ed.), *Artificial Intelligence in Design '96* (pp. 151-170). Springer.
- Kriebardis, A. G., Antonelou, M. H., Stamoulis, K. E., Economou-Petersen, E., Margaritis, L. H., & Papassideri, I. S. (2008, Sep). RBC-derived vesicles during storage: ultrastructure, protein composition, oxidation, and signaling components. *Transfusion*, *48*(9), 1943-1953. <https://doi.org/10.1111/j.1537-2995.2008.01794.x>
- Krizhevsky, A., Sutskever, I., & Hinton, G. (2012, 01/01). ImageNet Classification with Deep Convolutional Neural Networks. *Neural Information Processing Systems*, *25*. <https://doi.org/10.1145/3065386>
- Kubat, M., & Kubat. (2017). *An introduction to machine learning* (Vol. 2). Springer.
- Kurup, P. A., Arun, P., Gayathri, N. S., Dhanya, C. R., & Indu, A. R. (2003, Nov). Modified formulation of CPDA for storage of whole blood, and of SAGM for storage of red blood cells, to maintain the concentration of 2,3-diphosphoglycerate. *Vox Sang*, *85*(4), 253-261. <https://doi.org/10.1111/j.0042-9007.2003.00366.x>
- Lacroix, J., Hebert, P. C., Fergusson, D. A., Tinmouth, A., Cook, D. J., Marshall, J. C., Clayton, L., McIntyre, L., Callum, J., Turgeon, A. F., Blajchman, M. A., Walsh, T. S., Stanworth, S. J., Campbell, H., Capellier, G., Tiberghien, P., Bardiaux, L., van de Wating, L., van der Meer, N. J., Sabri, E., Vo, D., Investigators, A., & Canadian Critical Care Trials, G. (2015, Apr 9). Age of transfused blood in critically ill adults. *N Engl J Med*, *372*(15), 1410-1418. <https://doi.org/10.1056/NEJMoa1500704>
- Lanotte, L., Mauer, J., Mendez, S., Fedosov, D. A., Fromental, J. M., Claveria, V., Nicoud, F., Gompper, G., & Abkarian, M. (2016, Nov 22). Red cells' dynamic morphologies govern blood shear thinning under microcirculatory flow conditions. *Proc Natl Acad Sci U S A*, *113*(47), 13289-13294. <https://doi.org/10.1073/pnas.1608074113>
- LeCun, Y. B., B.; Denker, J. S.; Henderson, D.; Howard, R. E.; Hubbard, W.; Jackel, L. D. (1989). Backpropagation Applied to Handwritten Zip Code Recognition. *Neural Computation*, *1*(4), 541-551. <https://doi.org/10.1162/neco.1989.1.4.541>
- LeCun, Y. B., L.; Bengio, Y.; Haffner, P. (1998). Gradient-based learning applied to document recognition. *Proceedings of the IEEE*, *86*(11), 2278-2324. <https://doi.org/10.1109/5.726791>
- Lelubre, C., Piagnerelli, M., & Vincent, J. L. (2009, Jul). Association between duration of storage of transfused red blood cells and morbidity and mortality in adult patients: myth or reality? *Transfusion*, *49*(7), 1384-1394. <https://doi.org/10.1111/j.1537-2995.2009.02211.x>

- Lim, G., Wortis, M., & Mukhopadhyay, R. (2002, 12/01). Stomatocyte-discocyte-echinocyte sequence of the human red blood cell: Evidence for the bilayer-couple hypothesis from membrane mechanics. *Proceedings of the National Academy of Sciences of the United States of America*, 99, 16766-16769. <https://doi.org/10.1073/pnas.202617299>
- Litjens, G., Kooi, T., Bejnordi, B. E., Setio, A. A. A., Ciompi, F., Ghafoorian, M., van der Laak, J., van Ginneken, B., & Sánchez, C. I. (2017, Dec). A survey on deep learning in medical image analysis. *Med Image Anal*, 42, 60-88. <https://doi.org/10.1016/j.media.2017.07.005>
- Lockey, D. J., Weaver, A. E., & Davies, G. E. (2013, Jan). Practical translation of hemorrhage control techniques to the civilian trauma scene. *Transfusion*, 53 Suppl 1, 17S-22S. <https://doi.org/10.1111/trf.12031>
- Lockwood, W. B., Hudgens, R. W., Szymanski, I. O., Teno, R. A., & Gray, A. D. (2003, Nov). Effects of rejuvenation and frozen storage on 42-day-old AS-3 RBCs. *Transfusion*, 43(11), 1527-1532. <https://doi.org/10.1046/j.1537-2995.2003.00551.x>
- Longster, G. H., Buckley, T., Sikorski, J., & Derrick Tovey, L. A. (1972). Scanning electron microscope studies of red cell morphology. Changes occurring in red cell shape during storage and post transfusion. *Vox Sang*, 22(2), 161-170. <https://doi.org/10.1111/j.1423-0410.1972.tb05122.x>
- Lu, M., & Shevkoplyas, S. S. (2020). Dynamics of shape recovery by stored red blood cells during washing at the single cell level. *Transfusion*, 60(10), 2370-2378.
- Lyon, R. M., de Sausmarez, E., McWhirter, E., Wareham, G., Nelson, M., Matthies, A., Hudson, A., Curtis, L., Russell, M. Q., Kent, S., & Sussex Air Ambulance, T. (2017, Feb 14). Pre-hospital transfusion of packed red blood cells in 147 patients from a UK helicopter emergency medical service. *Scand J Trauma Resusc Emerg Med*, 25(1), 12. <https://doi.org/10.1186/s13049-017-0356-2>
- Makroo, R. N., Raina, V., Bhatia, A., Gupta, R., Majid, A., Thakur, U. K., & Rosamma, N. L. (2011, Jan). Evaluation of the red cell hemolysis in packed red cells during processing and storage. *Asian J Transfus Sci*, 5(1), 15-17. <https://doi.org/10.4103/0973-6247.75970>
- Marik, P. E., & Corwin, H. L. (2008, Sep). Efficacy of red blood cell transfusion in the critically ill: a systematic review of the literature. *Crit Care Med*, 36(9), 2667-2674. <https://doi.org/10.1097/CCM.0b013e3181844677>
- Mauer, J., Mendez, S., Lanotte, L., Nicoud, F., Abkarian, M., Gompper, G., & Fedosov, D. A. (2018, Sep 14). Flow-Induced Transitions of Red Blood Cell Shapes under Shear. *Phys Rev Lett*, 121(11), 118103. <https://doi.org/10.1103/PhysRevLett.121.118103>
- Melzak, K. A., Spouge, J. L., Boecker, C., Kirschhofer, F., Brenner-Weiss, G., & Bieback, K. (2021, Feb). Hemolysis Pathways during Storage of Erythrocytes and Inter-Donor Variability in Erythrocyte Morphology. *Transfus Med Hemother*, 48(1), 39-47. <https://doi.org/10.1159/000508711>
- Mesarec, L., Gózdź, W., Iglić, A., Kralj-Iglić, V., Virga, E. G., & Kralj, S. (2019, 2019/12/24). Normal red blood cells' shape stabilized by membrane's in-plane ordering. *Scientific Reports*, 9(1), 19742. <https://doi.org/10.1038/s41598-019-56128-0>
- Mohandas, N., & Chasis, J. A. (1993, Jul). Red blood cell deformability, membrane material properties and shape: regulation by transmembrane, skeletal and cytosolic proteins and lipids. *Semin Hematol*, 30(3), 171-192.
- Napolitano, L. M., Kurek, S., Luchette, F. A., Anderson, G. L., Bard, M. R., Bromberg, W., Chiu, W. C., Cipolle, M. D., Clancy, K. D., Diebel, L., Hoff, W. S., Hughes, K. M., Munshi, I., Nayduch, D., Sandhu, R., Yelon, J. A., Corwin, H. L., Barie, P. S., Tisherman, S. A., Hebert, P. C., Workgroup, E. P. M., & American College of Critical Care Medicine Taskforce of the Society of Critical Care, M. (2009, Dec). Clinical practice guideline:

- red blood cell transfusion in adult trauma and critical care. *J Trauma*, 67(6), 1439-1442. <https://doi.org/10.1097/TA.0b013e3181ba7074>
- Nilsson, L., Hedner, U., Nilsson, I. M., & Robertson, B. (1983, Sep-Oct). Shelf-life of bank blood and stored plasma with special reference to coagulation factors. *Transfusion*, 23(5), 377-381. <https://doi.org/10.1046/j.1537-2995.1983.23584018713.x>
- Oja, E. (1989). NEURAL NETWORKS, PRINCIPAL COMPONENTS, AND SUBSPACES. *International Journal of Neural Systems*, 01(01), 61-68. <https://doi.org/10.1142/s0129065789000475>
- Otani, T., Oki, K., Akino, M., Tamura, S., Naito, Y., Homma, C., Ikeda, H., & Sumita, S. (2012, Jan). Effects of helicopter transport on red blood cell components. *Blood Transfus*, 10(1), 78-86. <https://doi.org/10.2450/2011.0029-11>
- Otto, O., Rosendahl, P., Mietke, A., Golfier, S., Herold, C., Klaue, D., Girardo, S., Pagliara, S., Ekpenyong, A., & Jacobi, A. (2015). Real-time deformability cytometry: on-the-fly cell mechanical phenotyping. *Nature methods*, 12(3), 199-202.
- Oyeniya, B. T., Fox, E. E., Scerbo, M., Tomasek, J. S., Wade, C. E., & Holcomb, J. B. (2017, Jan). Trends in 1029 trauma deaths at a level 1 trauma center: Impact of a bleeding control bundle of care. *Injury*, 48(1), 5-12. <https://doi.org/10.1016/j.injury.2016.10.037>
- Palis, J. (2008, May). Ontogeny of erythropoiesis. *Curr Opin Hematol*, 15(3), 155-161. <https://doi.org/10.1097/MOH.0b013e3282f97ae1>
- Paris, G., Robilliard, D., & Fonlupt, C. (2004). Exploring Overfitting in Genetic Programming. In P. Liardet, P. Collet, C. Fonlupt, E. Lutton, & M. Schoenauer, *Artificial Evolution* Berlin, Heidelberg.
- Perutz, M. F., Rossmann, M. G., Cullis, A. F., Muirhead, H., Will, G., & North, A. C. (1960, Feb 13). Structure of haemoglobin: a three-dimensional Fourier synthesis at 5.5-Å resolution, obtained by X-ray analysis. *Nature*, 185(4711), 416-422. <https://doi.org/10.1038/185416a0>
- Pfeifer, R., Tarkin, I. S., Rocos, B., & Pape, H. C. (2009, Sep). Patterns of mortality and causes of death in polytrauma patients--has anything changed? *Injury*, 40(9), 907-911. <https://doi.org/10.1016/j.injury.2009.05.006>
- Piety, N. Z., Gifford, S. C., Yang, X., & Shevkopyas, S. S. (2015, Oct). Quantifying morphological heterogeneity: a study of more than 1 000 000 individual stored red blood cells. *Vox Sang*, 109(3), 221-230. <https://doi.org/10.1111/vox.12277>
- Pinto, R. N., Sebastian, J. A., Parsons, M. J., Chang, T. C., Turner, T. R., Acker, J. P., & Kolios, M. C. (2019, Sep). Label-Free Analysis of Red Blood Cell Storage Lesions Using Imaging Flow Cytometry. *Cytometry A*, 95(9), 976-984. <https://doi.org/10.1002/cyto.a.23846>
- Pittman, R. N. (2011). *Regulation of Tissue Oxygenation*. Morgan & Claypool Life Sciences.
- Powers, D. M. W. (2011). Evaluation: from precision, recall and F-measure to ROC, informedness, markedness and correlation. *J Mach Learn Tech*, 2, 37-63.
- Practical guideline for blood component therapy. (1996, Mar). A report by the American Society of Anesthesiologists Task Force on Blood Component Therapy. *Anesthesiology*, 84(3), 732-747.
- Rehn, M., Weaver, A., Brohi, K., Eshelby, S., Green, L., Roislien, J., & Lockey, D. J. (2019, Mar). Effect of Prehospital Red Blood Cell Transfusion on Mortality and Time of Death in Civilian Trauma Patients. *Shock*, 51(3), 284-288. <https://doi.org/10.1097/SHK.0000000000001166>

- Reichel, F., Mauer, J., Nawaz, A. A., Gompper, G., Guck, J., & Fedosov, D. A. (2019, Jul 9). High-Throughput Microfluidic Characterization of Erythrocyte Shapes and Mechanical Variability. *Biophys J*, 117(1), 14-24. <https://doi.org/10.1016/j.bpj.2019.05.022>
- Rentas, F. J., Macdonald, V. W., Houchens, D. M., Hmel, P. J., & Reid, T. J. (2004, Feb). New insulation technology provides next-generation containers for "iceless" and lightweight transport of RBCs at 1 to 10 degrees C in extreme temperatures for over 78 hours. *Transfusion*, 44(2), 210-216. <https://doi.org/10.1111/j.1537-2995.2004.00642.x>
- Rogers, M. A., Blumberg, N., Saint, S., Langa, K. M., & Nallamothu, B. K. (2009, Jul 31). Hospital variation in transfusion and infection after cardiac surgery: a cohort study. *BMC Med*, 7, 37. <https://doi.org/10.1186/1741-7015-7-37>
- Roussel, C., Buffet, P. A., & Amireault, P. (2018). Measuring Post-transfusion Recovery and Survival of Red Blood Cells: Strengths and Weaknesses of Chromium-51 Labeling and Alternative Methods. *Front Med (Lausanne)*, 5, 130. <https://doi.org/10.3389/fmed.2018.00130>
- Roussel, C., Dussiot, M., Marin, M., Morel, A., Ndour, P. A., Duez, J., Le Van Kim, C., Hermine, O., Colin, Y., Buffet, P. A., & Amireault, P. (2017, Apr). Spherocytic shift of red blood cells during storage provides a quantitative whole cell-based marker of the storage lesion. *Transfusion*, 57(4), 1007-1018. <https://doi.org/10.1111/trf.14015>
- Roussel, C., Morel, A., Dussiot, M., Marin, M., Colard, M., Fricot-Monsinjon, A., Martinez, A., Chambrion, C., Henry, B., Casimir, M., Volle, G., Depond, M., Dokmak, S., Paye, F., Sauvanet, A., Le Van Kim, C., Colin, Y., Georgeault, S., Roingear, P., Spitalnik, S. L., Ndour, P. A., Hermine, O., Hod, E. A., Buffet, P. A., & Amireault, P. (2021, Apr 29). Rapid clearance of storage-induced microerythrocytes alters transfusion recovery. *Blood*, 137(17), 2285-2298. <https://doi.org/10.1182/blood.2020008563>
- Rudolph, M., Sitzmann, N., Braun, J., Henkel, B., & Reifferscheidt, F. (2021). Präklinische Therapie mit Blutprodukten – das Projekt "HeliBlut" Prehospital Therapy with Blood Products – the "HeliBlut" Project. *Notarzt*, 37(06), 319 - 324. <https://doi.org/10.1055/a-1546-1374>
- Schmidhuber, J. (2015, 2015/01/01/). Deep learning in neural networks: An overview. *Neural Networks*, 61, 85-117. <https://doi.org/https://doi.org/10.1016/j.neunet.2014.09.003>
- Selleng, k. (2020). Der Blutungsnotfall - Versorgungskonzepte für Patienten mit unbekannter Blutgruppe. *Transfusionsmedizin*, 10, 151-158.
- Shackelford, S. A., Del Junco, D. J., Powell-Dunford, N., Mazuchowski, E. L., Howard, J. T., Kotwal, R. S., Gurney, J., Butler, F. K., Jr., Gross, K., & Stockinger, Z. T. (2017, Oct 24). Association of Prehospital Blood Product Transfusion During Medical Evacuation of Combat Casualties in Afghanistan With Acute and 30-Day Survival. *JAMA*, 318(16), 1581-1591. <https://doi.org/10.1001/jama.2017.15097>
- Shapiro, H. M. (2003). How Flow Cytometers Work. In *Practical Flow Cytometry* (pp. 101-223). <https://doi.org/https://doi.org/10.1002/0471722731.ch4>
- Sheetz, M. P., & Singer, S. (1974). Biological membranes as bilayer couples. A molecular mechanism of drug-erythrocyte interactions. *Proceedings of the National Academy of Sciences*, 71(11), 4457-4461.
- Shen, D., Wu, G., & Suk, H. I. (2017, Jun 21). Deep Learning in Medical Image Analysis. *Annu Rev Biomed Eng*, 19, 221-248. <https://doi.org/10.1146/annurev-bioeng-071516-044442>
- Shorten, C., & Khoshgoftaar, T. M. (2019, 2019/07/06). A survey on Image Data Augmentation for Deep Learning. *Journal of Big Data*, 6(1), 60. <https://doi.org/10.1186/s40537-019-0197-0>

- Sierra, F. D. (2017): *Flow Cytomorphometry for Assessment of Red Blood Cell Storage Lesion*. Med. Dissertation. Medizinische Fakultät Mannheim, Universität Heidelberg.
- Sierra, F. D., Melzak, K. A., Janetzko, K., Kluter, H., Suhr, H., Bieback, K., & Wiedemann, P. (2017, Sep). Flow morphometry to assess the red blood cell storage lesion. *Cytometry A*, 91(9), 874-882. <https://doi.org/10.1002/cyto.a.23127>
- Silliman, C. C., & McLaughlin, N. J. (2006, May). Transfusion-related acute lung injury. *Blood Rev*, 20(3), 139-159. <https://doi.org/10.1016/j.blre.2005.11.001>
- Sokolova, M., Japkowicz, N., & Szpakowicz, S. (2006). Beyond Accuracy, F-Score and ROC: A Family of Discriminant Measures for Performance Evaluation. In A. Sattar & B.-h. Kang, *AI 2006: Advances in Artificial Intelligence* Berlin, Heidelberg.
- Sparrow, R. L. (2010, Jun). Red blood cell storage and transfusion-related immunomodulation. *Blood Transfus*, 8 Suppl 3, s26-30. <https://doi.org/10.2450/2010.005S>
- Stehman, S. V. (1997). Selecting and interpreting measures of thematic classification accuracy. *Remote sensing of Environment*, 62(1), 77-89.
- Steiner, M. E., Ness, P. M., Assmann, S. F., Triulzi, D. J., Sloan, S. R., Delaney, M., Granger, S., Bennett-Guerrero, E., Blajchman, M. A., Scavo, V., Carson, J. L., Levy, J. H., Whitman, G., D'Andrea, P., Pulkrabek, S., Ortel, T. L., Bornikova, L., Raife, T., Puca, K. E., Kaufman, R. M., Nuttall, G. A., Young, P. P., Youssef, S., Engelman, R., Greilich, P. E., Miles, R., Josephson, C. D., Bracey, A., Cooke, R., McCullough, J., Hunsaker, R., Uhl, L., McFarland, J. G., Park, Y., Cushing, M. M., Klodell, C. T., Karanam, R., Roberts, P. R., Dyke, C., Hod, E. A., & Stowell, C. P. (2015, Apr 9). Effects of red-cell storage duration on patients undergoing cardiac surgery. *N Engl J Med*, 372(15), 1419-1429. <https://doi.org/10.1056/NEJMoa1414219>
- Stone, M. (1974). Cross-Validatory Choice and Assessment of Statistical Predictions. *Journal of the Royal Statistical Society. Series B (Methodological)*, 36(2), 111-147.
- Suhr, H., & Herkommer, A. M. (2015, Nov). In situ microscopy using adjustment-free optics. *J Biomed Opt*, 20(11), 116007. <https://doi.org/10.1117/1.JBO.20.11.116007>
- Suhr, H., Wehnert, G., Schneider, K., Bittner, C., Scholz, T., Geissler, P., Jahne, B., & Scheper, T. (1995, Jul 5). In situ microscopy for on-line characterization of cell-populations in bioreactors, including cell-concentration measurements by depth from focus. *Biotechnol Bioeng*, 47(1), 106-116. <https://doi.org/10.1002/bit.260470113>
- Szegedy, C., Liu, W., Jia, Y., Sermanet, P., Reed, S. E., Anguelov, D., Erhan, D., Vanhoucke, V., & Rabinovich, A. (2015). Going deeper with convolutions. *2015 IEEE Conference on Computer Vision and Pattern Recognition (CVPR)*, 1-9.
- Tchir, J. D., Acker, J. P., & Holovati, J. L. (2013, Dec). Rejuvenation of ATP during storage does not reverse effects of the hypothermic storage lesion. *Transfusion*, 53(12), 3184-3191. <https://doi.org/10.1111/trf.12194>
- Thies, K. C., Truhlar, A., Keene, D., Hinkelbein, J., Rutzler, K., Brazzi, L., & Vivien, B. (2020, Aug 14). Pre-hospital blood transfusion - an ESA survey of European practice. *Scand J Trauma Resusc Emerg Med*, 28(1), 79. <https://doi.org/10.1186/s13049-020-00774-1>
- Tinmouth, A., & Chin-Yee, I. (2001, Apr). The clinical consequences of the red cell storage lesion. *Transfus Med Rev*, 15(2), 91-107. <https://doi.org/10.1053/tmrv.2001.22613>
- Tinmouth, A., Fergusson, D., Yee, I. C., Hebert, P. C., Investigators, A., & Canadian Critical Care Trials, G. (2006, Nov). Clinical consequences of red cell storage in the critically ill. *Transfusion*, 46(11), 2014-2027. <https://doi.org/10.1111/j.1537-2995.2006.01026.x>
- Tombak, A. (2019). Introductory Chapter: Erythrocytes - Basis of Life. In A. Tombak (Ed.), *Erythrocyte*. IntechOpen. <https://doi.org/10.5772/intechopen.88847>

- Turgeon, M. L. (2011). *Clinical Hematology: Theory and Procedures* (5 th. Ed. ed.). Lippincott Williams & Wilkins.
- Usry, R. T., Moore, G. L., & Manalo, F. W. (1975). Morphology of stored, rejuvenated human erythrocytes. *Vox Sang*, 28(3), 176-183. <https://doi.org/10.1111/j.1423-0410.1975.tb02756.x>
- Vamvakas, E. C., & Carven, J. H. (1999, Jul). Transfusion and postoperative pneumonia in coronary artery bypass graft surgery: effect of the length of storage of transfused red cells. *Transfusion*, 39(7), 701-710. <https://doi.org/10.1046/j.1537-2995.1999.39070701.x>
- Vuille-Lessard, E., Boudreault, D., Girard, F., Ruel, M., Chagnon, M., & Hardy, J. F. (2010, Oct). Red blood cell transfusion practice in elective orthopedic surgery: a multicenter cohort study. *Transfusion*, 50(10), 2117-2124. <https://doi.org/10.1111/j.1537-2995.2010.02697.x>
- Wagner, G. M., Chiu, D. T., Qju, J. H., Heath, R. H., & Lubin, B. H. (1987, Jun). Spectrin oxidation correlates with membrane vesiculation in stored RBCs. *Blood*, 69(6), 1777-1781.
- Wong, P. (1999, Feb 7). A basis of echinocytosis and stomatocytosis in the disc-sphere transformations of the erythrocyte. *J Theor Biol*, 196(3), 343-361. <https://doi.org/10.1006/jtbi.1998.0845>
- Yazer, M. H., Podlosky, L., Clarke, G., & Nahirniak, S. M. (2004, Jan). The effect of prestorage WBC reduction on the rates of febrile nonhemolytic transfusion reactions to platelet concentrates and RBC. *Transfusion*, 44(1), 10-15. <https://doi.org/10.1046/j.0041-1132.2003.00518.x>
- Zehnder, L., Schulzki, T., Goede, J. S., Hayes, J., & Reinhart, W. H. (2008, Nov). Erythrocyte storage in hypertonic (SAGM) or isotonic (PAGGSM) conservation medium: influence on cell properties. *Vox Sang*, 95(4), 280-287. <https://doi.org/10.1111/j.1423-0410.2008.01097.x>
- Zhang, W. J. a. Y., Guosheng and Lin, Yingzi and Ji, Chunli and Gupta, Madan M. (2018). On Definition of Deep Learning. *2018 World Automation Congress (WAC)*, 1-5. <https://doi.org/10.23919/WAC.2018.8430387>
- Zimrin, A. B., & Hess, J. R. (2009, Feb). Current issues relating to the transfusion of stored red blood cells. *Vox Sang*, 96(2), 93-103. <https://doi.org/10.1111/j.1423-0410.2008.01117.x>

Publications by the Author:

Boecker, C., Sitzmann, N., Halblaub Miranda, J. L., Suhr, H., Wiedemann, P., Bieback, K., Rudolph, M., & Klüter, H. (2022). Noninferior Red Cell Concentrate Quality after Repeated Air Rescue Mission Transport for Prehospital Transfusion. *Transfusion Medicine and Hemotherapy*, 49(3), 172-179. <https://doi.org/10.1159/000520650>

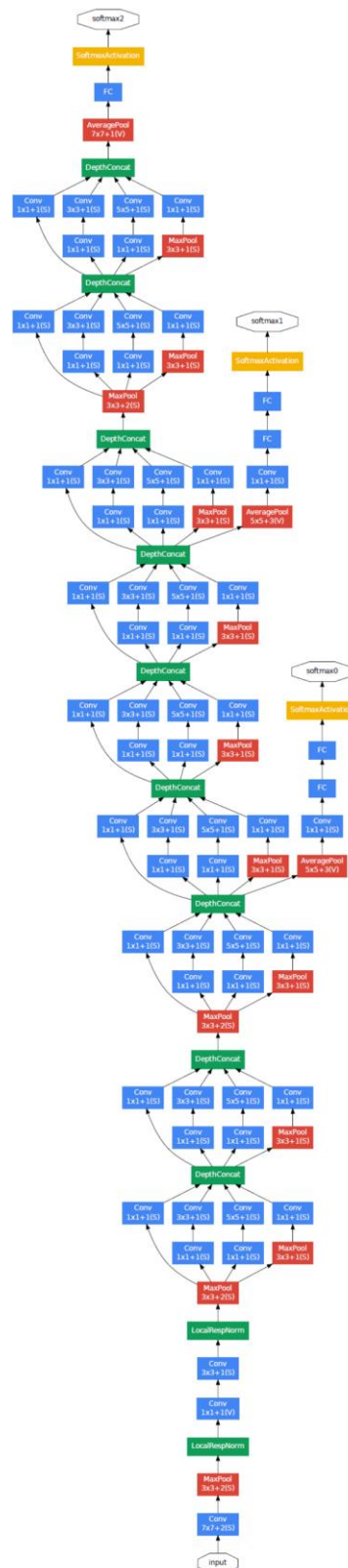
Melzak, K. A., Spouge, J. L., Boecker, C., Kirschhofer, F., Brenner-Weiss, G., & Bieback, K. (2021). Hemolysis Pathways during Storage of Erythrocytes and Inter-Donor Variability in Erythrocyte Morphology. *Transfus Med Hemother*, 48(1), 39-47. <https://doi.org/10.1159/000508711>

Oral presentations:

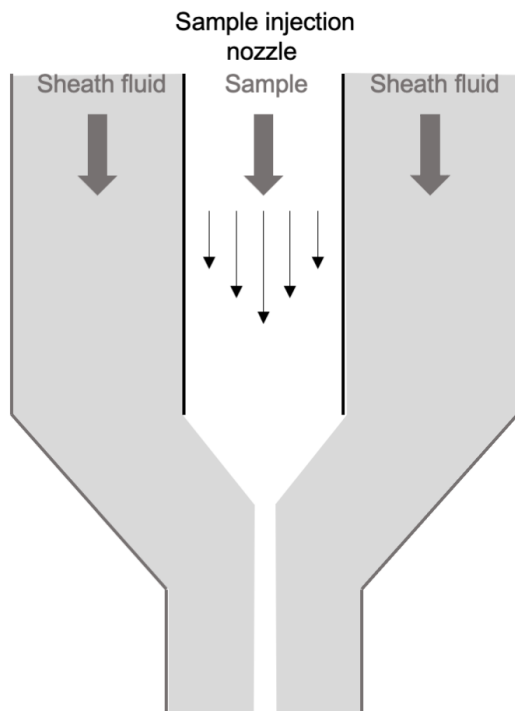
Böcker, C. Repeated helicopter transport of red cell concentrates for prehospital transfusion is feasible for up to 42 days. 54th Annual Meeting of the German Society for Transfusion Medicine and Immune Hematology (DGTI 2021), digital.

Böcker, C., Flow Cytomorphometry of Red Blood Cell Concentrates: Morphology vs. Hemolysis Quantification. 53th Annual Meeting of the German Society for Transfusion Medicine and Immune Hematology (DGTI 2020), digital.

## 7 SUPPLEMENTARY INFORMATION



Supplementary Figure 1. Complete architecture of GoogLeNet (Szegedy et al., 2015).



Calculation of maximal shear rate at the walls in the sample injection nozzle of imaging flow cytometers with typical parameter values according to [Shapiro 2003]:

$$\text{Shear rate at wall} = \dot{\gamma}_w = \frac{4}{\pi \cdot r^3} \cdot \dot{v}$$
$$\dot{\gamma}_w = 1273,24 \frac{1}{s}$$

where

$r = 100\mu\text{m}$

$\dot{v} = 1 \mu\text{L/s}$

Radius of injection nozzle

Sample volume flow

Supplementary Figure 2. Scheme of sample injection in an imaging flow cytometer and calculation of maximal shear rate at the walls in sample injection nozzle of IFCs.

## 8 CURRICULUM VITAE

### **Clemens Böcker**

18.05.1994 in Minden, Deutschland

Turnerstraße 39

69126 Heidelberg

Deutschland

E-Mail: clemensboecker@web.de

Tel.: 0170 / 4537116



### **AKADEMISCHER WERDEGANG**

<b>Jun 19 - heute</b>	<p><b>Promotion</b>          Medizinische Fakultät Mannheim (UMM), Universität Heidelberg. Mannheim, Deutschland          Angestrebter Abschluss: Dr. sc. hum.          Thema des Arbeitsvorhabens: Flow Morphometry of red blood cell storage quality based on neural networks          Unterstützt durch Promotionsstipendien der Albert-und-Anneliese-Konanz Stiftung und der Karl-Völker Stiftung</p>
<b>März 17 - Nov 18</b>	<p><b>Masterstudium Biotechnologie mit Schwerpunkt Bioprocess Development</b>          Hochschule Mannheim. Mannheim, Deutschland          Abschluss: MSc in Biotechnologie mit 1,1          Masterarbeit: Flow Cytomorphometry for Assessment of Red Blood Cells</p>
<b>Sept 13 - Feb 17</b>	<p><b>Bachelorstudium Biotechnologie</b>          Hochschule Mannheim. Mannheim, Deutschland          Abschluss: BSc in Biotechnologie mit 1,7          Bachelorarbeit: Etablierung einer Methode zur molekularbiologischen Diagnose weingutseigener Hefen</p>
<b>Sept 15 - Jan 16</b>	<p><b>Praxissemester</b>          University of Hawaii at Manoa. Hawaii, USA          Praxissemester: Optimizing Calcein protocol for HLB disease inside LAMP reaction          Unterstützt durch Studienprogramm Interstip der Albert-und-Anneliese-Konanz Stiftung</p>
<b>Aug 05 - Juni 13</b>	<p><b>Abitur</b>          Ratsgymnasium Minden. Minden, Deutschland          Abitur mit 1,8</p>
<b>Jan 11 - Juni 11</b>	<p><b>Schulischer Auslandsaufenthalt</b>          Canterbury School. Fort Myers, USA</p>

---

**BERUFSERFAHRUNG**

---

- Apr 22 - Juni 22**      **Wissenschaftlicher Mitarbeiter (im Rahmen einer Promotion)**  
Entwicklung von Neuronalen Netzen für den Einsatz von *in-situ* Technologie in Klärwerken  
Hochschule Mannheim, Mannheim, Deutschland
- Mai 19**                **Auftragsarbeit**  
Implementierung eines Bioreaktors  
Hochschule Mannheim, Mannheim, Deutschland
- Jan 19 - März 19**    **Wissenschaftliche Hilfskraft**  
Institut für Grenzflächen (IFG), KIT. Karlsruhe, Deutschland
- Feb 17 - März 17**    **Studentische Hilfskraft**  
Dienstleistungszentrum Ländlicher Raum Rheinpfalz (DLR-Rheinpfalz). Neustadt an der Weinstraße, Deutschland

---

**WEITERE QUALIFIKATIONEN**

---

- Sprachen**            Deutsch: flüssig  
Englisch: flüssig
- EDV**                    Microsoft Office: sehr gut  
Berkeley Madonna: sehr gut  
MATLAB: gut  
MATLAB (CNN): sehr gut  
MarkerView (PCA): gut

---

**PUBLIKATIONSLISTE**

---

- Boecker, C.**, Sitzmann, N., Halblaub Miranda, J. L., Suhr, H., Wiedemann, P., Bieback, K., Rudolph, M., & Klüter, H. (2022). Noninferior Red Cell Concentrate Quality after Repeated Air Rescue Mission Transport for Prehospital Transfusion. *Transfusion Medicine and Hemotherapy*, 49(3), 172-179. <https://doi.org/10.1159/000520650>
- Melzak, K. A., Spouge, J. L., **Boecker, C.**, Kirschhofer, F., Brenner-Weiss, G., & Bieback, K. (2021). Hemolysis Pathways during Storage of Erythrocytes and Inter-Donor Variability in Erythrocyte Morphology. *Transfus Med Hemother*, 48(1), 39-47. <https://doi.org/10.1159/000508711>

## 9 ACKNOWLEDGMENTS

A doctoral thesis – no matter how motivated or inspired one might be – cannot be completed without the help of many others.

This work would not have been possible without the funding of the Albert-and-Annelise-Konanz Foundation as well as the Karl-Völker Foundation of the Mannheim University of Applied Sciences.

First, I thank my supervisor Prof. Dr. rer. nat. Karen Bieback for the opportunity to carry out this stimulating doctoral research. From the very beginning you helped me to discover a unique interdisciplinary topic with the helicopter study. Your willingness to overcome all concerns and provide all necessary resources in order to make this project a success has been an invaluable help. Moreover, your optimism and clear-headed approaches created an excellent working atmosphere.

Secondly, my thanks goes to Prof Dr. Philip Wiedemann. None of the chapters in this thesis could have been completed without your excellent guidance of this project in every respect. Your vision for coordinating the academic and operational issues were essential for the development of this project.

Thank you too to Prof. Dr. Suhr. First of all, for the opportunity to work with *in situ* microscopy in your lab but also for your help at any time of the day, even when you are on vacation.

Further, I am deeply grateful for the extreme amount of time and help which you, Mr. Wiedemann and Suhr, gave, especially in our long-lasting Tuesday discussions! Your teaching and enthusiastic mind helped me to improve my analytical and scientific thinking but also to grow as a person.

Thank you Dr. med. Nicole Sitzmann. The helicopter study could not have happened without your coordination skills and the effort you put into the implementation and monitoring of all steps in the study.

I also want to thank Prof. Dr. med. Harald Klüter for letting me carry out this PhD project in his institute. I owe gratitude to Prof. Dr. Wuchter for providing space in his laboratory for carrying out all the flow morphometry measurements.

I wish to thank all the staff of the quality control laboratory and the staff that look after the erythrocyte concentrates of the Blood Donor Service Mannheim for performing the

experiments, the biochemical measurements and the logistics to carry out the monitoring of the RCCs.

I would like to thank José Halblaub. You supported me since my Master thesis with all kinds of hardware and software problems – you are my permanent role model when it comes to a clean and organized lab desk. I am grateful to you for always being there for me, whenever I need your help, and I am glad for all the nice lunch breaks we had.

Thank you to my friends and family – you mean the world to me and provided me with the background to spend 3 years classifying red blood cells based on tiny differences in their shape. More sincerely, Danke Mama und Papa. You are the best and thank you for always letting me pursue my dreams.

Thank you Caro. For everything. I could not have achieved any of this without you.